

**DEVELOPMENT OF A FUSION METHODOLOGY FOR FLOOD MAPPING
USING SAR AND OPTICAL SATELLITE DATA**

**SAR VE OPTİK UYDU VERİLERİ KULLANILARAK TAŞKIN
HARİTALAMASI İÇİN FÜZYON YÖNTEMİ GELİŞTİRİLMESİ**

BESTE TAVUS

PROF. DR SULTAN KOCAMAN GÖKÇEOĞLU

Supervisor

Submitted to

Graduate School of Science and Engineering of Hacettepe University

As a Partial Fulfillment to Requirements

For the Award of Degree of Doctor of Philosophy

in Geomatics Engineering

2023

To my family

ABSTRACT

DEVELOPMENT OF A FUSION METHODOLOGY FOR FLOOD MAPPING USING SAR AND OPTICAL SATELLITE DATA

Beste TAVUS

Doctor of Philosophy, Department of Geomatics Engineering

Supervisor: Prof. Dr. Sultan KOCAMAN GÖKÇEOĞLU

September 2023, 101 pages

In this thesis, a feature-level data fusion methodology was developed using the random forest (RF) approach, which is one of the frequently utilized machine learning methods for natural hazard assessments. For this purpose, Sentinel-1 SAR and Sentinel-2 optical data provided regularly and free of charge by the European Space Agency were used. For the development and performance analysis of the method, two study areas/flood cases with different topographical characteristics and data availability conditions were analyzed. The first case is a dam failure in Uzbekistan-Sardoba, for which pre- and post-event Sentinel-1 and Sentinel-2 and external reference data (PlanetScope) are available. Since the flood disaster in this region was not caused by precipitation, it is independent of the cloud effect that obstructs the Sentinel-2 data after the event. In addition, the well-known synthetic aperture radar (SAR) distortions that disturb the Sentinel-1 data could be omitted thanks to the flat topography of the area. For this reason, the method proposed in the thesis was primarily developed in Sardoba and the results were evaluated by applying it to another area, the Türkiye-Ordu May 2018 floods. The Ordu flood case was caused by precipitation, and unlike the first study area, the region has rugged topography. When the results obtained were validated with external data, it was observed that

especially flood and flooded vegetation classes could be determined with high accuracy. In the thesis, flood mapping strategies to be undertaken based on data availability scenarios are discussed in detail.

Keywords: Flood extent mapping, satellite remote sensing, optical images, Synthetic Aperture Radar, data fusion, random forest classification.

ÖZET

SAR VE OPTİK UYDU VERİLERİ KULLANILARAK TAŞKIN HARİTALAMASI İÇİN FÜZYON YÖNTEMİ GELİŞTİRİLMESİ

Beste TAVUS

Doktora, Geomatik Mühendisliği Bölümü

Tez Danışmanı: Prof. Dr. Sultan KOCAMAN GÖKÇEOĞLU

Eylül 2023, 101 sayfa

Bu tezde, doğal afet değerlendirmelerinde sıklıkla kullanılan ve makine öğrenmesi yöntemlerinden biri olan rastgele orman (RO) yaklaşımı kullanılarak özellik düzeyinde veri birleştirme/füzyon metodolojisi geliştirilmiştir. Bu amaçla Avrupa Uzay Ajansı tarafından düzenli ve ücretsiz olarak sağlanan Sentinel-1 SAR ve Sentinel-2 optik verileri kullanılmıştır. Yöntemin geliştirilmesi ve performans analizi için, farklı topografik özelliklere ve veri erişim koşullarına sahip iki çalışma alanı/taşkın sahası analiz edilmiştir. İlk saha, olay öncesi ve sonrası Sentinel-1 ve Sentinel-2 ile harici referans verilerinin (PlanetScope) mevcut olduğu Özbekistan-Sardoba'daki bir baraj yıkılmasıdır. Bu bölgedeki sel felaketi yağıştan kaynaklanmadığı için olay sonrasında Sentinel-2 verilerini kısıtlayan bulut etkisinden bağımsızdır. Aynı zamanda bölgenin düz topoğrafyaya sahip olması sentetik açıklıklı radar (SAR) bozulmalarından kaynaklanan olumsuz etkilerin en aza indirgenmesini sağlamıştır. Bu nedenle, tezde önerilen yöntem öncelikle Sardoba'da geliştirilmiş ve sonuçlar, diğer bir alan olan Türkiye-Ordu Mayıs 2018 taşkınlarına uygulanarak değerlendirilmiştir. Ordu sel vakası yağıştan kaynaklanmış olup, ilk çalışma alanının aksine bölge engebeli bir topoğrafyaya sahiptir. Elde edilen

sonular harici verilerle doęrulandıęında, zellikle tařkın ve sular altında kalan bitki sınıflarının yksek doęrulukla belirlenebildięi grlmřtr. Tezde, veri eriřim/kullanılabilirlik senaryolarına dayalı olarak yapılacak tařkın haritalama stratejileri detaylı olarak ele alınmıřtır. Elde edilen bulgular literatrle karřılařtırılmıř ve mevcut zorluklar ve gelecek alıřmalar ortaya konmuřtur. Tezin ıktıları, tařkın tehlikesi deęerlendirmeleri, tehlikelere duyarlı Őehir ve kırsal planlama ve felaket nleme faaliyetleri iin nemlidir.

Anahtar Kelimeler: Tařkın alanı haritalaması, uydu uzaktan algılama, optik grntler, Sentetik Aıklıklı Radar, veri fzyonu, rastgele orman sınıflandırması.

ACKNOWLEDGMENTS

I would like to extend my heartfelt gratitude to all those who have contributed to the completion of this PhD thesis. First and foremost, I am deeply grateful to my thesis advisor, Prof. Dr. Sultan Kocaman Gökçeođlu, for her unwavering guidance, expertise, and encouragement throughout the entire research journey. Her guidance in both academic and personal life has been priceless in molding my research and life abilities.

Besides my advisors, I am also very thankful to my doctoral committee members Prof. Dr. Aslı Özdarcı Ok and Assoc. Prof. Dr. Saygın Abdikan for their valuable comments, and also Prof. Dr. Hakan Ahmet Nefesliođlu and Assoc. Prof. Dr. Nusret Demir for taking their time and contributing to my thesis as a jury member.

I would like to special thank Prof. Dr. Candan Gökçeođlu, who helped my research by sharing his expertise and ideas.

I would also like to thank my dear friends and colleagues Recep Can, Gizem Karakaş and İlyas Yalçın, who have the vision and motivation to always benefit and with whom I find great joy in collaborating.

I owe gratitude to my mother, father, sister and my grandmother, who passed away recently, for their support, patience and understanding throughout this thesis process, as in every period of my life. It was very valuable for me your emotional support and encouragement in every moment of my life.

In closing, I would like to acknowledge that this work represents only a small step in the vast realm of knowledge as well as thank you all for being a part of this remarkable journey.

CONTENTS

ABSTRACT	i
ÖZET.....	iii
ACKNOWLEDGMENTS.....	v
LIST OF FIGURES.....	ix
LIST OF TABLES	x
SYMBOLS AND ABBREVIATIONS	xi
1. INTRODUCTION.....	1
1.1. Problem Statement/Motivation	1
1.2. Thesis Objectives	3
1.3. Contributions	4
1.4. Thesis Outline	4
2. BACKGROUND ON FLOOD INUNDATION MAPPING USING REMOTE SENSING TECHNIQUES	6
2.1. Studies utilizing Optical Sensors.....	6
2.1.1. Coarse-resolution satellite sensors (> 250 m)	7
2.1.2. Medium-resolution satellite sensors (> 10 m).....	8
2.1.3. Very high-resolution satellite sensors (< 2 m)	9
2.1.3. Very high-resolution satellite sensors (< 2 m)	10
2.2. Studies utilizing Microwave Sensors	11
2.2.1. X-band Satellite Sensors	12
2.2.2. C-band Satellite Sensors.....	13
2.2.3. L-band Satellite Sensors.....	14
2.3 Studies utilizing both Optical and Radar Data	15
2.4. Studies utilizing Machine Learning Methods for Flood Mapping	18
2.4.1. Thresholding.....	18
2.4.2. Change detection	20

2.4.3. Supervised & unsupervised learning	21
3. METHODOLOGY.....	23
3.1. Satellite Sensors	23
3.1.1. Sentinel-1 Sensor Characteristics	23
3.1.2. Sentinel-2 Sensor Characteristics	24
3.1.3. PlanetScope Sensor Characteristics	24
3.2. Overview of the Proposed Workflow	25
3.3. Data Pre-processing	27
3.4. Feature Extraction and Analysis	29
3.4.1. GLCM Features	30
3.4.2. Spectral Indices.....	33
3.4.3. Principal Component Analysis	34
3.4.4. Feature Selection.....	34
3.5. Random Forest Classification.....	35
3.6. Validation.....	37
4. THE FLOOD EVENTS	39
4.1. Sardoba Dam Failure	39
4.1.1. Sardoba Study Area and Event Characteristics	39
4.1.2. Sardoba Data Characteristics	41
4.2. Ordu 2018 Flood.....	42
4.2.1. Ordu 2018 Study Area and Event Characteristics	42
4.2.2. Ordu Data Characteristics	44
5. RESULTS	46
5.1. Results from Sardoba Dam Failure.....	46
5.1.1 Feature Maps Produced for Sardoba Site (GLCM, Indices and PCA)	46
5.1.2. Flood Maps and Validation Results.....	50
5.2. Results from Ordu Site	59
5.2.1. Feature Maps Produced for Ordu Site (GLCM, Indices and PCA)	59
5.2.2. Flood Maps and Validation Results.....	62
6. DISCUSSION	67

6.1. On the use of radar and optical data and features	67
6.2. Data availability	71
6.3. On the use of textural features and effect of topography	73
7. CONCLUSION AND FUTURE WORK.....	75
7.1. Conclusions	75
7.2. Future Work	79
8. REFERENCES	82

LIST OF FIGURES

Figure 3.1. Overall methodological workflow.....	26
Figure 3.2. Pre-processing of the Sentinel-1&2 data.....	28
Figure 3.3. GLCM texture feature generation and selection.	32
Figure 3.4. Spectral feature generation.....	33
Figure 3.5. Boxplot of the 10-fold cross-validation results.	36
Figure 3.6. Examples from PlanetScope post-event (10/05/2020) image parts (left) and locations of training polygons depicted on post-event S2 RGB image (right) [128].	38
Figure 4.1. The study area location (a), the LULC map.....	40
Figure 4.2. Pre- & post-event satellite images of the study site obtained from Sentinel-2 in true color combination and the VV and VH polarization data of Sentinel-1.	42
Figure 4.3. The study area location (a), the LULC map.....	43
Figure 4.4. A part of pre- & post-event Sentinel-2 images of the study site and the VV and VH polarization data of Sentinel-1.	45
Figure 5.1. The RF classification results for; (a) Stack 1 (S1 only), (b) Stack 2 (S2 only), (c) Stack 3 (S1 and pre-event S2) and (d) Stack 4 (S1 and S2).....	51
Figure 5.2. The RF classification result for Stack 5 (without GLCM PCs).	52
Figure 5.3. Zoomed-in views of Stack 1-5 classification results for sub-areas A and B, denoted by the black rectangles in Figure 5.2.	52
Figure 5.4. The RF classification results obtained from (a) Stack 1, (b) Stack 2.	63
Figure 5.5. Flood map obtained from Stack 2 and 30 cm resolution orthophoto acquired on 17 August 2018. Blue dots illustrate conjugate points between the flood maps and orthophotos.	66
Figure 5.6. Flood map obtained from Stack 2, 30 cm resolution orthophoto acquired on 17 August 2018 and ground photos. Blue dots illustrate conjugate points between the flood maps, orthophotos and media photographs.	66

LIST OF TABLES

Table 2.1. Optical sensors and specifications.	7
Table 2.2. Most frequently used radar sensors and their specifications for flood activities.	12
Table 3.1. Data stacks and their components.	35
Table 4.1. Basic specifications of the datasets used in the Sardoba study area.	41
Table 4.2. Basic specifications of the datasets used in the Ordu study area.	44
Table 5.1. Overviews of selected textural features produced from S1 for Sardoba.	47
Table 5.2. Overviews of GLCM PCs derived from the S1 and their information percentages for Sardoba.	47
Table 5.3. Overviews of spectral indices produced from S2 datasets for Sardoba.	48
Table 5.4. Overviews of the textural features produced from S2 over Sardoba.	49
Table 5.5. Overviews the GLCM PCs derived from S2 and their information percentages over Sardoba.	50
Table 5.6. Confusion matrix produced from the classification of Stack 1 - 5, along with the accuracy metrics.	56
Table 5.7. Testing feature importance score of S1 and S2.	59
Table 5.8. Overviews of selected textural features produced from S1 over Ordu site.	60
Table 5.9. Overviews of GLCM PCs derived from the S1 and their information percentages over Ordu site.	61
Table 5.10. Overviews of spectral indices derived from S2 datasets over Ordu.	61
Table 5.11. Overviews of the textural features produced from S2 datasets in Ordu.	62
Table 5.12. Overviews of the PCs derived from S2 GLCM features and their information percentages over Ordu site.	62
Table 5.13. Confusion matrix produced from the classification of Stack 1 and 2, along with the accuracy metrics over Ordu site.	65

SYMBOLS AND ABBREVIATIONS

Abbreviations

BL	Bare Land
CR	Crop Area
CNN	Convolutional Neural Network
DEM	Digital Elevation Model
DT	Decision Trees
EO	Earth Observation
ESA	European Space Agency
FI	Flooded Area
FR	Forest Area
FV	Flooded Vegetation
GLCM	Gray Level Co-occurrence Matrix
GSD	Ground Sampling Distance
HH	Horizontal Horizontal
HV	Horizontal Vertical
InSAR	Interferometric Synthetic Aperture Radar
IPCC	Intergovernmental Panel on Climate Change
LULC	Land Use Land Cover
ML	Machine Learning
MLC	Maximum Likelihood Classification
NASA	National Aeronautics and Space Administration
OA	Overall Accuracy
PA	Producer's Accuracy

PCA	Principle Component Analysis
POLSAR	Polarimetric Synthetic Aperture Radar
PCs	Principal Components
PW	Permanent Water
RF	Random Forest
SAR	Synthetic Aperture Radar
SRTM	Shuttle Radar Topography Mission
SVM	Support Vector Machine
S1	Sentinel-1
S2	Sentinel-2
UA	User's Accuracy
Ur	Urban
VH	Vertical Horizontal
VV	Vertical Vertical
V1	Vegetation-1
V2	Vegetation-2

1. INTRODUCTION

This chapter provides thesis motivation and describes problems addressed here, with a discussion of the occurrence and impact of floods. The objectives and outline of the thesis are also presented in the following sub-headings.

1.1. Problem Statement/Motivation

Floods can be described as overflows of water bodies from their usual boundaries or water accumulations in lands which are usually inundated [1]. According to the Intergovernmental Panel on Climate Change (IPCC), types of floods can be listed as river (fluvial), pluvial, flash, urban, coastal, sewer and glacial lakes. Various socio-economic and environmental elements influence the harm sourced from them, such as availability and quality of urban infrastructure, underplanned urban expansion without sufficient analysis of ecological and climatic parameters. The results can be disastrous with extensive loss of lives and biodiversity, natural resources and man-made assets, etc. [2, 3]. Flood events yield to approximately 40% of socio-economic and environment-related losses sourced from natural disasters [4]. As the magnitude and types of damages are related to the location, extent and the inundation level of flooding, the mapping and monitoring of flood hazards are essential to assess their true impact and prepare proper disaster risk management and rehabilitation efforts [5]. Flood dynamics are often difficult to assess with traditional techniques, due to both data limitations and rapid movement of water bodies, which are also often inaccessible [6].

Remote sensing technologies and Earth Observation (EO) data provide the necessary tools and data for the temporary monitoring and assessment of floods affecting large areas. The EO data collected from satellite platforms, both with and without regular coverage scheme, are indispensable in flood hazard assessments as they enable essential

information in inaccessible areas. Regarding the satellite EO data, two main sensing technologies, active with microwave sensors and passive via optical cameras can be listed as enablers for information provision [7]. One of the sensor categories that can serve this purpose is optical sensors that have been used since the early 1970s. Optical sensors are frequently used due to availability with diverse ground sampling distances (GSDs) and acquisition scheme [8]. The other category is based on radar sensors operating at longer bandwidths and thus have the possibility to operate in cloudy weather conditions. In addition, they can penetrate vegetation to some extent. The fact that the radar sensors are not affected by clouds thanks to this ability is one of the most important advantages considering the nature of the flood event. In addition, thanks to its penetration feature, it can supply information about a certain degree below the surface, so it can provide more information about floods that occur in urban, vegetated or forested areas than optical sensors that can only detect the top of surface. The Interferometric Synthetic Aperture Radar (InSAR) and Polarimetric Synthetic Aperture Radar (PolSAR) techniques offer well-known advantages such as the determination of the altered or stable areas with the coherency data it provides, thus surface deformations and scattering mechanism caused by flooding. In summary, various characteristics of Synthetic Aperture Radar (SAR) data products enables identification of several surface properties and enriches our knowledge on Earth. However, unlike optical imagery, SAR data contains phase data but less intensity information in visible spectrum, which makes it less interpretable by human vision. In addition, SAR data require expertise for processing and the interpretation of the results when compared to optical data.

On the other hand, complementary usage of optical and SAR data has a great potential to produce essential features such as color, brightness, texture, shape, surface roughness and smoothness, and water content, etc., to detect flooding in areas with different constructions and topography. Considering the availability of diverse satellite sensors with varying radiometric, spatial, temporal and spectral resolutions and data quality, fusion of heterogeneous information for flood mapping is still an active research area. As the data fusion techniques depend not only source data but also the application in order to meet the quality (e.g., accuracy, reliability, temporal availability, etc.), novel approaches are still needed for fusing optical and radar products for flood mapping and

monitoring to synthesize the advantages of both sensors. Thus, this thesis focused on the development and validation of a feature-level data fusion methodology for flood extent mapping using optical and radar data, in particular by using the Sentinel-1 SAR [9] and Sentinel-2 optical [10] satellites of the European Space Agency (ESA) due to their regular global coverage and free data distribution policy.

1.2. Thesis Objectives

Considering the emerging SAR satellites and processing methods, this thesis aimed at developing an approach for the integrated use of satellite optical and radar datasets based on diverse features produced from both. Considering the processing and interpretation difficulties of SAR data and well-known advantages of spectral indices obtained from optical imagery, this thesis relates with the following objectives:

- Investigating optimal feature types to increase the success of SAR and optical data fusion for flood mapping under various topographical (flat, hilly) and land cover conditions using machine learning (ML) methods;
- Analyzing the accuracy potential of SAR and optical data for flood extent mapping under different data availability scenarios, and propose a strategy, especially for cases where the optical data (i.e., Sentinel-2 imagery) is not available to represent flooding;
- And, proposing a methodology for ML classification to identify flood extent divided into two classes as flooded areas and flooded vegetation.

For this purpose, existing spectral indices and textural feature extraction methodologies were evaluated. In addition, considering the advancements in the ML methods, the performance of Random Forest (RF), which is a decision-tree based supervised classification technique widely used in environmental problems has been evaluated by using different features for regional flood extent mapping. The accuracy was assessed based on three different approaches, such as internal accuracy based on prediction metrics (e.g. overall accuracy (OA), producer's accuracy (PA), user's accuracy (UA), and Kappa

index value (K)), external accuracy using independent reference data, and qualitative assessment with visual inspection.

1.3. Contributions

The main contributions of this thesis can be listed as following:

- A flood extent mapping methodology based on the classification of flooded areas and flooded vegetation using the random forest method is proposed. Several processing strategies with corresponding feature sets are provided depending on the availability of post-event optical imagery.
- As a major outcome, the necessity of using pre-event Sentinel-2 bands and features derived from them has been proven in cases where post-event Sentinel-2 data cannot be used as an input for classification.
- Additionally, flood extent mapping based on ML classification should not be binary and it is recommended to use related land use land cover (LULC) classes including flooded vegetation for obtaining high accuracy.
- The proposed methodology has high accuracy potential and is applicable to different sites under flat, and hilly topographical and land cover conditions for mapping the floods and to assess the damages in agricultural areas.
- Regarding the second and third objective of the thesis, the optimal feature types proposed in the methodology significantly improved the flood observations, especially the flood and flooded vegetation classes. The feature types involve textural features obtained from gray level co-occurrence matrix (GLCM) variables and spectral indices produced for vegetation and water.

1.4. Thesis Outline

In the following chapters, the aforementioned objectives are tackled. Initially, Chapter 2 provides an extensive but non-exhaustive overview of existing SAR-based flood mapping approaches and elaborates on differences and similarities. In Chapter 3, the proposed

methodological workflow, data pre-processing, feature extraction and analysis, decision-making and validation methods are explained in detail. In Chapter 4, the application of the methodology described in the previous chapter to several flood events, some of which include flooded vegetation and an urban area and a dam flood, are given. In Chapter 5, the results of the method applied to three different sites are given and compared in detail in terms of extracted features, utilization of the techniques, and temporal resolution and data quality aspects. Finally, Chapter 6 summarizes the main conclusions of this thesis and suggests potential future research topics that could contribute to increasing the impact of SAR-based flood observations even further.

2. BACKGROUND ON FLOOD INUNDATION MAPPING USING REMOTE SENSING TECHNIQUES

In this chapter an extensive review of existing flood inundation mapping approaches with remote sensing techniques is presented. The studies in the literature using optical and/or radar sensors can be categorized by various basic perspectives such as resolution and wavelength, approaches or methods, land cover components, and flood type. In this context, the literature is mainly explained under the sub-chapters of optical sensors, radar sensors and fusion of optical and radar sensors, emphasizing the types of (resolution and wavelength) optical and radar sensors, respectively. In addition, floods in urban and vegetated areas have been taken into account, as land characteristics are as important as sensor types in the analysis of flood disaster. Most recent studies utilize the use of multi-source data and methods complementarily, rather than a single data and method. For this reason, the main differences of the existing approaches examined from this point of view are discussed.

At the end of this chapter, the main gaps and problems that need to be investigated have been identified based on the literature, and a conclusion has been reached about the gaps that this Ph.D. thesis aimed to fulfill.

2.1. Studies utilizing Optical Sensors

Satellite-based remote sensing is an invaluable tool that supplies broad view about location, extent, severity and susceptibility of floods on any terrain type since the early 1970s [11]. Thanks to these features and being more cost-effective than ground surveys, it has become one of the types of sensors used in flood inundation mapping and also contributes to flood crisis management and post-disaster damage assessments [11]. In this context, optical sensors, the most important advantage of which is spectral information and interpretability compared to SAR sensors, makes a significant contribution to the

determination of low reflective water areas in the near-infrared (NIR) part of the spectrum [12]. Among these sensors, the most frequently preferred ones for flood inundation mapping are given in Table 2.1 by categorizing them according to the geometric resolutions utilized. In the following subsections, literature on flood inundation mapping from optical sensors with diverse spatial resolutions and on different platforms including the remotely piloted aircraft systems (RPAS) has been presented in detail.

Table 2.1. Optical sensors and specifications.

Sensor group	Sensors	Spatial resolution (m)	Agency	Operation
Coarse-resolution	NOAA/AVHRR	1	NASA	1978-today
	MODIS	250-1000	NASA	1999-today
	Suomi NPP-VIIRS	375-750	NASA	2012-today
	MERIS	300	ESA	2002-2012
	Sentinel-3 OLCI	300	ESA	2016-today
Medium-high resolution	Landsat	15-80	NASA,USGS	1972-today
	SPOT	2.5-20	CNES	1986-today
	Aster	15-90	NASA	1999-today
	Sentinel-2 MSI	10-60	ESA	2015-today
Very high-resolution	IKONOS-2	1-4	GeoEye	1999-today
	Quickbird	0.61-2.24	Digital Globe	2001-today
	WorldView-3, 4	0.31-2.40	Maxar	2007-today
	RapidEye	5	DLR	2008- today
	ZY-3	2.1-5.8	CRESDA	2012-today
	GF-1/GF-2	1-16	CRESDA	2013-today

2.1.1. Coarse-resolution satellite sensors (> 250 m)

Although the coarse-resolution satellite sensors usually have the mission to monitor the atmosphere and ocean, they have also been used to detect large-scale flooding events due to their high temporal resolution and wide coverage [8]. The first research in this context used visible bands and some index from VHRR (Very High Resolution Radiometer) and AVHRR (Advanced VHRR) optical data at 1 km spatial resolution [8]. Many studies have been carried out to analyze the ability of National Oceanic and Atmospheric Administration/The Advanced Very-High-Resolution Radiometer (NOAA/AVHRR) to studying very large river floods [13, 14], using color composites for visual analysis [15].

It has been highlighted that the sensor suffers from extensive cloud distribution, especially during flood events [15-17].

The globally available and free Moderate Resolution Imaging Spectroradiometer (MODIS) data, which was operational in 2000 and available from the National Aeronautics and Space Administration (NASA), has been broadly operative in many areas such as LULC change detection and atmosphere monitoring. At the same time, the capacity of MODIS data in processes such as flood extent detection, disaster response and damage assessment was investigated by many studies [18-20]. Due to their low spatial resolution, which ranges from 250 m to 1 km, they are not optimal for detecting flooded area on a fine scale. In spite of the resolution limitations, many studies that use the MODIS data for flood inundation mapping or prevent research [21, 22]. Additionally, a large archive of floods extracted from MODIS was provided by Near Real-Time Global Flood Mapping Project by NASA and the Dartmouth Flood Observatory throughout the world [20, 23].

Another sensor in this scope is the Visible Infrared Imaging Radiometer Suite onboard Suomi National Polar-orbiting Partnership (Suomi NPP-VIIRS), which has 22 bands and was released in 2011. With the potential to generate near real-time (NRT) information thanks to its high temporal resolution, this sensor is used for the flood inundation mapping. In addition, ESA has been effective in land and ocean monitoring such as MEdium Resolution Imaging Spectrometer (MERIS) and Ocean and Land Color Instrument (OLCI) on board Sentinel-3, which was operated in 2016, and supplies 21 spectral bands at 300 m spatial resolution. This sensor, which is mostly used in the literature for the analyzing of water dynamics, is increasingly being used for flood activities thanks to its high revisit time and area coverage [24-26].

2.1.2. Medium-resolution satellite sensors (> 10 m)

With its optical sensors, which started in 1972 with Landsat-1 Multispectral Scanner (MSS) and upgraded to Thematic Mapper (TM) on Landsat-4 and Landsat-5, to Enhanced

Thematic Mapper Plus (ETM+) on Landsat-7, and finally to Operational Land Imager (OLI) on Landsat-8. Landsat have been providing data for over 45 years, has a successful history in the medium-resolution sensors group. While most of the pioneering studies in flood mapping with Landsat-1 has been performed in Arizona, Virginia and along the Mississippi River [27-29], Landsat data continues to increasingly contribute to flood activities with the OLI sensor becoming operational in 2013 [30-32].

Although Systeme Probatoire d'Observation dela Tarre (SPOT) has a higher spatial resolution than Landsat data, its application has been limited owing to its not being free of charge, and therefore there are few studies using SPOT for analyzing flood activities [33, 34]. Sentinel-2, the most preferred sensor within this group, provides global coverage of the Earth's surface every 12 days with one satellite and every 6 days with two satellites with spatial resolutions ranging from 10 to 60 m. The use of Sentinel-2 data, which potential has been investigated in many flood inundation mapping studies [35-38], has been increasing, especially thanks to its complementary advantageous with Sentinel-1 SAR data.

2.1.3. Very high-resolution satellite sensors (< 2 m)

Significant progress has been made in improving the spatial resolution of sensors over the past decade, and most of the new sensors, such as IKONOS (Sharma et al., 2022), Worldview, RapidEye, Worldview-2, Quickbird [39], ZY-3 [40], and GF-1/2, can supply data at meter or sub-meter level spatial resolution. At this resolution level, even small water bodies can be successfully detected, but such sensors have some limitations such as small scene coverage, shadow effect in especially urban and roughness areas and low temporal resolution [41].

Despite these limitations, studies aiming at flood analysis, monitoring and management from high resolution data are abundant. A comprehensive analysis of these studies was carried out by Munawar et al. [42] and it was summarized that the sensors in this category

generally produce high-accuracy results, but they have disadvantages in time-series analyses due to their low temporal resolution.

In recent years, the increase in nanosatellites with very high spatial resolution has eliminated the temporal resolution limitation of high-resolution data, and this has greatly contributed to disaster activities. For example, the potential for flood mapping of CubeSat data from a constellation of small satellites, which provides global data with high spatial and temporal resolution, has been explored in many studies [43, 44].

2.1.3. Very high-resolution satellite sensors (< 2 m)

Nowadays, Remotely Piloted Aircraft Systems (RPAS) (also known as unmanned aerial vehicles - UAV) have great potential in scientific applications, from agriculture and environmental science (e.g., wildlife, water, air, forest) to oceanography, archeology, and natural disaster-related studies [45]. In the case of flood disasters, it is clear that the RPASs are one of the technology-oriented platforms that can support many such activities, especially detection, and response. RPASs thanks to providing highly detailed images that optical and radar sensors cannot provide for a variety of reasons are specifically often used in flood analysis in urban areas [46].

Popescu et al. [47] proposed a methodology including texture measurements for the analysis of flooded areas from RPAS images. Afterwards, Gebrehiwot et al. [48] investigated the potential of CNN approaches to extract urban flooded areas from UAV imagery. In the study, it was stated that CNN-based classifiers are very useful for flood segmentation with a Kappa index of 0.9. Karamuz et al. [49] proposed a procedure for updating hydrodynamic model boundaries with RPAS data. In the study, it was emphasized that the proposed approach is very effective for updating and validating flood risk maps on-line. In the recently published bibliometric review by Iqbal et al. [50], it was emphasized that especially the RPAS technology provides advantages in critical activities such as flood inundation and surface water mapping, and damage assessment.

In summary, the experimental results of the studies reviewed showed that the use of RPASs in flood analysis produced promising results, despite the availability of sufficient RPAS data to apply various methods. While drones were predominantly preferred for data collection in previous research on flood analysis and mapping, in recent years, drones equipped with high-resolution multi-spectral (MD), LiDAR, and radar sensors have been used. It should be noted that UAV data, which is particularly advantageous in dense urban flooding, has some difficulties in areas where the terrain is covered by high vegetation or shadows.

2.2. Studies utilizing Microwave Sensors

In addition to optical imaging, the microwave sensors as an alternative satellite-based remote sensing data type provide an invaluable tool that has been used in flooding activities since the early 1977s and has been increasingly used today [11]. In this context, SAR sensors, which are least affected by weather conditions (day & night-time) and can provide continuous data about the roughness and surface characteristics of the mediums compared to optical sensors, are advantageous in flood mapping thanks to these specifications [51-53]. SAR sensors with different information levels and resolutions and named P, L, S, C, X, Ku, K and Ka according to wavelengths in the range of 100 - 0.6 cm, have been preferred especially in areas with different requirements and features such as urban floods, flooded vegetation, and river floods. Accordingly, in the following subsections, the literature on the most commonly used X, C and L sensors in flood mapping is presented in detail.

Table 2.2 summarizes the state-of-the-art literature since the early 2000s, mainly aimed at producing flood inundation maps using SAR data. Especially, for each research in the Table, specific features of the landscape analyzed, data used, methods or approaches, and validation processes have been listed, along with the key results. In addition, it must be stated not every study provided quantitative results.

Table 2.2. Most frequently used radar sensors and their specifications for flood activities.

Band	Sensors	Agency	Operation	Polarization
X	TerraSAR-X/ TanDEM-X	DLR	2007-today 2010-today	quad
	COSMO- Skymed-1/4	ASI/MiD	2007-today	quad
	RISAT-1	ISRO	2012-today	quad
	Kompsat-5	KARI	2013-today	dual
	PAZ	CDTI	2013-today	quad
C	ERS-1/2	ESA	1991-2000 /1995-2011	VV
	Radarsat-1	CSA	1995-today	HH
	SRTM	NASA/DoD, DLR, ASI	2000-today	C(HH+VV) X(VV)
	Envisat-1 ASAR	ESA	2002-2012	dual
	Radarsat -2	CSA	2007-today	quad
	Sentinel-1A/1B	ESA	2014-today	dual
L	Seasat	NASA/JPL	1979	HH
	JERS-1	JAXA	1992-1998	HH
	ALOS/PALSAR	JAXA	2006-2011	quad
	ALOS-2	JAXA	2013-today	quad

2.2.1. X-band Satellite Sensors

The X-band, which is called high-resolution SAR, which varies in the wavelength range of 2.4 – 3.75 cm of the electromagnetic spectrum, is often preferred in studies such as urban monitoring, agriculture, ice and snow investigation. X-band sensors have a shorter range than the X- & C-bands and do not have sufficient coherency in flooded areas and flooded vegetation. Thus, they are disadvantageous compared to other sensors in terms of penetrating vegetation [54].

When it comes to flooding, the most used X-band sensors are TerraSAR-X and COSMO-SkyMed satellites operated by German and Italian institutions/companies, respectively. One of the first studies under this title conducted by Martinis et al. [55] combines thresholding and segmentation and presents an automatic near real-time (NRT) flood identification approach. Experimental results on urban and agricultural areas with 3 m resolution TerraSAR-X datasets, together with the optional integration of digital elevation model (DEM), demonstrate the high classification accuracy of the proposed approach. A subsequent study led by Mason et al. [56] recommended to use digital surface model

(DSM) in urban areas for the elimination of layover and shadow effects with the same datasets. The same TerraSAR-X dataset was then used in a subsequent series of case studies [57-59].

These studies have highlighted that areas with various structures and heights of buildings, green or vegetated lands, and different street topologies have different SAR signal characteristics, and studies have focused on investigating the backscattering characteristics of different urban structures. Research works conducted in this context have generally produced promising results using SAR intensity data as well as coherency, InSAR and PolSAR information [60-66].

2.2.2. C-band Satellite Sensors

The C-band varies in the wavelength range of 3.75 – 7.5 cm of the electromagnetic spectrum and is often preferred in studies such as global mapping and monitoring (i.e. land, ice, and ocean) and multi-temporal analysis. C-band sensors, which have a longer range than the X-bands, supply more sufficient coherency and penetration capacity. Among these group, Sentinel-1 is the most preferred sensor and has a C-Band SAR instrument with a wavelength of around 5.7 cm and four observation modes [10].

One of the first studies under this title was conducted by Twele et al. [67] proposed a combination of automatic tile-based thresholding and fuzzy-logic for improving the results by eliminating potential water-like pixels. Study results indicated that the thematic accuracy of vertical transmit-vertical receive (VV) polarization is slightly higher than vertical transmit-horizontal receive (VH) polarization. It was emphasized that the robustness of the processor for various wind levels and other environmental factors still needs to be confirmed. Martinis [68] proposed an approach in arid areas, where accurate SAR-based water mapping is usually not possible. Using statistical metrics from the Sentinel-1 time-series to eliminate water-like pixels with could be mixed with sand surfaces, the study highlights that the algorithm can significantly improve the classification accuracy of the Sentinel-1 flood processing chain. In addition, Martinis [69] proposed a method called Sentinel-1 time-series-based Sand Exclusion Layer (SEL) for

near real-time flood extent mapping. The study emphasized that the best results require longer time series interval to generate the SEL in the 60-100% frequency range.

Amitrano et al. [70] proposed a framework based on GLCM features combined with intensity data in a fuzzy classification and a change detection applied to Sentinel-1 Ground Range Detected (GRD) product. Results emphasized that the fuzzy classification applied using Haralick et al. [71] textural features specifically homogeneity and contrast gave good performance. While texture features that provide additional information vary depending on the study area and the data used in terms of parameter and feature selection, the method using the change index requires further validation. Li et al. [72] have proposed a reference selection procedure with high similarity with multi-temporal images and low similarity with flood image. Although these methods provide a better reference than the manual selection, they are constrained in time and computationally. Tavus et al. [73] proposed an approach that includes urban flood mapping using only Sentinel-1 data. The method, which basically includes change detection and thresholding, recommends the use of one post-event acquisition and at least two acquisitions representing pre-event conditions.

2.2.3. L-band Satellite Sensors

The L-band, which is called medium-resolution SAR varies in the wavelength range of 15 – 30 cm of the electromagnetic spectrum and is often preferred in studies such as geophysical monitoring, biomass and vegetation mapping. L-band sensors, which have a longer range than the X- & C-bands, achieve greater penetration into a medium such as forest, soil and ice. Such sensors are preferred in the analysis of forested or vegetated floods, as they allow greater interaction between the radar signal and large branches and tree trunks in a forest.

Among this category, the Japanese Earth Resources Satellite (JERS) and the Advanced Land Observation Satellite (ALOS) from JAXA are the most preferred ones. In this context, studies that started in the Amazon [74-76] and Congo basin [77] continue with successful applications today. The most important handicap of L-band SAR sensors, which have been evaluated in many studies for purposes such as urban flooding, flood

depth estimation in agricultural lands, mapping flooded vegetation with polarimetric information, has limited access to data due to the lack of open source policy [78-82].

2.3 Studies utilizing both Optical and Radar Data

Three combinations of optical and SAR data have been usually preferred in the literature, which is applied to pre-&post flood events, respectively. The combinations can be listed as optical and optical, SAR and optical, and SAR and SAR sensors. The combination of SAR and optical is more favorable considering the requirement for timely assessment of floods that rapidly change their dynamics. Recently, various approaches have been used in the literature for flood mapping using multi-temporal and multi-source data [83]. However, as noted in the previous sections, the complementary nature of SAR and optical data has brought this concept to the fore and made it a preferred research topic [84].

Martinis et al. [85] proposed a two-phase methodology that included flood services from MODIS Flood Service (MFS) and TerraSAR-X Flood Service (TFS) and the presentation of information via a web-based user interface. The study is important in that it is one of the first studies that includes the fusion of optical and high-resolution SAR data and serving via a web portal. Tong et al. [84] presented a methodology for flood monitoring that combined both Landsat 8 and COSMO-SkyMed data. The proposed method is based on the change between before and after flood event based on Landsat-8 data by using SVM and the COSMO-SkyMed data by using active contour model, respectively. In the study, it was stated that the highest overall accuracy (OA) was obtained from Landsat-8 data with 97%, with a difference of 3% compared to SAR data. DeVries et al. [86] proposed a fully automated and real-time flood inundation mapping approach using Sentinel-1 time-series and Landsat data on the Google Earth Engine (GEE) platform. The approach has been applied to different areas and has been validated using external reference sources such as Planet and Copernicus Emergency Mapping Service (EMS) with at least 95% OA. Benoudjit and Guida [87] used the TerraSAR-X, Sentinel-1&2 dataset with a supervised classifier for automated delineation of flood extent, but it was stated that the classifier failed in relatively small water areas compared to the study area.

Optical and SAR data fusion approaches for flood mapping in the literature usually preferred Sentinel-1&2 data as they are freely available and can count global data at regular intervals. These advantages of the data in question make it very attractive to explore their potential with the development of data processing algorithms. Most of the studies in this scope have used indices such as Normalized Difference Vegetation Index (NDVI) and Normalized Difference Water Index (NDWI) from optical imagery as a complement to SAR data. For example, Sunar et al. [88] proposed a methodology in which NDWI time series generated from optical data such as Landsat-8, Sentinel-2 (S2), and Sentinel-1 (S1) are evaluated based on thresholds. The results, which were compared with different data sources such as meteorological and river bed flow, showed that there are two major reasons for flood events in the research area and the damage rates they can cause are different. In Bioresita et al. [89], a decision-level fusion approach were used to combine multi-temporal NDWI indices produced from S1 & S2. In the study comparing single-date and multi-temporal analysis, it was stated that the decision-level fusion of S1 & S2 provided better results for permanent water and has a high potential for flood mapping.

Huang and Jin [90] proposed a flood detection approach that analyzes LULC data generated from S1 & S2 with a pixel-based change assessment and thresholding method and achieved an OA of 81%. However, there were some limitations such as the determination of LULC types representing the entire study area from the S1 data and the necessity for pre-information about the backscatter distributions of the relative surfaces in dry and wet conditions. In addition, it has been reported that activities such as agricultural irrigation, which require pre-information and processing, cause false alarms in the results. Manakos et al. [91] proposed a pixel-based random forest (RF) classifier trained with samples generated from S1-based features and S2 flood map classes. In conclusion, it was emphasized that the increase of the considered S2 maps enabled the prediction of S1 flood maps with higher accuracy. Slagter et al. [92] used multi-level RF classifier for fusing S1&S2 for flood inundation segmentation. The results showed that although using S1&S2 together led to considerably higher accuracies, relatively poor for classifications in high-vegetated wetlands, as sub-canopy flooding.

Singha et al. [93] analyzed the multi-temporal flood patterns and paddy lands that could be damaged by flooding in Bangladesh from Sentinel-1&2 by using change detection and

thresholding approaches SAR images in the GEE platform. Hakdaoui et al. [94] presented an approach that includes Sentinel-1 for the detection of the water extent and soil roughness, and S2 and Landsat-8 data for analyzing the soil moisture after the flood. The results of the study which that based on the change of spectral features and Support Vector Machine (SVM) classifier showed the importance of combinations of different sensors and approaches outperforming flood-affected wetland areas monitoring. Hakdaoui and Emran [95] proposed an approach aiming at the flood extent delineation caused by heavy rainfall on the Sakia El Hamra dam failure case in Southern Morocco. The results from the study, based on the change analysis of spectral indices and segmentation from S1&S2 and Landsat-8, demonstrate the importance of complementary multi-sensor images for flood inundation mapping.

Tripathi et al. [96] used S1&S2, MODIS imagery and precipitation data for Near Real Time (NRT) flood inundation mapping. Land/water data produced separately from S1 and MODIS images were compared with precipitation data and LU/LC produced from S2, and agricultural areas under flood were analyzed. However, no accuracy assessment was made in the study. The study by Sherpa et al. [97] used S2, Landsat-8 and MODIS data for the validation of probabilistic flood maps produced from S1 data using a pixel-based Bayesian approach, emphasizing the usability of the approach for rapid flood response purposes. Lal et al. [98] investigated a correlation between spatio-temporal pattern of satellite-based precipitation and a S1-based flood inundation map by using thresholding and an RF approach. The results of the study revealed the necessity of increasing ecological stability and resistance to flood hazards for some regions.

Konapala et al. [11] used a deep Convolutional Neural Network (CNN) known as U-Net to evaluate the potential of various bands of S1&S2 images and different combinations of water indices. Datasets containing only S1 bands and height information with S1 achieved an F1 score of 0.62 and 0.73, respectively. Among all combinations, the Hue, Saturation, Value (HSV) transformation of the S2 provided a median F1 score of 0.9, thanks to the superior contrast discrimination capabilities. In their study, Bai et al. [99] introduced a deep learning (DL) method for mapping permanent and flood water using S1&S2 data on the Sen1Floods11 benchmark dataset, achieving an OA value of 92.8%. Gašparović and Klobučar [100] implemented an object-based approach that combined

Sentinel-1&2 data for forest flood detection, achieving an OA value of 95% by incorporating various GLCM and vegetation features.

In support of operationalizing flood segmentation on a global scale using U-Net deep learning algorithm, Muszynski et al. [101] proposed semantic flood segmentation, making the approach largely immune to geographic differences around the world. Results show the segmentation model with a level of 95% F1 score for both non-water and water classes, and 53% F1 score for water class, respectively on unseen flood events. Jenifer et al. [102] presented an AgriFloodNet (dual patch CNN model), learning the permanent water and flood classes from S1&S2, for the detection of flood-affected agricultural areas. The proposed model provided 96.88% and 91.11% OA, respectively, from the SEN12-FLOOD benchmark data.

2.4. Studies utilizing Machine Learning Methods for Flood Mapping

SAR and optical-based flood mapping studies consist of several different approaches such as thresholding (global, split-based, fuzzy and multi-temporal), image segmentation, change detection, supervised and/or unsupervised learning methods.

2.4.1. Thresholding

The most basic and simple technique for rapid flood inundation mapping is image thresholding [52, 103]. Although the main difficulty in the thresholding method is user-dependence of the parameters, there are also some limitations in flood mapping from SAR data [55]. These are atmospheric disturbances [104], double-bounce effect due to underwater vegetation or building [105], dry and smooth bare soil or shadow with a backscatter water-like surfaces and soil moisture content [53, 106, 107]. Furthermore, selection of threshold values rely on both the flood size and the reparability between the flood and non-flood pixels. Thresholding can cause errors, especially when rough water surface due to wind is occurs, and when flooded area is small relative to the working area.

Thresholding methods, which are basically based on the solution of the problems mentioned, can be evaluated in four groups as global, split-based, fuzzy and multi-temporal thresholding. Global thresholding, which is an efficient and probably the simplest approach to image binarization, is based on class-variance in a mono image. One of the most well-known of these algorithms is the Otsu thresholding method introduced by Otsu [108], which works by minimizing the interclass variance, and based on bimodalities of the distribution of pixel values. In various studies in the literature, the Otsu algorithm has been used with complementary methods for SAR-based flood mapping [109-112]. In addition, algorithms such as Kittler & Illingworth (KI) and Minimum Cost Entropy based on threshold optimization problems are frequently used in this context [55, 67, 113, 114].

In order to overcome the aforementioned disadvantages of global thresholding methods, split-based approaches have been introduced that determines a representative area for selection of optimal threshold firstly. Martinis et al. [55] introduced segmenting the SAR image into tiles by using bimodal local histograms. In the study, tiles having a bimodal histogram, including water and non-water classes, were applied for KI threshold selection. Chini et al. [115] also proposed a similar adopted tiling approach to identify bimodal areas in an image. In their study, it was emphasized that the separability between flooded and non-flooded areas is clearer when the coefficient is higher than 2.

For similar purposes, namely to improve the contrast between flood and non-flood pixels, Schlaffer et al. [116] introduced an approach that masks areas that are not likely to be inundated. A threshold value (10 m) determined by using the Height Above Nearest Drainage (HAND) index was applied to mask areas with a high probability of flooding, but it was stated that it should be selected according to the topography of the region. Similarly, using the HAND index for post-processing, Twele et al. [67] suggested a value of 15 m as the global threshold, while Clement et al. [117] and Bioresita et al. [89] also suggested a threshold value of 20 m, adding some slope restrictions.

In the literature, fuzzy logic approaches firstly introduced by Zadeh [118] have been frequently preferred to investigate floods in vegetated or forested areas, unlike the two methods mentioned above. Pulvirenti et al. [119] evaluated different datasets such as DEM and land cover map in addition to SAR data with a fuzzy logic approach and

suggested an approach for detecting flooding in vegetation, forest and urban areas. On account of the threshold values being calculated from only a few flood events, even if the problems that may occur when the preconditions of the models are not satisfactory can be eliminated by manual intervention this situation can cause a lack of automation in the process. Amitrano et al. [70] proposed two methods aiming to identify floods from the archive of Sentinel-1 SAR images with automatic fuzzy classification based on textural features and change index. While textural features provide additional information, they vary depending on the study area and the data used in terms of parameter and feature selection. Thus, the method using the change index requires further validation. Dasgupta et al. [120] applied a similar approach, which includes texture optimization and neuro-fuzzy classification to a single COSMO-SkyMed data and it was stated that the proposed approach has the potential to improve operational SAR-based flood mapping. In addition, Grimaldi et al. [121] proposed a method that includes evaluating the thresholds representing wet and dry vegetation, calculated using probability binning, with a fuzzy logic approach.

One of the main approaches in determining the optimum threshold value is based on the analysis of variation of statistical information generated from multi-temporal SAR data. Cian et al. [122] proposed the methodology consisting of change detection analysis of multi-time statistics. In addition, as a result of the study using the Normalized Difference Flood Index, a constant threshold of the index is determined to detect the flooded areas.

2.4.2. Change detection

Despite change detection techniques can overcome some limitations of thresholding methods and significantly improve the results, they have some additional limitations [57]. In these techniques, the selection of a reference data acquired from the same acquisition geometry is crucial to avoid changes due to geometric effects and the risk of underestimating the size of the event [123]. Another important issue in the reference selection is the seasonal effects, which can significantly change the backscatter and can be perceived as a change, especially in areas with vegetation [124]. It is possible to distinguish the flood backscatter areas from others with the reference images selected considering these considerations.

The most practical approach to reference image selection is to select the first available non-flood image that satisfies the required conditions [123]. However, with the increase in SAR archive data, different approaches have been developed based on the statistical analysis of image time series. Schlaffer et al. [116] have been analyzed backscatter characteristics under flood and non-flood conditions with harmonic analysis of a multi-temporal ENVISAT ASAR. Li et al. [72] have proposed a reference selection procedures with high similarity with multi-temporal images and low similarity with flood image. Though these methods provide a better reference than manual selection, they are time consuming and have high computational costs.

2.4.3. Supervised & unsupervised learning

Supervised classification methods require a dataset including labeled flooded areas and their corresponding pixels in SAR and optical data. A number of studies applied supervised and unsupervised learning methods to tackle flood extent mapping problems with SAR. One of the first studies in this category was performed by Pulvirenti et al. [119]. They introduced a semi-automatic fuzzy logic classifier, which used thresholds for classifying pixels automatically or using labeled data. Although the method proved to be quite accurate, it was emphasized that automatic classification needs a scattering model and causes modeling uncertainty. Skakun [125] used a self-organizing map (SOM) for segmentation and classification of SAR data. The approach applied to three different SAR sensors such as ERS-2/SAR, ENVISAT/ASAR and RADARSAT-1, yielded 85%, 98% and 96% OA, respectively, using independent test datasets.

Notti et al. [126] presented a semi-automatic and manual approach by using a multi-sensor (S1&S2, Landsat-8, MODIS, and Proba-V) for flood inundation mapping. Supervised classification techniques such as maximum likelihood and spectral angle methods have been performed on different configurations of mentioned datasets. Results showed that the availability and the combination of S1&S2 and Landsat-8 data together with ancillary data (DEM and geomorphological) was essential to flood mapping.

Tanim et al. [127] proposed to flood inundation mapping approach using different supervised and unsupervised ML models, such as RF, SVM, and Maximum Likelihood

Classifier (MLC). F1-score from the RF, SVM, MLC, and CD models show 0.67, 0.85, 0.79 and 0.85. Wang et al. (2022) utilized a CNN model called MultiSenCNN for LULC classification and flood inundation mapping using optical, panchromatic and SAR datasets. The results showed that the OA of the combination of optical and SAR data is slightly higher than the optical and panchromatic data, highlighting that the flood result covering mostly crop and urban land is produced with a Kappa of 0.94.

In summary, supervised classification techniques are frequently preferred for binary or multivariate classification challenges. These methods, such as the K-Nearest Neighbor Classifier, the RF classifier [128], SVM [129], and ANN classifier [130-132] have been used to SAR and optical images for flood inundation mapping. The prediction performances depend on the characteristics of the site and input feature.

3. METHODOLOGY

In this chapter, the methodology proposed in the thesis is explained. The chapter begins with a description of the overview of proposed workflow, continues with explanations of the data pre-processing required prior to the analysis of Sentinel-1&2 data, feature extraction and selection, modeling, mapping and validation.

3.1. Satellite Sensors

In this section, characteristics of three sensors, i.e., Sentinel-1, Sentinel-2 and PlanetScope, from which data were utilized here are explained briefly.

3.1.1. Sentinel-1 Sensor Characteristics

The main purpose of Sentinel missions is to improve Global Environment and Security Monitoring (GMES) services by continuously monitoring the environment and to collect data similar to that of the European Remote Sensing satellite (ERS), Environmental Satellite (Envisat), and SPOT/Landsat, with improved capabilities [133]. Each Sentinel mission consists of a constellation of two satellites, denoted as A and B. Sentinel-1A was launched on 3 April 2014 and Sentinel-1B on 25 April 2016. However, Sentinel-1B data has not been available since January 10, 2022, due to an anomaly that resulted in a loss of data transmission [9]. For this reason, the Sentinel-1A satellite has the potential to map global land masses using the Interferometric Wide (IW) swath mode every 12 days through a single pass, be it ascending or descending.

Sentinel-1 satellites are equipped with a C-Band SAR instrument payload, operating at a wavelength of nearly 5.7 cm. These satellites operate in four different observation modes,

namely Stripmap (SM), IW Area (standard mode), Extra Wide (EW), and Wave, depending on the satellite's position and the scope of the observation. The sensors offer four distinct combinations of vertical (V) and horizontal (H) polarization (i.e., VV, HH, VV + VH, and HH + HV) data. In this section, characteristics of the sensors used in this thesis are briefly explained.

3.1.2. Sentinel-2 Sensor Characteristics

Sentinel-2 satellites are equipped with optical instruments comprising 13 multi-spectral bands, capturing images at spatial resolutions ranging from 10 m to 60 m across the wavelengths from 443 nm to 2190 nm. [133]. In the Sentinel-2 satellites, the visible and NIR bands have a GSD of 10 m. The vegetation red edge and short-wave infrared (SWIR) bands have a 20 m, while the coastal aerosol, water vapor, and cirrus bands have a GSD of 60 m [10]. The temporal resolution of Sentinel-2 constellation are 5 days, and each satellite has a revisit frequency of 10 days.

3.1.3. PlanetScope Sensor Characteristics

The PlanetScope satellite constellation, which is operated by Planet Labs Inc., acquire images with a ground sampling distance (GSD) of 3.7 m [134]. This satellite has the capability to collect images of the entire land surface of the Earth every day, with a daily collection capacity of 200 million km²/day). PlanetScope imagery products are available in 3 levels: Basic Scenes (Level 1B), Ortho Scenes (Level 3B), and Ortho Tile (Level 3A). The Level 3B products have three visible RGB and one near-infrared band and are processed orthorectified, scaled Top of Atmosphere Radiance image products suitable for analytic and visual applications [134]. PlanetScope orthoimages exhibit an approximate spatial resolution of 3 meters and demonstrate positional accuracy with root mean square error (RMSE) values better than 10 meters [134].

3.2. Overview of the Proposed Workflow

In this thesis, the proposed method is based on the analysis of S1 & S2 data acquired before and after a hazard event as shown in Figure 3.1. The methodology was developed by using the Sardoba dam failure case, which is the first study area for which pre- & post-event S1 & S2 data are available, and then applied to the Ordu flood case, which was previously mapped with a preliminary version of it [135]. Since Sentinel-1 data is presumably not affected by weather conditions, the main limitation remains in the temporal resolution, i.e. finding suitable data that corresponds to flood event time. Specifically concerning the flood hazard, the fact that Sentinel-2 data is affected by weather conditions is the most important limitation of many flood mapping cases. In this context, the proposed methodology considers data availability, which is one of the major limitations, and analyzes auxiliary features for flood extent mapping with S1 & S2 data.

The methodology applied here consists of three main stages as (a) data pre-processing, (b) feature extraction and selection, and (c) modelling, mapping and validation, as illustrated in Figure 3.1. In the first stage, a number of methods were applied to correct S1 & S2 data radiometrically and geometrically. For feature extraction, GLCM texture measurements first presented by Haralick et al. [71] were applied to pre- & post-event S1 & S2 band data. In addition, spectral indices such as NDVI and modified NDWI (MNDWI) were produced from pre- & post-event optical (S2) images. For selecting optimal features, Principle Component Analysis (PCA) was applied to the GLCM textural features for reducing dimensions. After the PCA, instead of GLCM variables, their principle components (GLCM PCs) were integrated as supplementary data to the original S1 VV and VH bands and S2 RGB, NIR and SWIR bands. At this stage, the features were organized into different data stacks to investigate the effects of both data availability scenarios and impact of different features on the prediction performances. In each data stack, which consists of different data combinations, the training data delineation strategy is different as the data availability scenario is also different. This aspect is further explained in the following sections. At the last stage, the RF method (Breiman [136]) was applied to learn from the data created in the previous stage. The classification results were

validated by using pixels within test polygons delineated on external reference data (such as PlanetScope).

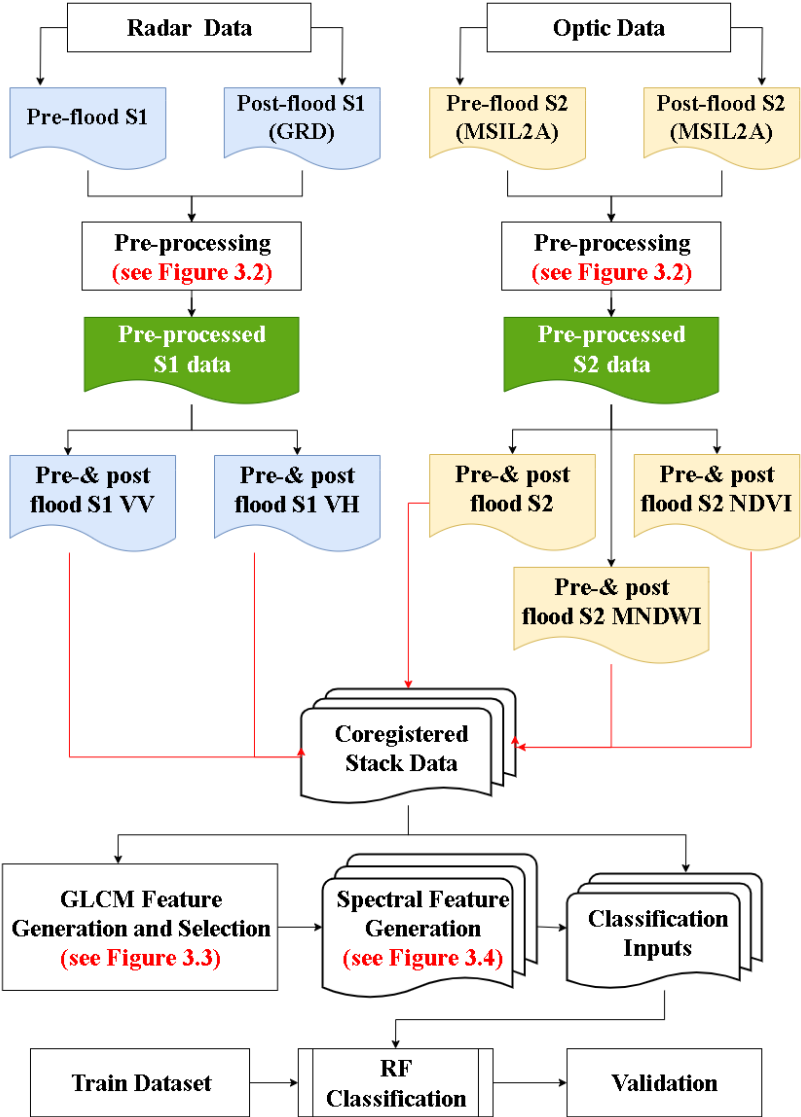


Figure 3.1. Overall methodological workflow.

3.3. Data Pre-processing

Pre-processing of satellite image products is essential for the data to represent real value and can be utilized in multi-temporal or multi-sensor analyses. A pre-processing chain applied for the processing and interpretation of Sentinel-1 SAR and Sentinel-2 optical data SAR is given in Figure 3.2. As shown in the figure, Level-1 IW mode and Sentinel-1 GRD pre-processing steps consist of radiometric calibration, terrain correction, speckle filtering, shadow and layover masking. Radiometric calibration of SAR data provides the opportunity to be compared with different datasets obtained by another or the same sensor, by converting pixel values into physically meaningful measurements [137]. Thus, pre- & post-event S1 GRD images were calibrated to represent radar backscatter and σ_0 bands were generated.

SAR data typically have geometric distortions, such as shadow, layover and foreshortening, caused by topographic variations and the side-looking viewing angle of the satellite sensor. For the elimination of such distortions, the pre- & post-event Sentinel-1 data have been terrain-corrected and orthorectified using the Range Doppler Terrain Correction algorithm. SRTM-1Sec has been used as the DEM with a bilinear interpolation resampling. In addition, the 2-pass method proposed by Schreier [138] have been applied to orthorectified image to eliminate the shadow effect considering the fact that no information is obtained from back slopes. At this stage, if it is necessary to mosaic images taken from different tracks, the backscatter coefficients are converted from the dB scale to the original linear scale and it is important to normalize them according to the incidence angles. For this purpose, different backscatter normalization techniques can be used such as angular-based radiometric slope correction.

One of the most important problems preventing the interpretation of SAR images is speckle noise caused by the random effects of multiple backscattering mechanisms that may occur in each resolution cell [139]. Filters such as Boxcar, Mean, Median, Lee, Lee Sigma and Gamma-MAP have been developed in SAR images to reduce noise caused by the nature of the data acquisition methods. In this context, Lee and Lee Sigma filters have been used frequently in the literature to eliminate speckle noise and have come to the fore

in flood analysis [73, 140, 141]. In Tavus et al. [73], for determining the optimal kernel size, VV and VH pre- & post-event Sentinel-1 data were applied Lee sigma filter with a (3 x 3), (5 x 5), (7 x 7) and (9 x 9) filters, respectively. The effect of kernel sizes on homogeneous surfaces such as lake surfaces was analyzed and it was stated that the 7 x 7 kernel size performed better than the other three filters. In this thesis, a (7 x 7) kernel size Lee Sigma filter was applied for speckle filtering, based on the relevant literature and the analysis results by Tavus et al. [73].

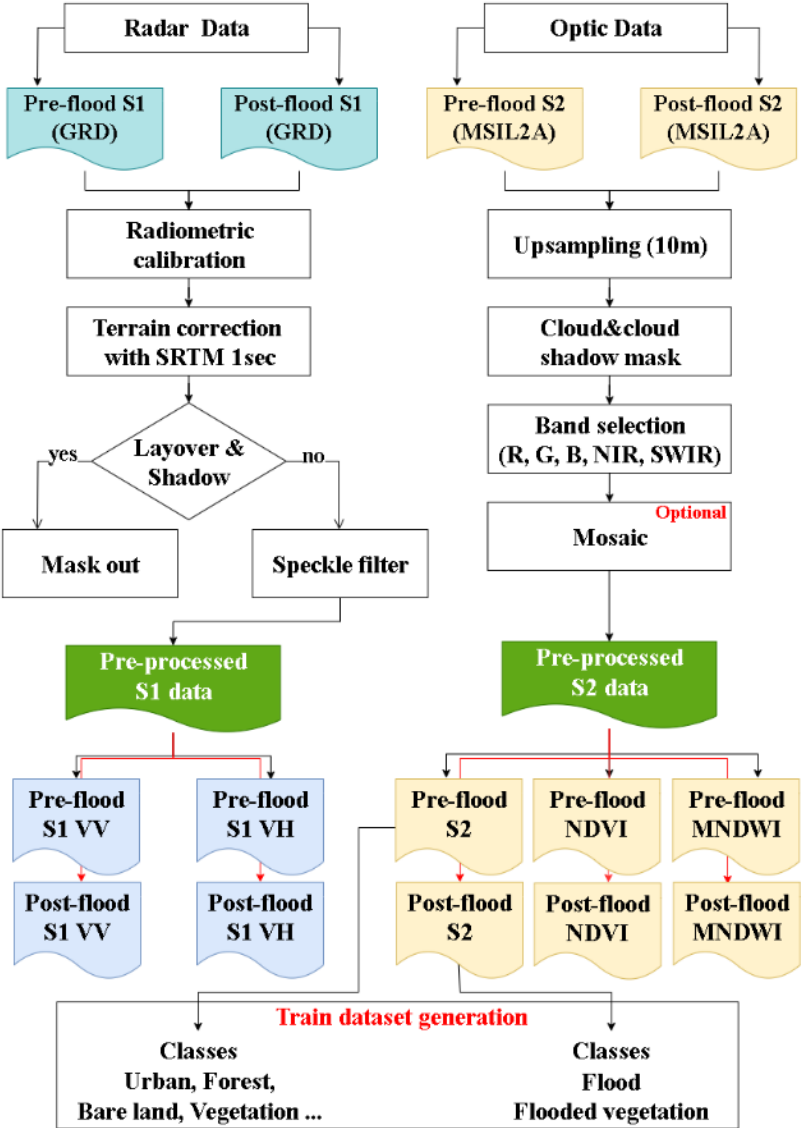


Figure 3.2. Pre-processing of the Sentinel-1&2 data.

Sentinel-2 involves 13 spectral bands as Blue (B2), Green (B3), Red (B4), and NIR (B8) at a spatial resolution of 10 m, Vegetation Red Edge (B5, B6, B7, B8A) and SWIR (B11, B12) of 20 m and Coastal Aerosol (B1), Water Vapour (B9), and SWIR (B10) of 60 m. In this thesis, B2, B3, B4, B8 and B11 bands of Sentinel-2 have been used. Since the SWIR band has a spatial resolution of 20 m, it was upsampled at 10 m for the use together with the other bands. The data to be analyzed in flood events generally need to be eliminated from cloud and cloud shadow areas. For this reason, cloud and cloud shadow pixels mask out the data by using medium and high probability cloud and cloud shadow masks freely available from Sentinel-2.

Pre-processed pre- & post-event Sentinel-2 data have been used to generate of training dataset, which is given as a final step in Figure 3.2. In order to determine the training data required for the classification, in case of post-event and usable Sentinel-2 data, LULC classes and training data in the study area were manually delineated from this data. In particular, training data of flood and flooded vegetation classes were produced from pre-processed post-flood Sentinel-2 data, while permanent water, urban, forest and vegetation classes were produced using pre-processed pre-event Sentinel-2 data.

3.4. Feature Extraction and Analysis

The importance of using auxiliary features in order to improve the classification accuracy of primary remote sensing data has been emphasized in many studies conducted for different purposes [142, 143]. This concept is basically based on the assumption that information that can be produced based on the relations of the object or surface of interest to environmental factors such as topography, geology, climate, soil, water and moisture

can be included as descriptive features [144]. Many studies have demonstrated the potential of using such auxiliary features to investigate land surface changes caused by flood events [66, 132, 145-147]. In this thesis, NDVI, MNDWI and GLCM measurements were used as auxiliary features for improving the mapping accuracy. The methods are briefly explained in the following.

3.4.1. GLCM Features

The GLCM [71] is one of the commonly preferred for measuring of the second-order texture and based on the estimation of the probability density function, $P(i, j | d, \theta)$. GLCM measures the statistical spatial relation of c pixel co-occurrence in a pre-defined window and directions ($\theta = 0^\circ, 45^\circ, 90^\circ$ and 135°) and pixel distances (d) [37].

In this thesis, the GLCM measurements were applied to primary pre- & post-event Sentinel-1 (VV and VH) and Sentinel-2 mosaics for separating the flood and other land cover types. The GLCM measurements consist of the contrast, dissimilarity, homogeneity, angular second moment, maximum probability, energy, entropy, mean, variance and correlation, respectively. Textural measurements formulated in Equations 3.1-3.10 were applied to the Sentinel-1&2 datasets in all directions and with a 64-level probabilistic quantizer with a kernel size of (9 x 9), considering the computational requirements, although Amitrano et al. [70] and Senthilnath et al. [148] suggested the size of (7 x 7).

$$\text{Homogeneity} = \sum_{i,j=0}^{N-1} \frac{P_{i,j}}{1 + (i - j)^2} \quad (3.1)$$

$$\text{Contrast} = \sum_{i,j=0}^{N-1} P_{i,j} (i - j)^2 \quad (3.2)$$

$$\text{Dissimilarity} = \sum_{i,j=0}^{N-1} P_{i,j} |i - j| \quad (3.3)$$

$$\text{Angular Second Moment} = \sum_{i,j=0}^{N-1} \{\rho(i, j)\}^2 \quad (3.4)$$

$$\text{Energy} = \sqrt{ASM} \quad (3.5)$$

$$\text{Maximum Probability} = \max P_{i,j} \quad (3.6)$$

$$\text{Entropy} = \sum_{i,j=0}^{N-1} P_{i,j} (-\ln P_{i,j}) \quad (3.7)$$

$$\text{GLCM Mean } (\mu_i) = \sum_{i,j=0}^{N-1} i (P_{i,j}), \quad \mu_j = \sum_{i,j=0}^{N-1} j (P_{i,j}) \quad (3.8)$$

$$\text{GLCM Variance } (\sigma_{i,j}^2) = \sum_{i,j=0}^{N-1} P_{i,j} (i, j - \mu_{i,j})^2 \quad (3.9)$$

$$\text{GLCM Correlation} = \sum_{i,j=0}^{N-1} P_{i,j} \left[\frac{(i - \mu_i)(j - \mu_j)}{\sqrt{(\sigma_i^2)(\sigma_j^2)}} \right] \quad (3.10)$$

where, $P_{i,j}$ is the probability of values i and j occurring in adjacent pixels. i and j are the labels of the columns and rows (respectively) of the GLCM. μ and σ indicate the mean and standard deviation, respectively.

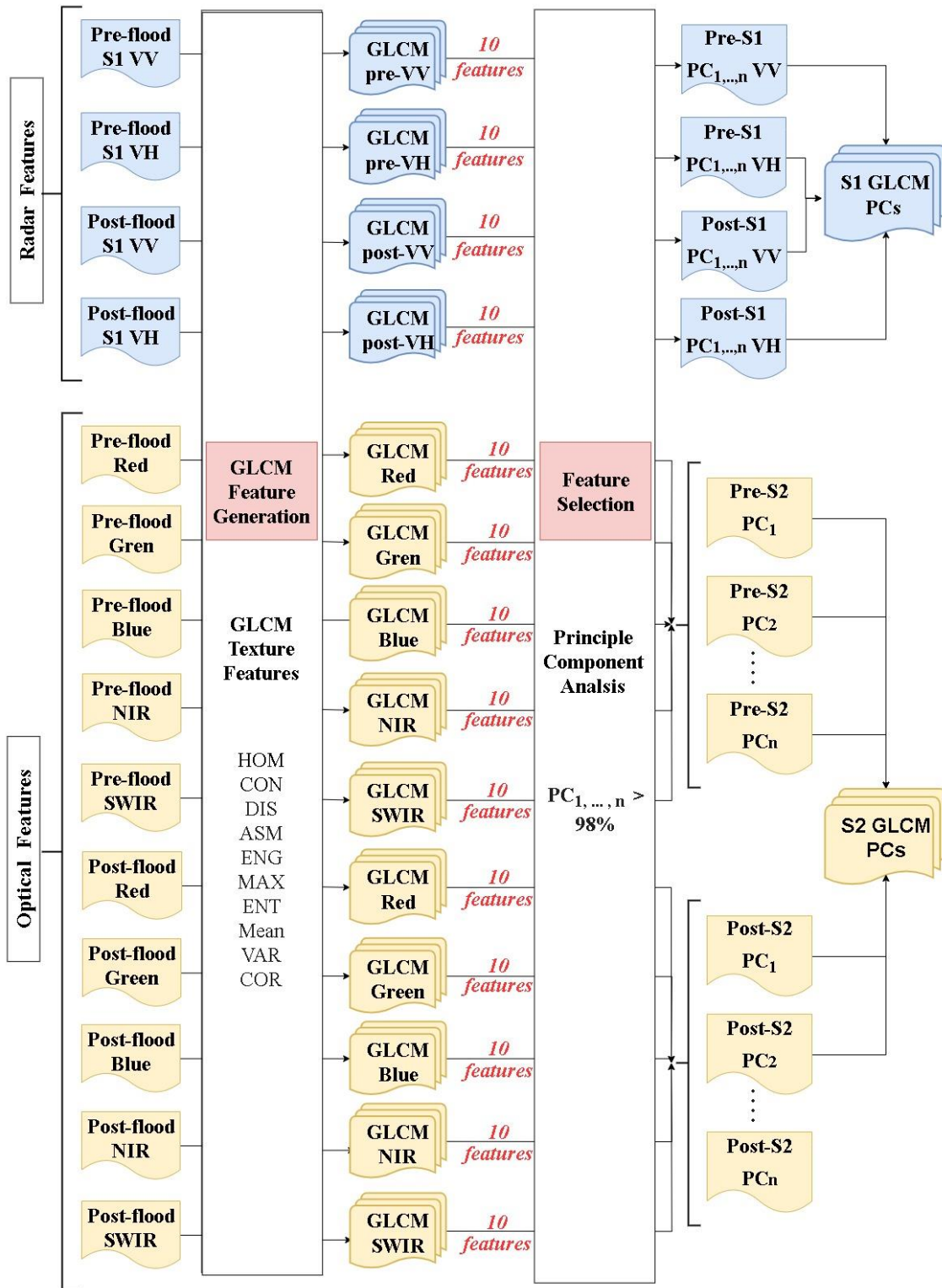


Figure 3.3. GLCM texture feature generation and selection.

3.4.2 Spectral Indices

The Sentinel-2 images provide valuable information about vegetation, urban, water and various other land cover classes. Spectral indices series such as NDVI [149], NDWI [150] (McFeeters, 1996), and many more are often preferred in the most common land monitoring applications. These indices provide information about the impacts of flood events on soil or ground even after the water has been absorbed [126, 151, 152]. The NDVI and MDNWI described in Equations (3.11-3.12) were obtained from the pre- & post-event Sentinel-2 data (Figure 3.4).

$$NDVI = (NIR - RED)/(NIR + RED) \quad (3.11)$$

$$MNDWI = (GREEN - SWIR)/(GREEN + SWIR) \quad (3.12)$$

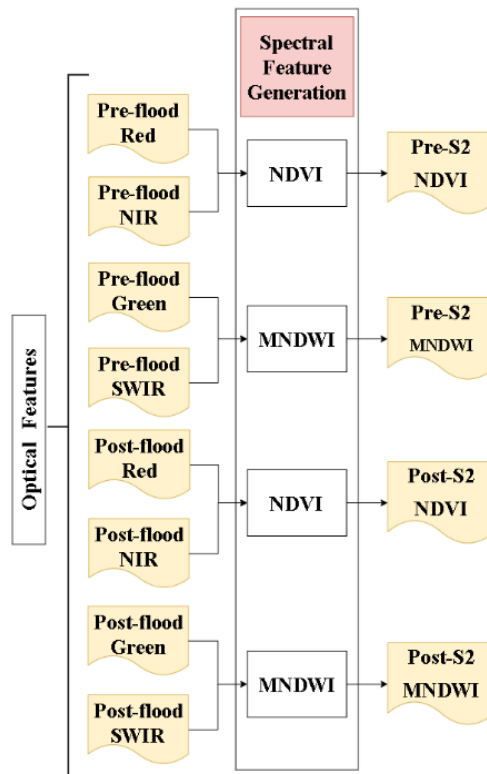


Figure 3.4. Spectral feature generation.

3.4.3. Principal Component Analysis

The PCA has been used in a number of flood mapping studies to improve visual interpretation or to generate input for the classification process [153]. In addition, as the coverage of dense multi-temporal and multi-source data increases, the potential for flood detection will increase even in areas with vertical targets such as dense vegetation and urban areas [154-158].

The purpose of PCA in this study is to optimize textural information and highlight uncorrelated information rather than preserving common information between auxiliary features. As shown in Figure 3.3, PCA have been applied to pre- & post-event Sentinel-1&2 GLCM features. As a result of the PCA, the principal components (PCs) that contain at least 98% information of the overall data have been used as auxiliary features together with the original Sentinel-1&2 bands.

3.4.4. Feature Selection

Considering the poor availability of Sentinel-2 data during or after a flood event due to clouds, various data availability scenarios for flood map production were investigated in detail in this thesis. Since post-event Sentinel-2 data suffered from clouds in Ordu, the investigations were carried out in Sardoba only. A number of feature stacks were created for this purpose as shown in Table 3.1 Stack 1 (Sentinel-1 only) and Stack 2 (Sentinel-2 only) were created in order to compare the performances of single sensor data for flood mapping. Accordingly, Stack 1 includes pre- & post-event flood S1 bands (VV and VH) and GLCM PCs, while Stack 2 includes pre- & post-event flood S2 bands (RGB, NIR,

SWIR), NDVI, MNDWI and GLCM PCs. On the other hand, Stack 3 was created for the analysis of scenarios where post-event S2 data cannot be used as input in classification. Therefore, Stack 3 was created for considering that pre-event Sentinel-2 data is usually available to contribute to Sentinel-1. Stack 4, on the other hand, represents a data group in which pre- & post-event S1 & S2 data are usable, which is generally not the case in flood events. Finally, Stack 5 was created for evaluating contributions of GLCM PCs in Stack 4 by removing them from this feature group.

Table 3.1. Data stacks and their components.

Features/Stacks		Stack 1	Stack 2	Stack 3	Stack 4	Stack 5	
Sentinel-2	Pre	Bands		✓	✓	✓	✓
		NDVI		✓	✓	✓	✓
		MNDWI		✓	✓	✓	✓
		GLCM PCs		✓	✓	✓	
	Post	Bands		✓		✓	✓
		NDVI		✓		✓	✓
		MNDWI		✓		✓	✓
		GLCM PCs		✓		✓	
Sentinel-1	Pre	Bands	✓		✓	✓	✓
		GLCM PCs	✓		✓	✓	
	Pos	Bands	✓		✓	✓	✓
		GLCM PCs	✓		✓	✓	

3.5. Random Forest Classification

Supervised and unsupervised ML approaches have been commonly used for flood inundation mapping with satellite imagery [62, 159]. Recently, the algorithms based on machine learning (SVM, decision tree (DT) and RF) and deep learning (deep NN, CNN and recurrent NN) have a high potential and great accuracy in many research activities [160, 161]. The ML including deep learning-based algorithms are frequently preferred

for accurate analysis of pre- & post-flood data, especially in flood inundation mapping studies [162].

The RF is a supervised ML approach that makes output (i.e. predictions) by combining results from decision trees (DT), $\{h(x, \theta_i), i = 1, \dots, T\}$, where x is the input vector and θ_i indicate the random vectors. This approach, proposed by Breiman [136], gives a vector (x) as input to each of the decision trees to classify and then final decision according to voting process assign to labels. In this way, RF can correctly classify dataset based on majority voting in each decision trees and process large datasets. The RF classification requires two model parameters defined by the user, the number of trees (T) and features (M). Although this study did not test the effect of the values assigned to these parameters, previous studies recommended that to obtain high accuracy, T can be set to 500 and M should be the square root of the number of features [163-165]. In this thesis, no parameter optimization was made for RF, but based on both literature review and heuristic analysis after manual investigation, the T parameter was used as 300. The ten-fold cross-validation results yielded mean OA and RMSE values of 92% and 0.23 based on random initializations for Stack 1 (Figure 3.5).

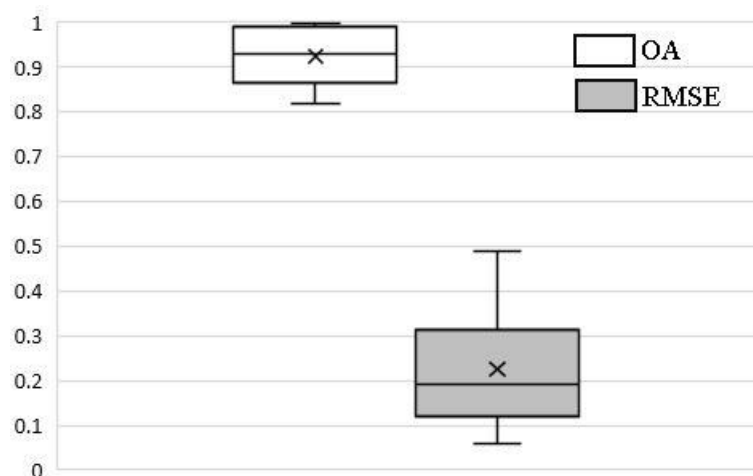


Figure 3.5. Boxplot of the 10-fold cross-validation results.

RF have been used in many remote sensing applications and compared other ensemble methods [166, 167]. Ham et al. [166] used RF for hyperspectral with a limited sample set and Gislason et al. [167] used RF for classification of multi-source data. Waske and van der Linden [168] used RF and SVM classifiers to classify multisensor imagery and stated

that RF performed better. In these studies, it has been noted that RF outperforms a single decision tree and is faster in terms of computation time compared to other ensemble methods [169, 170]. The selection of RF in this thesis was primarily due to its ability to outperform most classifiers, minimum parameter requirement, stability together with small sample sizes and few variables, and the high accuracy it consistently achieves in comparison to other classifiers, as demonstrated by Phiri et al. [171].

3.6. Validation

In this thesis, a set of measures calculated from the error matrix and given in Equations 3.13- 3.17 have been employed for assessing the results. The error matrices show the predicted and actual labels of the samples and the confusion between the classes together with true and false predictions. To analyze the error matrices, measures such as producer's accuracy (PA), user's accuracy (UA), overall accuracy (OA) [172] were used together with Kappa coefficient (K) [173].

$$\text{Omission error (PA)} = \frac{X_{ii}}{X_{+i}} \quad (3.13)$$

$$\text{Comission error (UA)} = \frac{X_{ii}}{X_{i+}} \quad (3.14)$$

$$\text{F1 score} = 2 \times \frac{(PA \times UA)}{(PA + UA)} \quad (3.15)$$

$$\text{OA} = \frac{\sum_{i=1}^r X_{ii}}{N} \quad (3.16)$$

$$K = \frac{N \sum_{i=1}^r X_{ii} - \sum_{i=1}^r (X_{i+} \times X_{+i})}{N^2 - \sum_{i=1}^r (X_{i+} \times X_{+i})} \quad (3.17)$$

where, r is number of rows; X_{ii} is the number of observations in i, i (row, column) ; X_{i+} and X_{+i} are total of observations in i, i (row, column), respectively. N is the total number of observations.

Even though the supervised classification approaches are able to successfully detect water bodies and flooded areas, ground truth is required for the training, classification and validation stages [174]. This requirement is often the greatest deficiency in flood mapping procedures. In this concept, train, test and validation data can often be obtained by using higher-quality data or by conducting field visits. Second operation is much more complex and often not feasible in cases including areas with high water dynamics or flood event cases.

To validate the classification results, the PlanetScope image mosaics were used as a reference data in Sardoba study area. Unfortunately, no such reference was available for Ordu floods. The PlanetScope satellite constellation, operated by Planet Labs Inc., acquire the images with a GSD of 3.7 meters [134]. The reference dataset was created through manual delineation using PlanetScope data obtained on May 10, 2020, through the Planet Explorer platform (www.planet.com). Figure 3.6 shows representative identified LULC classes on both the PlanetScope and post-event Sentinel-2 RGB data. The number of references (pixels) for Stack 1, Stack 2 & 4, and Stack 3 was 442,530, 546,052 and 450,680, respectively.

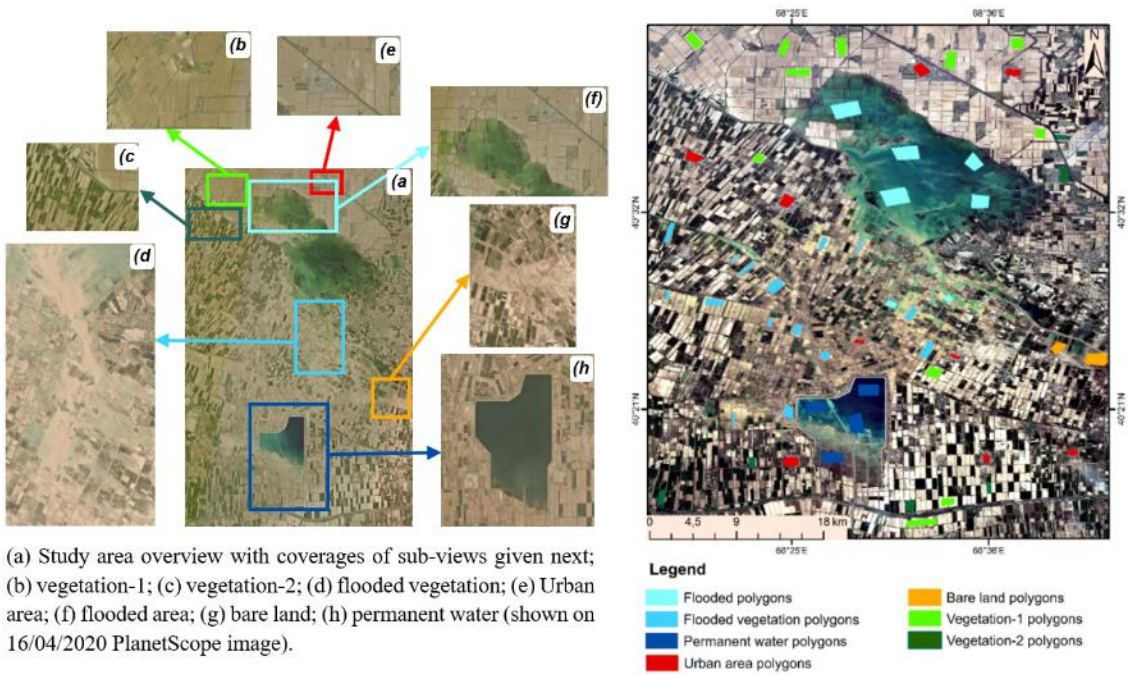


Figure 3.6. Examples from PlanetScope post-event (10/05/2020) image parts (left) and locations of training polygons depicted on post-event S2 RGB image (right) [128].

4. THE FLOOD EVENTS

The methodology proposed in the thesis is applied to two different flood events with different characteristics in terms of data availability, topographical and land cover conditions. In this section, the flood events, study area and data characteristics of the test areas are explained.

4.1. Sardoba Dam Failure

In this section, Sardoba study area and event and data characteristics are explained. The site was selected as it is a relatively flat region and the flooding was due to a dam failure.

4.1.1. Sardoba Study Area and Event Characteristics

The construction of the Sardoba Dam was completed between 2010 and 2017 on the Syr Darya River, one of Uzbekistan's two major rivers [175]. The dam reservoir holds particular importance, primarily concerning the country's irrigation and energy needs. With a capacity of approximately 922 million m³, it efficiently provides water for irrigating agricultural lands in the Sirdaryo and Jizzakh regions [176]. The agricultural products cultivated in the region are 80% cotton, 15% melon-watermelon, 4% corn and 1% alfalfa (Maktaaral.gov.kz, 2020). The dam, which provides water for irrigation of croplands in Sirdaryo and Jizzakh regions, has a capacity of approximately 922 million m³ [176]. Heavy rains in some parts of Uzbekistan on April 27-29, 2020, caused partial collapse of the Sardoba dam in the province of Sirdarya. On May 1, 2020, the region was flooded due to a failure on the wall of the dam. A dam failure on May 1, 2020, led to extensive flooding in the region, with floodwaters encroaching into Kazakhstan's borders, resulting in significant damage across more than 20 small settlements and fertile agricultural lands. [175]. The flooding especially affected the Sardoba and Jizzack

districts of Uzbekistan and Maktaaral district of Kazakhstan province and caused great damage to the economy of the region.

The study site location covering an area of approximately 2430 km² and the corresponding land cover (LC) and elevation maps are shown in Figure 4.1. According to the WorldCover 2021-v2 product provided by ESA, the study area mainly consists of 73% cropland [177]. This is followed by 14% grassland, 6% built-up area, 4% bare/sparse vegetation, and 3% permanent water bodies, respectively. As shown in Figure 4.1.(b), there are many villages consisting of houses with three or less floors around the dam built for irrigation of croplands in the region. In Figure 4.1.(c), according to the Global 30 Arc-Second Elevation (GTOPO30) elevation values in the study area have a smooth decreasing change from south to north between 260-360 m [178]. In this way, the SAR data used in the study are not affected by the distortions caused by the the image acquisition geometry.

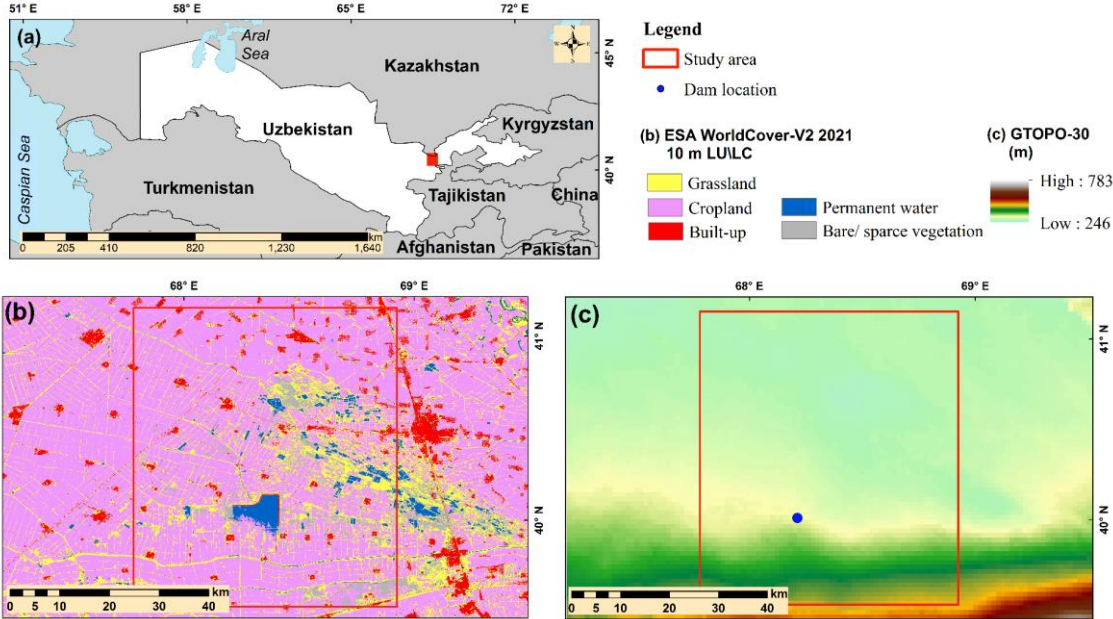


Figure 4.1. The study area location (a), the LULC map obtained from the WorldCover 2021-v2 (b) and DEM from GTOPO-30 (c) .

4.1.2. Sardoba Data Characteristics

In Sardoba site, S1 GRD and S2 MSI L2A datasets are provided by the ESA Copernicus Programme. Also, PlanetScope data representing the flood conditions have been used as an external reference source for the validation of the results. Table 4.1 summarizes the data acquisition dates (dd.mm.yyyy), the surface state (pre- or post-event), flight direction and orbit number together with dataset ID such as DS1. The Sentinel-2 data were 14.04.2020 (pre-event) and 04.05.2020 (post-event). Likewise, the pre-event Sentinel-1A is 29.04.2020, while the post-event Sentinel-1A data is 05.05.2020. Overviews of the pre- & post-event satellite images from S2 in true color combination and the VV and VH polarization data of S1 are given in Figure 4.2.

Table 4.1. Basic specifications of the datasets used in the Sardoba study area.

	ID	Acquisition Date	Condition	Flight Direction/Orbit Number
Sentinel-1	DS1	29.04.2020	Pre-event	ASC/71
	DS2 DS3	05.05.2020	Post-event	DSC/151
Sentinel-2	DS4	24.04.2020	Pre-event	DSC/34
	DS5	04.05.2020	Post-event	
PlanetScope orthoimage		10.05.2020	Post-event	
DS1: S1A_IW_GRDH_1SDV_20200429T132316_20200429T132341_032343_03BE56_0401 DS2: S1A_IW_GRDH_1SDV_20200505T013021_20200505T013046_032423_03C11E_EDA3 DS3: S1A_IW_GRDH_1SDV_20200505T012956_20200505T013021_032423_03C11E_7886 DS4: S2B_MSIL2A_20200424T061629_N0214_R034_T42TVK_20200424T095418 DS5: S2B_MSIL2A_20200504T061629_N0214_R034_T42TVK_20200504T095816				

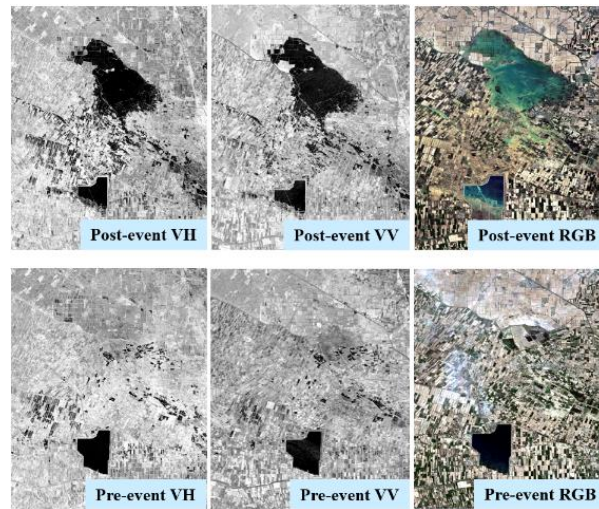


Figure 4.2. Pre- & post-event satellite images of the study site obtained from Sentinel-2 in true color combination and the VV and VH polarization data of Sentinel-1.

4.2. Ordu 2018 Flood

In this section, Ordu study area and event and data characteristics have been explained. The site was selected as floods occur frequently in the region, which has rugged topography and dense vegetation.

4.2.1. Ordu 2018 Study Area and Event Characteristics

The study areas investigated here are the flood disasters that occurred in some districts of Ordu and Samsun provinces located in the Black Sea Region, in the north of Türkiye. Unye, Ikizce and Caybası districts in Ordu Province and Terme and Carsamba districts in Samsun Province were the most affected by the disaster. The study area has a Black Sea climate and there is precipitation in almost all months of the year. Based on analysis between 1950 and 2011, landslides (80%) constitute the most prevalent natural hazard in the area, followed by floods (9%) and rockfall (8%) [179].

On August 8, 2018 in the late afternoon, flooding occurred in the area and damaged houses, agricultural areas, and infrastructure. In the area, about 80 mm of precipitation

fell per square meter and caused flooding of streams and rivers. There have been numerous landslides triggered by flooding and a total of 8 bridges were destroyed, including the Cevizdere Bridge in Unye Town (TRT News, 2018). Further details about the event can be found in Tavus et al. [135] and Kocaman et al. [179].

The study area covers an area of approximately 1985 km² and the corresponding LULC and elevation maps are given in Figure 4.3. According to the WorldCover 2021-v2 product provided by ESA, the study area mainly consists of 82% trees classes. This is followed by 7% cropland, 6% grassland, 3% permanent water bodies, 1% built-up area and 1% herbaceous wetland, respectively (Figure 4.3 (b)). The climate and precipitation yields the area to be suitable for agriculture. Especially in Ordu province, there are hazelnut trees on the hill slopes. The other agricultural products of the region are corn, potatoes, beans, soy, wheat and barley, but some citrus fruits and tea are also cultivated. The elevation values of the study area, which consists of approximately 85% hilly regions, vary between 1 m and 1200 m (Figure 4.3 (c)). In the centre of the districts which shown with towns in the Figure 4.3 (c), mean elevation value are nearly 25 m, 10 m, 12 m, 140 m and 500m for Carşamba, Terme, Unye, İkizce and Caybaşı regions, respectively.

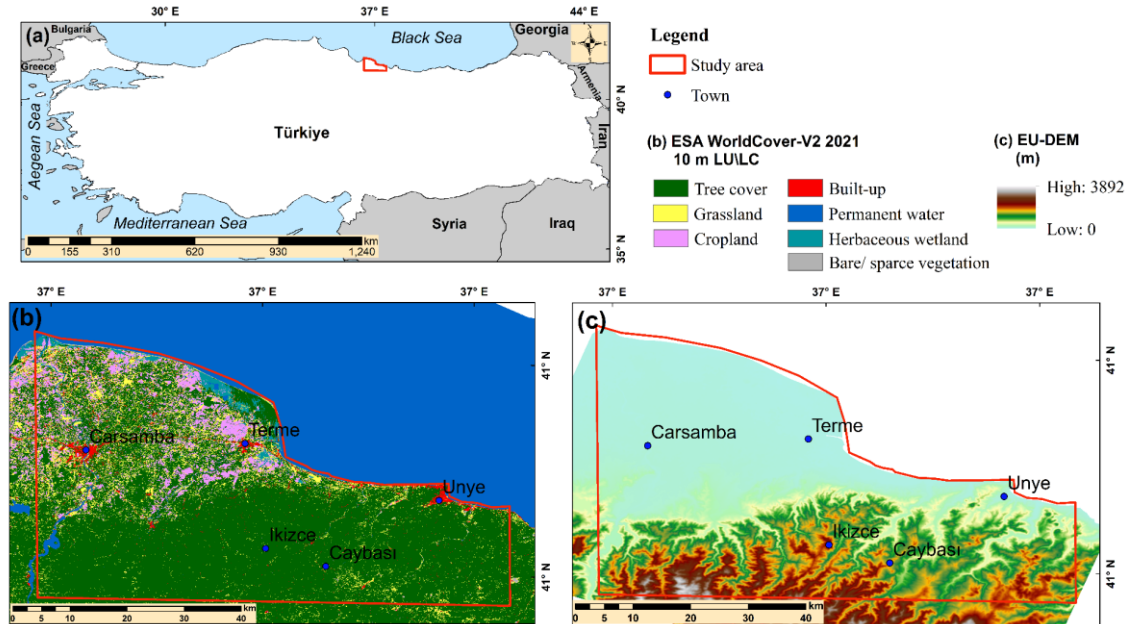


Figure 4.3. The study area location (a), the LULC map obtained from the WorldCover 2021-v2 (b) and DEM from EU-DEM (c).

4.2.2. Ordu Data Characteristics

In this study area, Sentinel-1 GRD and Sentinel-2 MSI L2A datasets were available. Table 4.2 summarizes the data acquisition dates (dd.mm.yyyy), the ground conditions at the time of the data acquisition (pre- or post-event), flight direction and orbit number together with data-sets ID such as DS1. The selected Sentinel-1 and Sentinel-2 data accurately represented the pre- & post-flood conditions in terms of time and resolution. The Sentinel-2 data were 16.05.2018 (pre-event) and 09.08.2018 (post-event). Likewise, the pre-event Sentinel-1A is 18.08.2018, while the post-event Sentinel-1A data is 10.08.2018. Overviews of the pre- & post-event satellite images of the some part of the Carsamba town obtained from Sentinel-2 in true color combination and the VV and VH polarization data of Sentinel-1 are given in Figure 4.4.

Table 4.2. Basic specifications of the datasets used in the Ordu study area.

	ID	Acquisition Date	Condition	Flight Direction/Orbit Number
Sentinel-1	DS1 DS2	18/05/2018	Pre-event	DSC/94
	DS3 DS4	10/08/2018	Post-event	
Sentinel-2	DS5	16/05/2018	Pre-event	DSC/121
	DS6 DS7	09/08/2018	Post-event	
DS1: S1B_IW_GRDH_1SDV_20180518T034024_20180518T034049_010970_014159_08A7 DS2: S1B_IW_GRDH_1SDV_20180518T034049_20180518T034114_010970_014159_B477 DS3: S1B_IW_GRDH_1SDV_20180810T034029_20180810T034054_012195_016770_7612 DS4: S1B_IW_GRDH_1SDV_20180810T034054_20180810T034119_012195_016770_841C DS5: S2A_MSIL2A_20180516T081611_N0207_R121_T37TCF_20180516T102815 DS6: S2B_MSIL2A_20180809T081559_N0208_R121_T37TCF_20180809T112729 DS7: S2B_MSIL2A_20180809T081559_N0208_R121_T37TCF_20180809T132329				

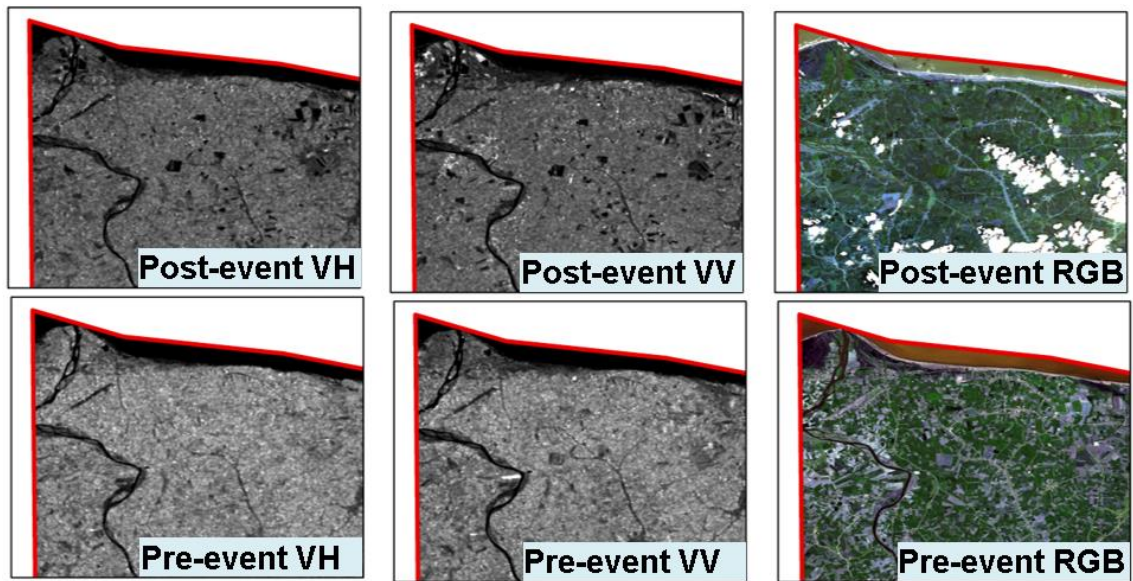


Figure 4.4. A part of pre- & post-event Sentinel-2 images of the study site and the VV and VH polarization data of Sentinel-1.

5. RESULTS

In this chapter, the quantitative and qualitative results of two flood events occurred in two different regions, one with rugged topography (Ordu site) and the other one in plains (Sardoba Site), are presented.

5.1. Results from Sardoba Dam Failure

This section presents the flood mapping results for the Sardoba dam failure occurred on May 1st, 2020 in detail. The feature maps produced for Sardoba are given in the next sub-heading. Section 5.1.2 presents the flood maps obtained with different feature sets and the validation results in terms of confusion matrices between the identified classes, overall accuracy, user's and producer's accuracy, the Kappa value, and the F-1 score.

5.1.1 Feature Maps Produced for Sardoba Site (GLCM, Indices and PCA)

Texture measurements explained in Chapter 3.4.1 have been applied to the pre- & post-event S1 and S2 data. As a result of applying ten GLCM measurements to pre- & post-event VV and VH bands of Sentinel-1 data, a total of 40 textural features were produced. Table 5.1 presents overviews of selected textural features obtained from pre- & post-event Sentinel-1 VV and VH data. Additionally, pixel value ranges ranging from white to black are given for the homogeneity, entropy and correlation features that can best be interpreted visually. The PCA was applied individually to the pre- & post-event VV and VH datasets, each containing 10 textural features. Table 5.2 presents overviews of PCs together with their information percentages. With PCA, PC1 (99%) from the pre-event VV dataset, PC1 and PC2 (87% and 13%) from the pre-event VH, PC1 (98%) from the post-event VV, and PC1 and PC2 from the post-event VH data were computed (Table 5.2).

Table 5.1. Overviews of selected textural features produced from S1 for Sardoba.

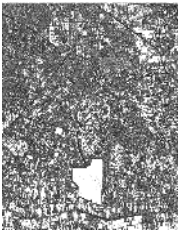



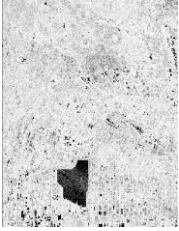

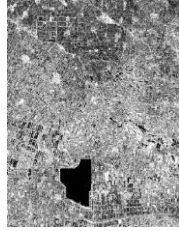
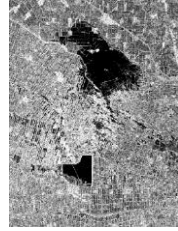
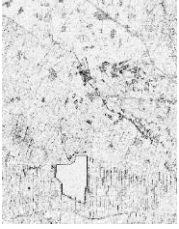

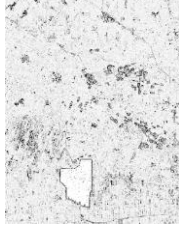
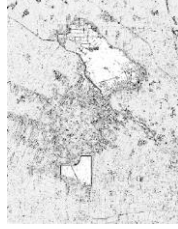
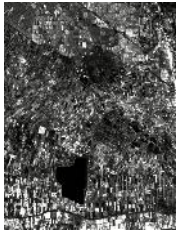
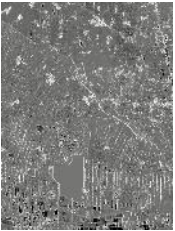
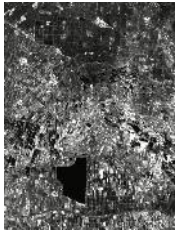

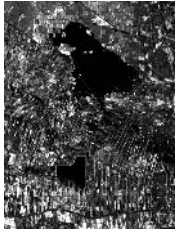
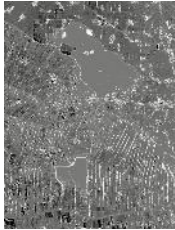


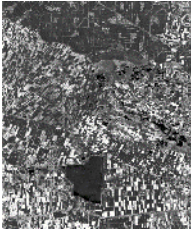
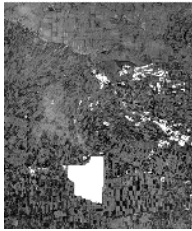
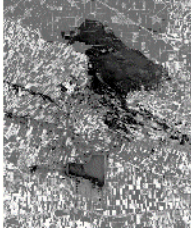
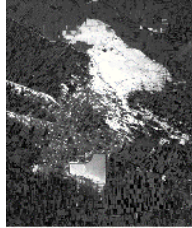
Inputs	Sentinel-1 VV		Sentinel-1 VH	
	Pre-event	Post-event	Pre-event	Post-event
Homogeneity (0.00 - 1.0)				
Entropy (0.00 - 9.5)				
Correlation (0.00 - 1.0)				

Table 5.2. Overviews of GLCM PCs derived from the S1 and their information percentages for Sardoba.

Inputs	Sentinel-1 VV		Sentinel-1 VH	
	PC ₁	PC ₂	PC ₁	PC ₂
Pre-event	 99%	 1%	 87%	 13%
Post-event	 98%	 2%	 91%	 9%

For the feature extraction of Sentinel-2 dataset, GLCM features and spectral indices that include NDVI and MNDWI have been produced. Table 5.3 represent the NDVI and MNDWI produced from pre- & post-event Sentinel-2 data. In the NDVI images, flooded areas can be recognized well. The MNDWI results help to separate permanent waters and flooded areas.

Table 5.3. Overviews of spectral indices produced from S2 datasets for Sardoba.


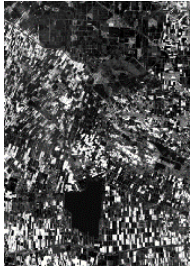
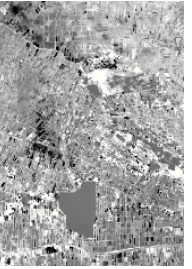

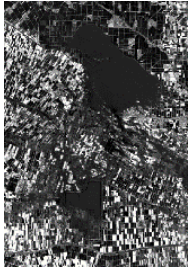
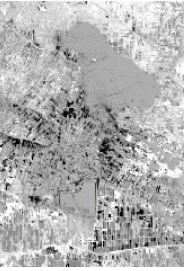
Inputs	Sentinel-2	
	NDVI	MNDWI
Pre-event (-1.00 – 1.00)		
Post-event (-1.00 – 1.00)		

The texture measurements have been applied also to the to pre- & post-event red (B2), green (B3), blue (B4), NIR (B8) and SWIR (B11) of Sentinel-2 data. Thus, a total of 100 GLCM features have been produced. Table 5.4 shows the overviews of selected textural features applied to the pre- & post-event B2, B3, B4, B8 and B11 data of Sentinel-2. In addition, homogeneity, entropy and correlation features are given, with pixel values ranging from white to black (0.00 - 1.00), (-0.00 - 9.5) and (0.00 - 1.0), respectively. Likewise, for the S1 dataset, PCA was applied separately to pre- & post-event VV and VH bands, each containing 10 texture features. According to PCA, the pre-event S2 dataset yielded PC1, PC2, and PC3 accounting for 57%, 37%, and 6% of the information, respectively, while the post-event S2 dataset generated PC1, PC2, and PC3 components accounting for 70%, 24%, and 6% of the information (Table 5.5).

Table 5.4. Overviews of the textural features produced from S2 over Sardoba.

Inputs	Sentinel-2					
	Red (B2)	Green (B3)	Blue (B4)	NIR (B8)	SWIR (B11)	
Homogeneity (0.00 - 1.00)	Pre-event					
	Post-event					
Entropy (0.00 - 9.5)	Pre-event					
	Post-event					
Correlation (0.00 - 1.0)	Pre-event					
	Post-event					

Table 5.5. Overviews the GLCM PCs derived from S2 and their information percentages over Sardoba.

Inputs	Sentinel-2		
	PC ₁	PC ₂	PC ₃
Pre-event	 57%	 37%	 6%
Post-event	 70%	 24%	 6%

5.1.2. Flood Maps and Validation Results

The flood maps produced from Stack 1- 4 are presented in Figure 5.1. (a)- (d). The Stack 1 and Stack 2 were created to analyse the performances of single sensor data for flood mapping. While Stack 3 refers to the situation where post-event S2 data cannot be used, it includes pre-event S2, pre-&post event S1 and their respective feature maps. Stack 4 consists of both pre- & post-event S1 and S2 data and their features. In addition, Stack 5 was produced, the details of which are explained later and the classification result is given in Figure 5.2, in order to analyze the contribution of GLCM feature components to the prediction performance. As shown in Figure 5.1 (a), when only S1 data are used, five LULC classes (FL, PW, V1, V2, Ur) could be defined, while the availability of the pre- & post-event S2 data allows for the definition of further LULC classes (additionally FV and BL. Additionally, Stack 3 allows for the definition of six distinct LULC classes, whereas Stack 4 enables the definition of seven classes (Figure 5.1 (c)). In the event that post-event S2 data is not available (Stack 3), except for the FV class, the other six classes were determined (Figure 5.1(c)).

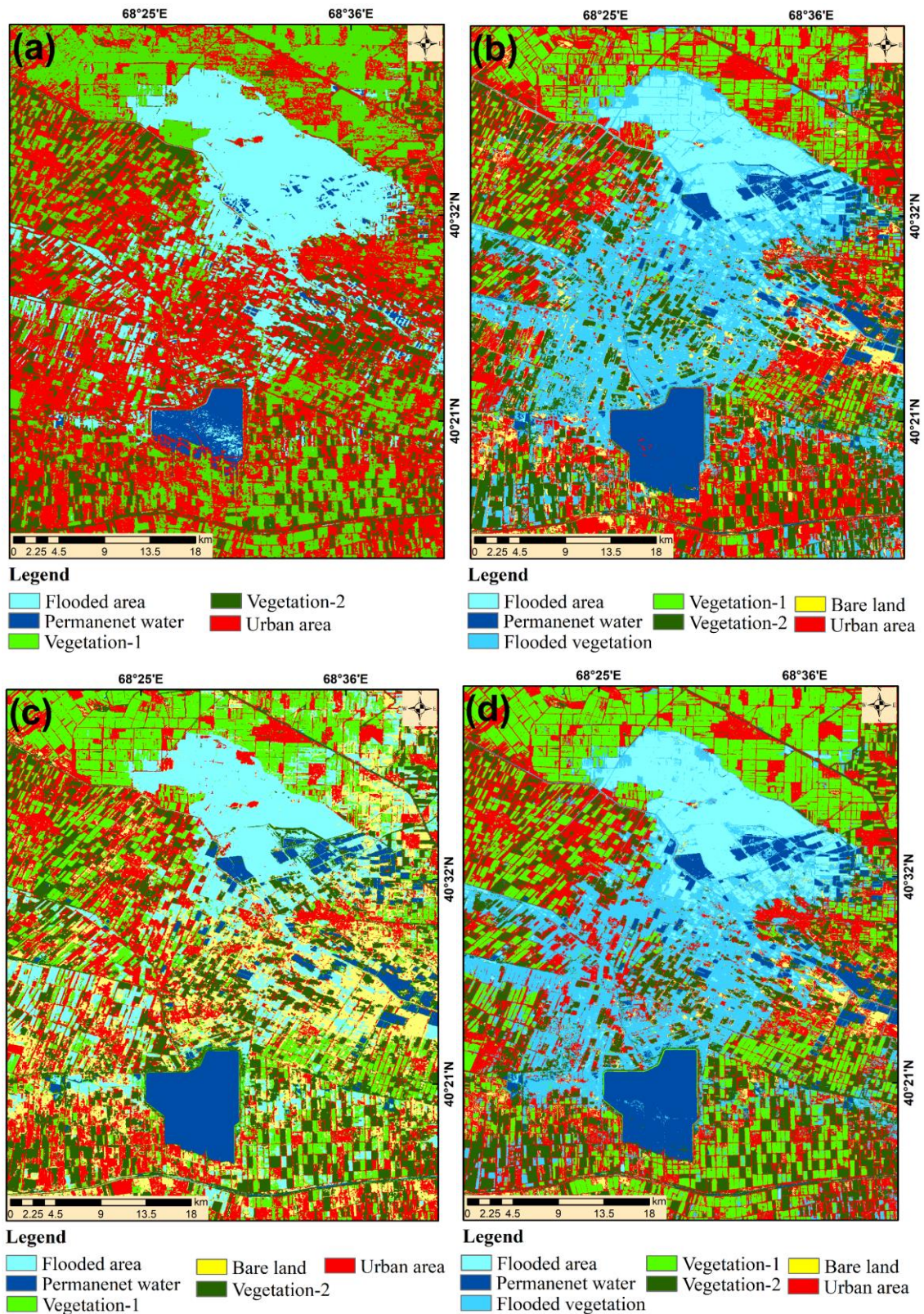


Figure 5.1. The RF classification results for; (a) Stack 1 (S1 only), (b) Stack 2 (S2 only), (c) Stack 3 (S1 and pre-event S2) and (d) Stack 4 (S1 and S2).

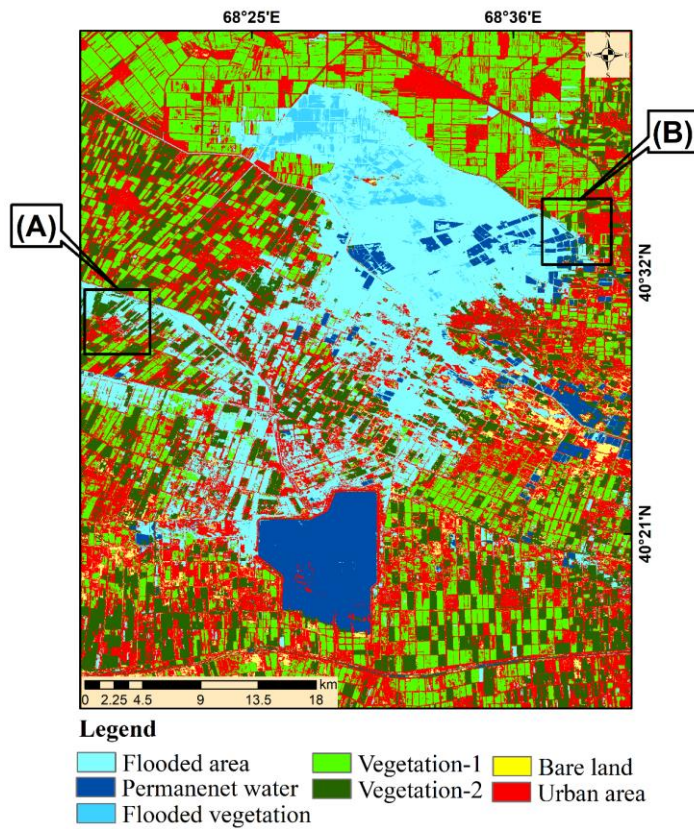


Figure 5.2. The RF classification result for Stack 5 (without GLCM PCs).

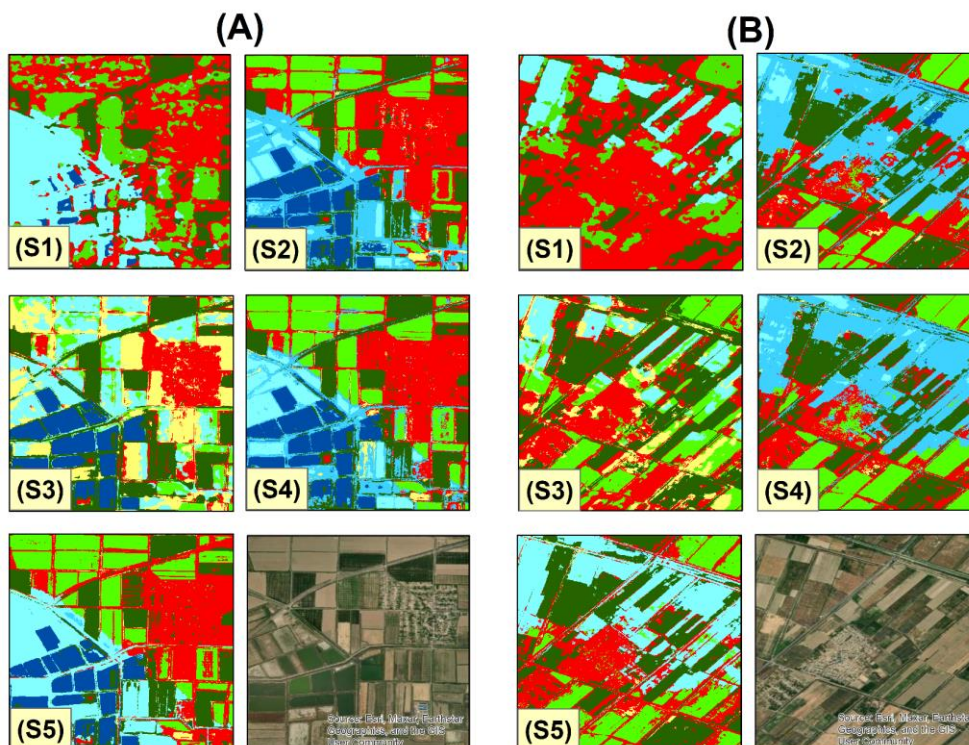


Figure 5.3. Zoomed-in views of Stack 1-5 classification results for sub-areas A and B, denoted by the black rectangles in Figure 5.2.

For analyzing contributions of the GLCM PCs to the prediction performance, they were removed from Stack 4 and thus Stack 5 was obtained. Figure 5.2 shows the classification result produced from Stack 5, which consists of pre- & post-event S1 and S2 bands (B2, B3, B4, B8, B11), NDVI and MNDWI. In addition, for detailed visual analysis, views of Stack 1-5 classification results for sub-areas A and B, denoted by the black rectangles in Figure 5.2 are given in Figure 5.3. The flood maps produced from Stack 4 and Stack 5 exhibit differences in specifically the FV class based on the visual inspection. Here, omission of the GLCM features caused FV pixels to be generally labeled as FL, but also confused with the Ur and V2 classes. In other words, in the absence of texture information, the FV class could not be learned and classified by the model and the relevant FV pixels were usually assigned to the classes they belonged to the pre-flood conditions. Consequently, although distinctions were noted in the FL, Ur, and V1 classes, no substantial change was evident in the PW and V2 classes. On the other hand, the use of GLCM data, especially for the Ur class, largely eliminated the noisy-pattern found as a result of not using it.

The classification results given in Figure 5.1 include the above-mentioned different LULC classes, as well as many differences when compared visually. As can be seen in Figure 5.1 (a), Stack 1, which consists of only S1 and its features, could not determine the FV and BL classes, and the classes showed a noisy pattern. Especially pixels belonging to F1, V1 and V2 classes are labeled as Ur class. In addition, in this scenario where S2 data is not used, the PW class within the dam could not be determined to represent the post-flood situation, unlike other classification results. As a result of the classification of S1, pre-event S2 and Stack 3, which is given in Figure 5.1 (c), the FV class could not be determined and some agricultural parcels located in the flood area were incorrectly labeled as PW. In addition, confusion was observed between BL and V1 classes. On the other hand, the misclassification in the Ur class found as a result of Stack 1 has been greatly reduced here. In addition, unlike other classification results, misclassified PW pixels in the north and north east of the study area were not seen in this scenario.

According to the Stack 2 classification result given in Figure 5.1 (b), it was observed that the mixing between the Ur and FL classes found as a result of the Stack 1 classification result was greatly reduced. However, according to the Stack 1 classification result, it was

seen that the confusion between Ur and V1, V2 classes continues to decrease. On the other hand, it was observed that V1 and V2 classes could be determined better. As a result of Stack 3 (S1 and pre-event S2) classification result, the problem of misclassification of the BL class is eliminated in this scenario (Stack 2), where only optical data is used. According to the Stack 4 classification result given in Figure 5.1 (d), BL, Fl, FV, V1 classes are best classified according to other results. The problems mentioned above for the Ur class have been greatly reduced in this dataset and as a result of Stack 3, where the Ur class has the highest F1-score, the a noisy pattern seen for this class has decreased.

Table 5.6 represents confusion (error) matrix elements for Permanent Water (PW), Flooded Area (Fl), Flooded Vegetation (FV), Urban (Ur), Bare Land (BL), Vegetation-1 (V1), and Vegetation-2 (V2) classes together with PA and UA and F-1 score values. In addition, the OA and K values for each classification result available in the tables, while the rows represent the numbers of actual (PlanetScope), while the columns correspond to the predicted class samples. The values were acquired by comparing them with the reference dataset established in PlanetScope image mosaics. The reference dataset for classes except that the PW class was created by manually delineating using PlanetScope data obtained on May 10, 2020 via the Planet Explorer platform. The reference dataset for the PW class, on the other hand, was manually delineated from PlanetScope data obtained on April 16, 2020, representing non-flooding conditions. As a result of this, the number of reference samples (pixels) for Stack 1, Stack 2, 4 & 5, and Stack 3 was 442,530, 546,052 and 450,680, respectively. Also, detailed information about the reference data generation is given in section 3.6.

Table 5.6 includes the confusion matrix produced from classification of Stack 1, which includes only pre- & post-event S1 data and derived features. According to confusion matrix produced from Stack 1, OA and Kappa values were 71% and 0.62. The F1-score for the Fl, PW, Ur, V1 and V2 classes were 0.89, 0.72, 0.41, 0.73, 0.56, respectively. Despite the high UA (90%) and PA (88%) values observed in the flooded area, there exists significant confusion between the flooded areas and the permanent water classes. The PW class is also confused with the urban and vegetation 1 classes. Additionally, the PA of urban areas was very low (27%) compared to the UA (88%), indicating that this class was overestimated in this dataset. While the PA values are strong performance for the vegetation classes, the UA values demonstrate lower accuracy. Even though Sentinel-

1 is not affected by cloud cover and is suitable for use in flood-triggering weather conditions, it was unable to distinguish inundated vegetation and bare lands when used as the sole sensor. Difficulty in visual interpretation of existing LULC classes found in Sentinel-1 data brings with it the need for additional information about the plots.

According to the confusion matrix produced from Stack 2, the OA and Kappa values, which were superior than the results of Stack 1, were 79% and 0.75 (Table 5.6). The F1-score for the BL, Fl, FV, PW, Ur, V1 and V2 classes were 0.63, 0.75, 0.83, 0.88, 0.61, 0.87 and 0.86, respectively. In addition to the higher performance result, the use of post-event Sentinel-2 data enabled the determination of BL and FV classes. Besides, the F1-score of the vegetation 2 (V2) obtain the highest values in Stack 2. In this dataset, FV was predicted with 94% PA, while flooded areas (FL) had a lower PA (69%) compared to Stack 1 (88%). The PA values of the Fl (69%) and FV (94%) classes indicate that the optical data has the capability to separate the flooded vegetation areas. When the F1-scores of the classes were compared, although there was a decrease in the FL class, a high increase was observed in the other classes.

In the Stack 3 (pre- & post-event S1 and pre-event S2 data), six LULC classes could be defined as FV was not visible in the post-event S1 data. According to the confusion matrix produced from Stack 3, the OA and Kappa values, which were superior than the results of Stack 1 and 2, were 82% and 0.76 (Table 5.6). The F1-score values for the BL, Fl, PW, Ur, V1 and V2 classes were 0.32, 0.81, 0.90, 0.88, 0.86 and 0.78, respectively. According to the F1-scores produced from Stack 2 (only Sentinel-2 data), the F1 values of the Fl, PW and Ur classes have increased, and the F1 values of the BL and V2 classes have decreased. No change was observed for the V1 class. In addition, the F1-score of the PW and Ur obtain the highest values in Stack 3. The PA of PW is 81% because it is mostly confused with the FL class. Hence, it is advisable to use pre-event Sentinel-2 data together with the Sentinel-1 data to precise identification of the non-flood classes. In this scenario, the F1 score of the BL class with the lowest classification accuracy is 0.32 as it is often confused with the V1 and FL class. Conversely, while the Sentinel-2 could visually identify the bare land class, it proved challenging to classify accurately. Further improvements may be required to improve the prediction of this class.

Table 5.6. Confusion matrix produced from the classification of Stack 1 - 5, along with the accuracy metrics.

		Bare Land	Flood	Flooded Vegetation	Perm. Water	Urban	Vegetation-1	Vegetation-2	UA (%)
Stack 1	Bare Land	NA	NA	NA	NA	NA	NA	NA	
	Flood	NA	108171	NA	10007	936	11	779	90
	Flooded Veg.	NA	9512	NA	NA	NA	NA	NA	
	Perm. Water	NA	167	NA	48244	15304	2490	222	64
	Urban	NA	4376	NA	0	32400	4153	276	88
	Vegetation-1	NA	393	NA	0	52085	103645	1881	64
	Vegetation-2	NA	108171	NA	0	20676	6794	20008	42
	PA (%)		88		83	27	86	86	
	F1-score		0.89		0.72	0.41	0.73	0.56	
	Overall Accuracy: 68% Kappa (K): 0.60								
Stack 2	Bare Land	15587	8976	53	0	689	0	2	62
	Flood	659	78347	6734	46	8056	1034	242	82
	Flooded Veg.	8	12410	104535	21072	0	0	16	75
	Perm. Water	0	0	0	75878	0	0	0	100
	Urban	7730	11702	95	83	45916	680	2542	67
	Vegetation-1	499	3043	0	0	23743	90602	2	78
	Vegetation-2	7	0	0	0	4100	0	20964	84
	PA (%)	64	69	94	78	56	98	88	
	F1-score	0.63	0.75	0.83	0.88	0.61	0.87	0.86	
	Overall Accuracy: 79% Kappa (K): 0.75								
Stack 3	Bare Land	8532	16489	NA	0	10	185	4	38
	Flood	1946	11086	NA	17969	949	265	5963	81
	Flooded Veg.	NA	NA	NA	NA	NA	NA	NA	
	Perm. Water	0	0	NA	75767	0	0	0	100
	Urban	3913	673	NA	85	60350	2683	1185	88
	Vegetation-1	9215	9392	NA	2	8474	90476	268	77
	Vegetation-2	4122	0	NA	0	229	0	20674	83
	PA (%)	31	81		81	86	97	74	
	F1-score	0.32	0.81		0.90	0.88	0.86	0.78	
Overall Accuracy: 82% Kappa (K): 0.76									

		Bare Land	Flood	Flooded Vegetation	Perm. Water	Urban	Vegetation-1	Vegetation-2	UA (%)
Stack 4	Bare Land	11131	2916	1478	0	6497	623	2662	44
	Flood	502	88754	2325	58	846	2300	333	93
	Flooded Veg.	386	10053	107663	19808	2	0	129	78
	Perm. Water	0	0	0	75841	0	0	37	100
	Urban	802	8045	27	91	53554	4722	1507	78
	Vegetation-1	239	1902	0	0	4617	111129	2	94
	Vegetation-2	29	0	0	0	4217	0	20825	83
	PA (%)	85	79	96	79	77	94	82	
	F1-score	0.58	0.85	0.86	0.88	0.77	0.94	0.82	
Overall Accuracy: 86% Kappa (K): 0.83									
Stack 5	Bare Land	10048	2965	0	0	12157	123	14	40
	Flood	157	78404	1	2	8525	7378	651	82
	Flooded Veg.	2	101018	23238	13591	152	0	40	17
	Perm. Water	0	92	0	75611	175	0	0	99
	Urban	403	2701	0	73	61186	1429	2956	89
	Vegetation-1	63	395	0	0	15934	101467	30	86
	Vegetation-2	13	0	0	0	4196	0	20862	83
	PA (%)	94	42	99	85	60	92	85	
	F1-score	0.56	0.29	0.56	0.91	0.71	0.88	0.84	
Overall Accuracy: 68% Kappa (K): 0.60									

The confusion matrix in Table 5.6, generated from the classification of Stack 4 which represents a scenario where all data is available, resulted in an OA of 86% and a Kappa value of 0.83. These values indicate a slightly superior performance for this stack compared to the results obtained from Stack 3. Here, since post-event Sentinel-2 data is available, just like in Stack 2, a total of seven classes were defined. The F1-score for the BL, Fl, FV, PW, Ur, V1 and V2 classes were 0.58, 0.85, 0.86, 0.88, 0.77, 0.94 and 0.82 respectively. Here, according to the comparison of the results produced from Stacks 1, 2, and 3, it becomes evident that the overall results are improved. In addition, the F1-score of the BL, Fl, FV, V1 obtain the highest values in Stack 4.

According to the confusion matrix produced from the Stack 4 and 5, 86% OA and 83% K values in Stack 4 reduce to 68% OA and 60% K values in Stack 5, respectively (Table 5.6). The F1-score for the BL, FL, FV, PW, Ur, V1 and V2 classes were 0.56, 0.29, 0.56, 0.91, 0.71, 0.88 and 0.84 respectively. As evident from both the classification results and the error matrices, the use of GLCM data yields a significantly improvement in classification accuracy, effectively decreasing the confusing between FV and FL classes. In cases where GLCM is not used, over 75% of FV class pixels were misclassified as FL, whereas no such confusion between FV and other classes. To elaborate, the absence of textural features led to the labeling of flood regions as urban and vegetated areas. It is clear that the radar data exhibits a different backscatter characteristic for inundated vegetation when contrasted with other classes. This finding highlights the difference in texture characteristics of the flooded vegetation, especially compared to the flood, water or other cropland in the region.

Using GLCM Principal Components (PCs) has notably elevated the PA of urban areas from 60% to 77%. However, there was a decrease in UA from 89% to 78%, because Ur class pixels were labeled as FL. Hence, it can be asserted that the textural information causes complexity in the process of learning of Ur and FL classes. Furthermore, comparing both sets of results revealed that the PA of the PW class, classified using GLCM, has increased from 79% to 85%. In Stack-1 and Stack-2, the PA values for the the PW class were at 79% and 85%, respectively. This outcome suggests that textural information might contribute to the mixing between PW and FL classes.

Feature importance (FI) was applied to analyze the effectiveness of S1 (VV and VH) and S2 (blue-B, green-G, red-R, NIR and SWIR) bands on the prediction performance. While calculating the feature importance score, each feature was perturbed 3 times and the average of the percentage of correct predictions was taken. The importance score given in Table 5.7 is the original % of correct prediction. According to FI scores of pre- & post-event S2 bands, the most effective band is post-event SWIR, followed by post-event B2, B11 and B4. In addition, power set evaluation indicated that % 99.8 OA can be obtained from S2 bands including post-event B11, post-event B2, post-event B3, pre-event B11, pre-event B2 and pre-event B4. According to power set evaluation indicated that % 99.92 OA can be obtained from S2 bands including pre-event B2 GLCM mean, post-event B3

GLCM max, B4 GLCM mean, B3 GLCM homogeneity, B8 GLCM correlation and B4 GLCM variance. In addition, the FI result of pre- & post-event VV and VH data, the most effective Sentinel-1 bands are post-event VV and pre-event VH as shown in Table 5.7.

Table 5.7. Testing feature importance score of S1 and S2.

		Score	Accuracy	Precision
Sentinel 2 bands	Post-event B11	0.4044	0.1156	0.3874
	Pre-event B2	0.1563	0.0446	0.0959
	Pre-event B11	0.0892	0.0255	0.0808
	Pre-event B4	0.0818	0.0234	0.0535
	Post-event B3	0.0087	0.0025	0.0082
Sentinel 1 bands	Post-event VV	0.6999	0.2000	0.3323
	Pre-event VH	0.6500	0.1857	0.3793
	Post-event VH	0.4355	0.1244	0.2603
	Pre-event VV	0.2134	0.0610	0.1364

5.2. Results from Ordu Site

This section presents the flood mapping results for the Ordu floods (2018) in detail. The feature maps, the flood maps obtained with different feature sets, and the validation results in terms of confusion matrices between the identified classes, overall accuracy, user's and producer's accuracy, the Kappa value, and the F-1 score are presented in the following. Visual assessments based on an orthophoto acquired after the event for the Ordu flood were also carried out as can be seen in section 5.2.2.

5.2.1. Feature Maps Produced for Ordu Site (GLCM, Indices and PCA)

Texture measurements and PCA have been also applied to pre- & post-event S1 and pre-event S2 data in the Ordu study area. Post-event S2 data is not used any process except the training dataset delineation because of high cloud percentage. A selection of textural features produced as a result of applying 10 GLCM measurements to the pre- & post-

event S1 data is given in Table 5.8. The PCA was individually applied to pre- & post-event VV and VH datasets, each containing 10 texture features. The PCs and information percentages obtained as a result of PCA are given in Table 5.9.

Table 5.8. Overviews of selected textural features produced from S1 over Ordu site.

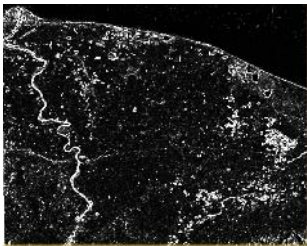
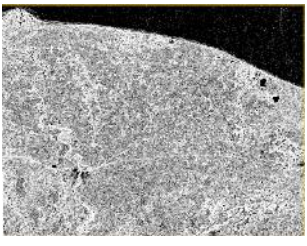
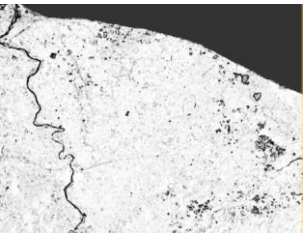
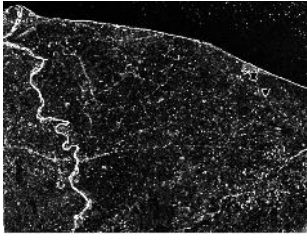
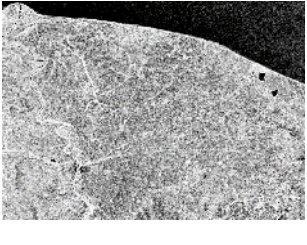

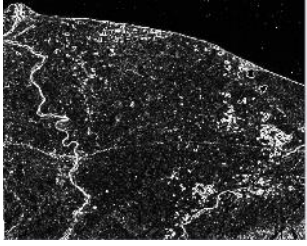
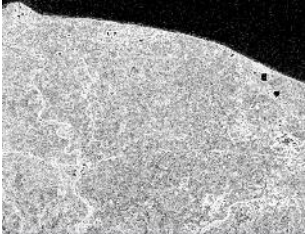
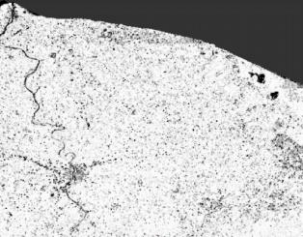
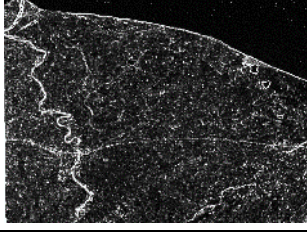
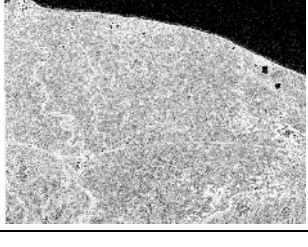
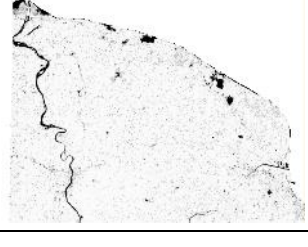
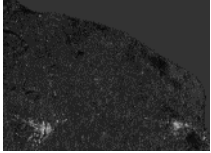
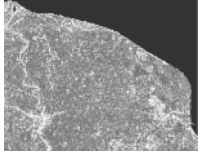
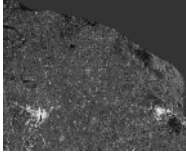
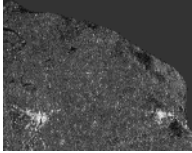
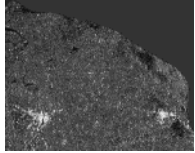
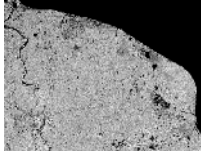
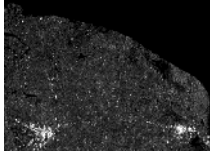
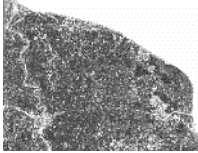
Inputs		GLCM Measurements		
		Contrast (0.00 – 1.0)	Entropy (0.00 – 9.5)	Correlation (0.00 – 1.00)
Sentinel-1 VV	Pre-event			
	Post-event			
Sentinel-1 VH	Pre-event			
	Post-event			

Table 5.9. Overviews of GLCM PCs derived from the S1 and their information percentages over Ordu site.

Inputs	Sentinel-1 VV		Sentinel-1 VH	
	PC ₁	PC ₂	PC ₁	PC ₂
Pre-event	 95%	 5%	 82%	 18%
Post-event	 96%	 4%	 87%	 13%

For the feature extraction of pre-event S2 dataset, GLCM features and spectral indices that include NDVI and MNDWI were produced. Table 5.10 represent NDVI and MNDWI produced from pre-event S2 data. A selection of 50 textural features produced as a result of applying 10 GLCM measurements to the pre-event S2 bands are given in Table 5.11. As a result of applying PCA to these 50 texture features, the PC₁, PC₂ and PC₃ (53%, 38% and 9% information, respectively) given in Table 5.12 were obtained.

Table 5.10. Overviews of spectral indices derived from S2 datasets over Ordu.

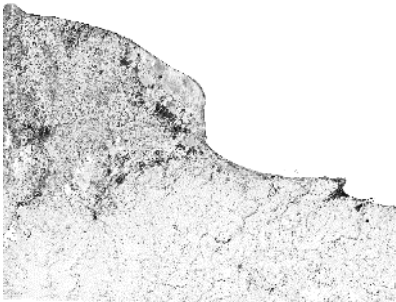
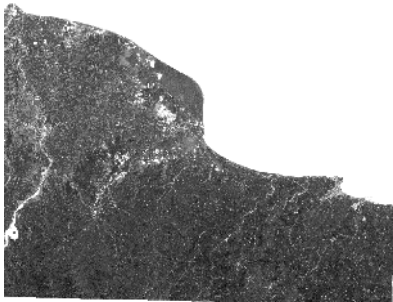
Inputs	Sentinel-2	
	NDVI	MNDWI
Pre-event (-1.00 – 1.00)		

Table 5.11. Overviews of the textural features produced from S2 datasets in Ordu.

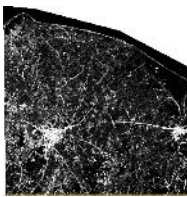
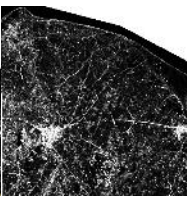
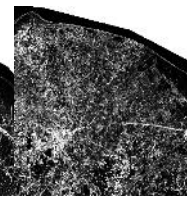
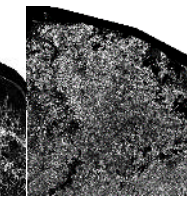
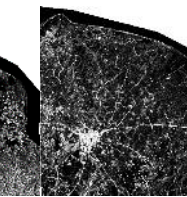
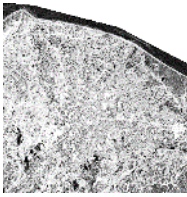
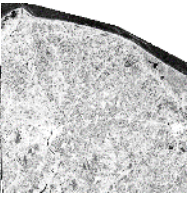
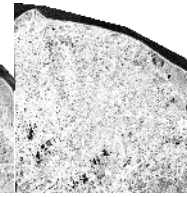
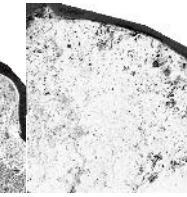
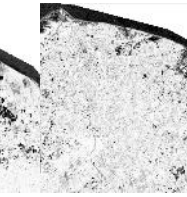
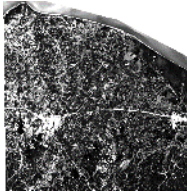
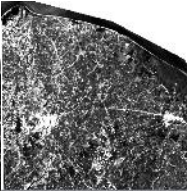
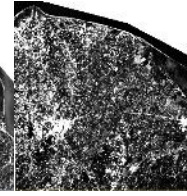
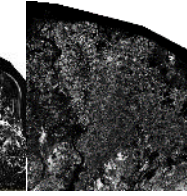
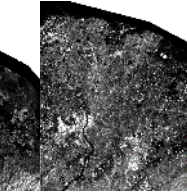
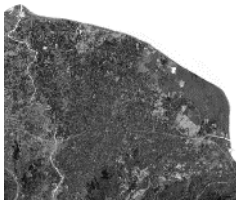
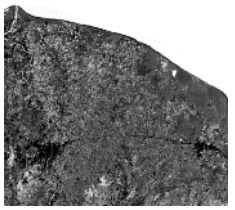
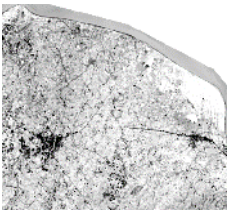
Inputs	Sentinel-2					
	Red (B2)	Green (B3)	Blue (B4)	NIR (B8)	SWIR (B11)	
Pre-event	Contrast (0.00 – 1.0)					
	Entropy (1.00 – 8.00)					
	Variance (0.00 – 1.0)					

Table 5.12. Overviews of the PCs derived from S2 GLCM features and their information percentages over Ordu site.

Inputs	Sentinel-2		
	PC ₁	PC ₂	PC ₃
Pre-event	 53%	 38%	 9%

5.2.2. Flood Maps and Validation Results

To evaluate the contribution of the GLCM PCs on class prediction, original S1 and S2 data, NDVI, MNDWI and produced GLCM PCs were stacked with different combinations. For this purpose, while the bands in Stack 1 were pre-event S2, NDVI and MNDWI, pre- & post-event S1, Stack 2 was obtained by adding S1 GLCM PCs and S2

GLCM PCs to Stack 1. For the classification process, the outputs of which are given in Figure 5.4, a total of 65,281 training samples manually delineated from pre- & post-event S2 were used with the same parameters (tree size of 300) as a previous study site. The RF parameters were previously tested by Tavus et al. [180] and found suitable. Prior investigations conducted by Tavus et al. [73, 128, 135] have indicated that opting for a comprehensive land use/land cover (LU/LC) classification, in contrast to a binary classification approach for flooded areas, enhances the accuracy and reliability of flood extent maps. Hence, the pre- and post-event S2 images were used to identify the following six classes: flooded area (FL), flooded vegetation (FV), permanent water (PW), crop (CR), urban area (UR) and forest (FR).

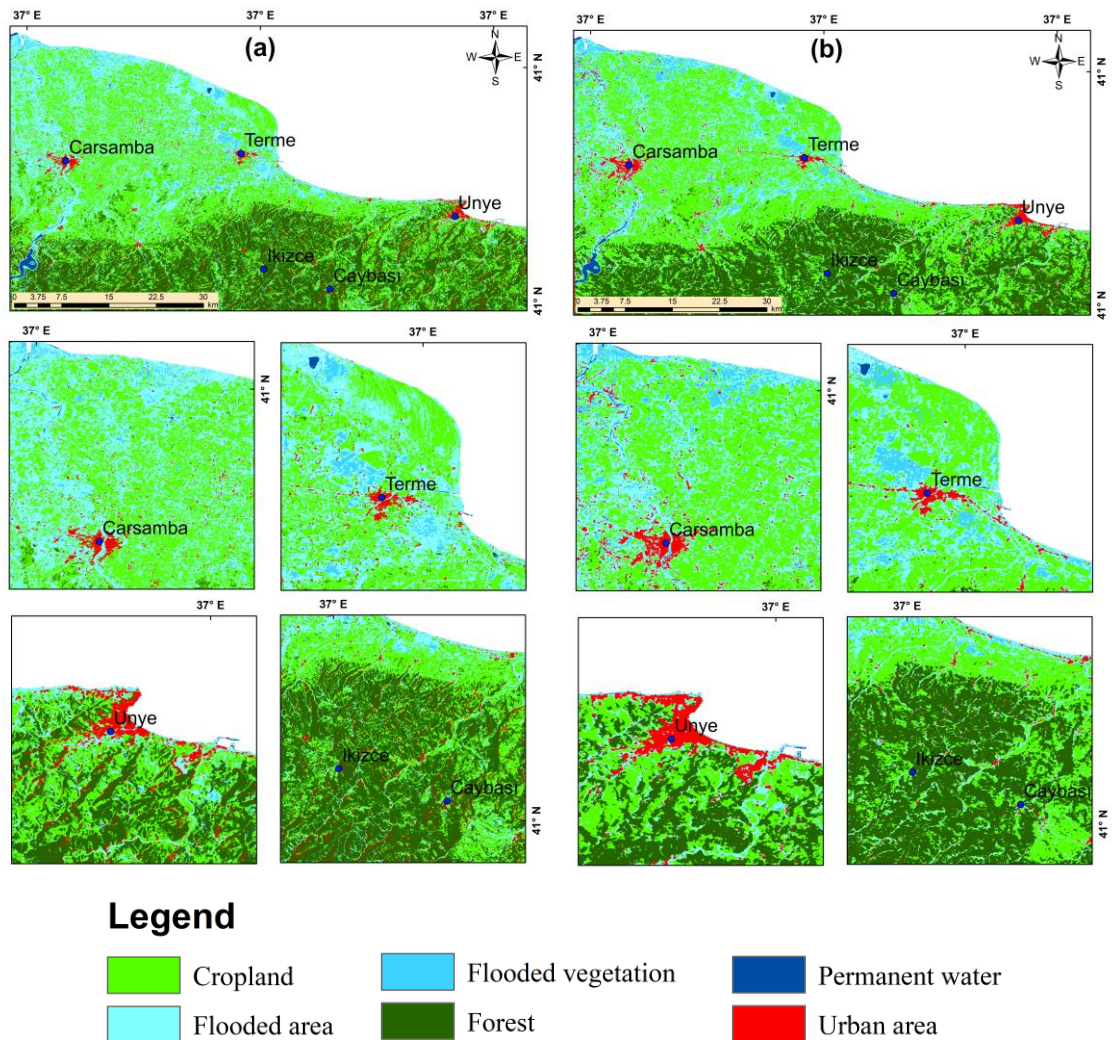


Figure 5.4. The RF classification results obtained from (a) Stack 1, (b) Stack 2.

The flood maps produced from Stack 1 and 2 features and their detailed views of sub-areas are presented in Figure 5.4 (a) and (b). As a result of the visual evaluation of the flood map given in Figure 5.4 (a), it was observed that all classes, especially the CR, FR, UR and FL areas, exhibit a noisy pattern. In the scenario where GLCM data is used, it is possible to say that the noisy structure in these classes has been greatly improved (Figure 5.4 (b)). In addition, as a result of visual inspections, no significant change was observed in the PW class within all classes. In addition, as seen in Figure 5.4 (b), it is noteworthy that the mixing between FV and FL class is reduced by the use of GLCM features.

The problem of labeling the FV class as FL in Figure 5.4 (a) according to Carsamba and Terme sub-areas was greatly reduced by the use of GLCM texture features (Figure 5.4 (b)). On the other hand, the Unye and Terme sub-areas were inspected in detailed views, and it was observed that the floods in the urban areas were better determined with Stack 1. The use of texture information has led to the fact that flood pixels occurring in urban areas were largely labeled as urban pixels. Also, while using the GLCM data (Stack 2) gives better results in detecting the urban pixels (Unye and Terme) in a rather open area, non-using the GLCM data (Stack) is more effective in detecting the urban pixels (Ikizce and Caybası) in the dense forest area.

Table 5.13 represents confusion (error) matrices between the related classes and their PA and UA and F-1 score values separately for each class. In addition, the OA and K values for each classification result are given in the tables. The overall accuracies (OA) achieved from the Stacks 1 and 2 were 92% (without GLCM) and 97% (with S1&S2 GLCM), respectively. The OA values show that the integration of GLCM PCs produced from S1 and S2 provided the best prediction performances for all classes. According to the confusion matrix produced from Stack 1 and 2, 92% OA and 87% K values in Stack 1 increase to 97% OA and 95% K values in Stack 2, respectively (Table 5.13). In Stack 2, F1-score for the cropland, flood, flooded vegetation, forest, permanent water and urban area classes were 0.98, 0.97, 0.92, 0.96, 0.97 and 0.93 respectively. The improvement in F1-score occurred for cropland and flooded vegetation classes, increasing by 0.1 and 0.08, respectively.

Table 5.13. Confusion matrix produced from the classification of Stack 1 and 2, along with the accuracy metrics over Ordu site.

		Cropland	Flood	Flooded Vegetation	Forest	Perm. Water	Urban	UA (%)
Stack 1	Cropland	5180	14	0	4	0	0	99
	Flood	221	24316	66	35	9	276	97
	Flooded Veg.	496	1251	8528	662	0	470	74
	Forest	421	93	3	5763	0	0	91
	Perm. Water	0	1174	166	0	10442	19	55
	Urban	185	121	4	0	0	5562	94
	PA (%)	80	90	97	89	99	87	
	F1-score	0.88	0.93	0.84	0.90	0.93	0.91	
Overall Accuracy: 92% Kappa (K): 0.87								
Stack 2	Cropland	8559	3	0	0	0	0	99
	Flood	32	20406	57	1	7	347	97
	Flooded Veg.	111	464	10565	338	28	400	88
	Forest	100	0	0	5980	0	0	98
	Perm. Water	0	149	280	0	10962	10	96
	Urban	0	103	0	0	0	6379	98
	PA (%)	97	96	96	94	99	89	
	F1-score	0.98	0.97	0.92	0.96	0.97	0.93	
Overall Accuracy: 97% Kappa (K): 0.95								

External reference source is not available for producing of accuracy metrics in this study area. For this reason, the orthophoto produced by Kocaman et al [181] and media photographs were used for visual comparison. Aerial photogrammetric datasets acquired on 17 August 2018 (9 days after the flood) by the General Directorate of Mapping (GDM), Türkiye. In Figure 5.5, the some overviews of flood map produced from Stack 2 are presented together with the 30 cm resolution orthophoto produced from aerial images. Additionally, photographs representing flood in urban and rural areas along with the corresponding of flood map produced from Stack 2 and orthophoto are given in Figure 5.6. In the figures, the blue points represent the corresponding flood areas in the classification result and in the orthophoto.

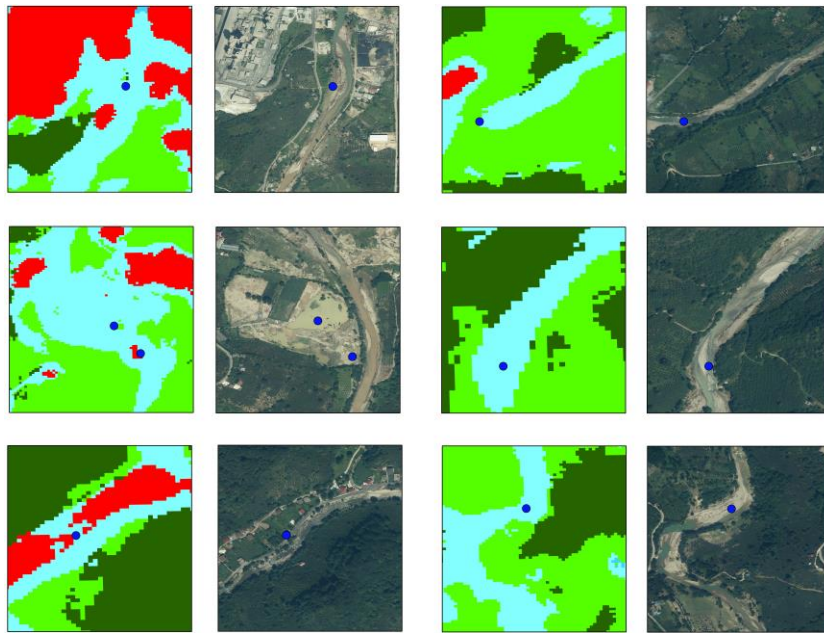


Figure 5.5. Flood map obtained from Stack 2 and 30 cm resolution orthophoto acquired on 17 August 2018. Blue dots illustrate conjugate points between the flood maps and orthophotos.

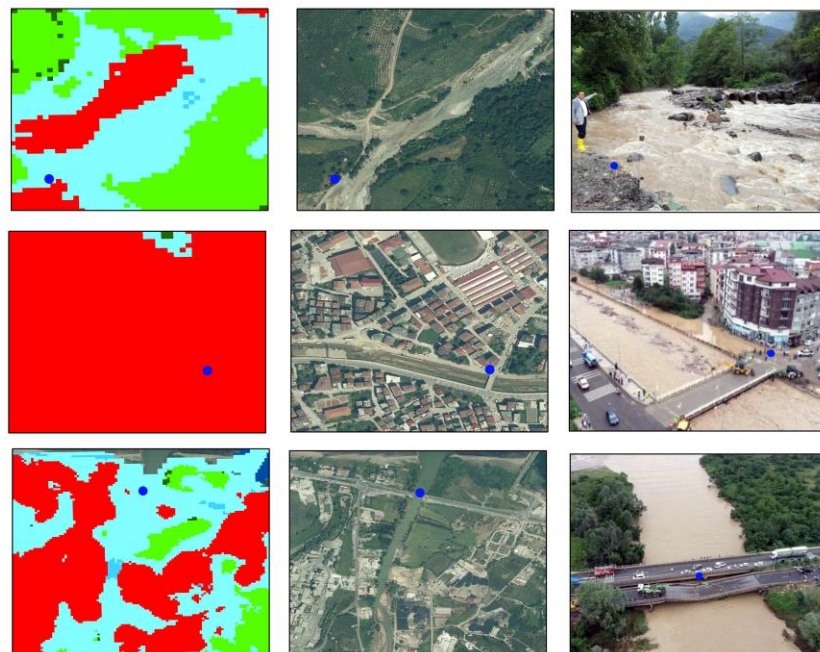


Figure 5.6. Flood map obtained from Stack 2, 30 cm resolution orthophoto acquired on 17 August 2018 and ground photos. Blue dots illustrate conjugate points between the flood maps, orthophotos and media photographs.

6. DISCUSSION

In this section, the results produced from the thesis are discussed from the perspectives such as the use of radar and optical data, data availability, the use of textural features and the effect of topography.

The aim of this thesis was to develop an approach for the integrated use of satellite optical and radar datasets based on the diverse features produced from both, and to contribute to the literature and future studies with conclusions and recommendations. For this purpose, the ability of Sentinel-1 and Sentinel-2 (S1 and S2) to generate flood maps was investigated based on two case studies. The first of these is a dam failure case, in which pre- & post-event S1 and S2 data and external reference data (PlanetScope) are available. Since the area is rather flat and the flood disaster was caused by dam failure, the post-event S2 data was cloud-free and the S1 data was not distorted due to topography. The Ordu flood case represents a more common situation in flood disasters, heavy precipitation and rugged topography unlike Sardoba event.

The data sets used in this thesis are S2 and S1 have been increasingly used in the literature thanks to the regular global coverage and free distribution, as also stated by Zoka et al. [83] and [84]. The results obtained were evaluated qualitatively based entirely on visual comparison with external reference data (PlanetScope). In addition, quantitative analyzes were performed on a class basis using a set of measures described in section 3.6 and also calculated from PlanetScope data.

6.1. On the use of radar and optical data and features

Studies on the determination of permanent water and especially large-spread flooded areas from SAR data indicate the success of the SAR data when suitable field conditions

are provided. This primarily occurs because the backscatter from open waters is considerably lower when compared to the backscatter from the adjacent land surface areas. Among the satellites equipped with SAR sensors, the S1 stands out as the most popular choice due to its cost-free access, relatively frequent revisit schedules, and a multi-year data archive that extends back to 2014 [182]. Sentinel-1 is equipped with radar sensors that can "see" through clouds and operate day and night, making it especially useful during periods of heavy cloud cover or darkness. It measures the backscatter of radar signals, which can effectively differentiate between open water and flooded land areas due to the distinct reflective properties of water. This ability makes Sentinel-1 a valuable tool for detecting flood extents even in challenging weather conditions. A wide variety of methods have already been published in the literature for flood extent mapping from S1 sensor, including various approaches as described in Section 3.4. The main of these methods are change detection based approaches [116, 117], thresholding methods [55, 67, 89], bayesian [183, 184] and machine learning methods [24, 125, 127]. The methods evaluated in this context have proven their success.

Nonetheless, in the presence of windy conditions and/or vegetation cover, the water surface becomes turbulent, causing an increase in backscatter, which decreases the contrast between flooded and non-flooded areas [185]. In such circumstances, the detection of flooded areas becomes more challenging. Furthermore, although there are reviews [54, 113, 182] and evaluations of these flood and inundation mapping methods using S1 sensors, direct investigation of the performance of S1 sensor is constrained. Here, in order to investigate the effect of radar and optical data on the prediction performance, the results of Stack 1, which includes only S1 data and derived features, and Stack 2, which includes only S2 bands and features, were analyzed. According to confusion matrix produced from Stack 1, OA and Kappa values were 71% and 0.62. Tupas et al. [186] mapped floods by using S1 images only, and the results based on change detection were compared with the S2 data, resulting in a peak OA of 83%. The studies conducted by Shahabi et al. [187], which aimed to map the same flood event with Sentinel-1 data, obtained OA values of 78% and 91%, respectively. Nevertheless, it is important to highlight that the analyses discussed in this context only involve the two classes: flood and non-flood. Additionally, these methodologies have predominantly been employed in cases of river basin flooding, which may not be as applicable to areas

characterized by intricate flood dynamics and different LULC categories. Also, despite S1 being cloud-independent and can therefore be used in flood-triggering weather conditions, it was not possible to identify flooded vegetation and bare land areas from this sensor alone. Difficulty in visual interpretation of existing LULC classes found in S1 data brings with it the need for additional information about the plots.

On the other hand, S2 carries an optical sensor that captures high-resolution images of the Earth's surface. The images provide detailed information about land cover, including vegetation, urban areas, and water bodies. While optical imagery can be affected by cloud cover, it offers the advantage of finer spatial resolution and can help identify subtle changes in landscape features caused by flooding. S2, which is used as optical data in this thesis, is the optical data preferred in many global or regional natural disasters such as flood [37], drought [188] and earthquake [189] in the literature. Thanks to the high resolution of S2 data, providing detailed analysis opportunities at fine scale, and the information provided by visible and near infrared bands, its potential has been investigated in many flood mapping studies [35-38]. S2 data was used for training dataset production in some of these studies, validation source in others, and for both purposes in most of these studies. One of the most important advantages of S2 data within the scope of flood mapping is that it enables the production of spectral indexes that provide information such as vegetation, water, and moisture used in many studies [37, 164]. For example; for the same area, flood maps with 64% and 74% OA, respectively, were produced in the studies carried out by Caballero et al. [37] and Phiri et al. [164], using the spectral indices produced from the S2 data together with the RF method. In this thesis, the OA and Kappa values were found to be 79% and 0.75%, which were superior to the results of the flood map produced only in S2 and its features, only in S1 and its features. Here, the OA and Kappa values were found to be 79% and 0.75%, which were superior to the results of the flood map produced only in S2 and its features, only in S1 and its features. When the results are compared with the results of Caballero et al. [37] and Phiri et al. [164] studies including Built-up, vegetation and flood classes, it was seen that the approximate OA value is achieved with basically the same classification method (RF). It should be noted here that as an advantage of the method proposed in the thesis, the inclusion of all LULC classes present in the pre- & post-event S2 data in the classification process will positively improve the result. At the same time, as explained in Section 5.2,

S2 data allows visual interpretation of flooded vegetation and bare land classes, unlike S1 data, which is seen as one of the important advantages of S2 data over S1 data.

By integrating data from both S1 and S2, flood mapping efforts benefit from the strengths of each satellite. S1 radar data can reliably detect the presence of water, even when clouds obstruct the view. S2 optical imagery can provide context by showing changes in land features associated with flooding, and it can supplement flood maps with additional information about the surrounding environment. To leverage the complementary nature of these two datasets effectively, researchers and scientists employ advanced techniques that fuse the radar and optical data. This fusion enhances the accuracy of flood extent delineation and can also provide insights into flood dynamics, such as water flow direction and velocity. The combination of S1 and S2 satellite data has emerged as a powerful approach for enhancing flood mapping efforts. These two satellites offer complementary information that collectively improves the accuracy and reliability of flood detection and mapping. Complementary use of S2 and S1 data mentioned above has a great potential to produce essential features the use color, brightness, texture, shape, surface roughness and smoothness etc. to detect flooding in areas with different constructions and topography. In conclusion, the combined use of S1 and S2 data has proven to be a valuable strategy for flood mapping. By capitalizing on their individual strengths, these satellites contribute to a more comprehensive understanding of flood events, enabling better preparedness, response, and recovery efforts in flood-prone regions.

Literature studies using both optical (S2) and radar data (S1) are given in detail in Section 2.3. Within the scope of this thesis, by using the above-mentioned S1 and S2 data and the spectral and texture features produced from them together, a flood map containing 7 classes, including flooded area, permanent water, flooded vegetation, urban area, bare land and two types of vegetation, was obtained with 86% OA. This result is higher than the scenarios where only S1 and only S2 data are used, as supported by different methods in the literature. In addition, the results of this scenario were reported by Huang and Jin [90], Manakos et al. [91], Lal et al. [98], Slagter et al. [92], Singha et al. [93], Hakdaoui and Emran [95], and Konapala et al. [11], it was seen that the classification success rate

was carried forward. The common result of these studies showed that although using S1&S2 together led to considerably higher accuracies, relatively poor for classifications in high-vegetated wetlands, as sub-canopy flooding.

6.2. Data availability

One of the focal points of this thesis revolves around addressing the challenge of inadequate S2 data accessibility during and following flood occurrences, primarily due to cloud cover interference. At the same time, as stated in the study by Huang and Chin [90], the S1 data has some limitations, such as the requirement to have prior information of the backscatter distributions of the relevant surfaces in dry and wet conditions. In addition to the aforementioned limitations, the inability to determine LULC classes representing the whole study area from only S1 data both in this thesis and in the literature revealed that there is a need for a detailed analysis of this subject. For this reason, this thesis takes into a comprehensive analysis of diverse data availability scenarios essential for generating accurate flood maps. This research phase involves the in-depth analysis of features in different data stacks, allowing for an investigation into the influences of data availability scenarios and their impacts on various classes of prediction efficacy. In other words, of notable significance is the issue of flood hazard assessment, where in the susceptibility of S2 data to meteorological conditions emerges as a significant constraint in numerous flood mapping efforts. Contextually, the methodology proposed in this study addresses the crucial limitation of data availability and conducts an in-depth analysis of features using the combined potential of S1 and S2 data sources for flood mapping.

Here, the datasets analyzed in above-mentioned scope are Stack 3 and Stack 4, as there is no problem that prevents the use of the data to a large extent if Sentinel-1 is present before and after the event. Stack 3 represents the analysis of scenarios where post-event Sentinel-2 data cannot be used as input in classification. Therefore, Stack 3 was created to consider that pre-event Sentinel-2 data is usually available to contribute to S1. Stack 4, on the other hand, represents a data group in which pre- & post-event S1&2 data are usable, which is generally not the case in flood events (detailed information in the Chapter 3.4.4).

According to the confusion matrix produced from Stack 3, the OA and Kappa values, which were superior than the results of Stack 1 and 2, were 82% and 0.76. Also, the scenario where all data is available is represented by Stack 4. Based on the confusion matrix derived from Stack 4, the OA and Kappa values were calculated to be 86% and 0.83, respectively. According to this result, it is possible to say that Stack 3 produces results with slightly less accuracy than Stack 4. Considering the kappa values explained in detail in Section 5.1.2 and produced on a class basis, it is advisable to use pre-event S2 data together with the pre- & post-event S1 data to accurate determination of the non-flood classes. In addition, the fact that PW and Ur classes have the highest kappa values in this scenario supports this argument. Also, according to research conducted by Tarpanelli et al. [185] in recent year, showed that nearly 58 % of flood hazards in Europe are potentially observable by S1 and just 28 % by S2 because of the cloudy conditions. In this thesis, it is clear that the performance of the use of pre-event S2 data together with the pre- & post-event S1 will contribute to the mapping of flood disasters by increasing these percentages. As a matter of fact, this scenario was applied to the Ordu study area, where the post-event S2 data could not be used because of the dense cloud content, and a classification result with 99% OA was obtained. However, it should be noted that the accuracy value calculated here should be validated with an external reference source.

Another aspect in evaluating different data scenarios is that the strategy for delineating the training data varies with each data stack. That is, as detailed in Section 5.2, it can be seen in Figure 5.1(c) that six other LULC classes (Fl, PW , V1, V2, Ur, and BL) can be defined apart from the flooded vegetation class with Stack 3 . Here, since the post-event Sentinel-2 data was not available and the flooded vegetation was not visible in the post-event Sentinel-1 data, this class (FV) could not be defined. If post-event S2 data is available, all LULC classes available in the study area are defined. As a result of this, it is possible to say that its performance on the determination of the FV class, which represents the flooded agricultural areas, is insufficient according to the visual inspection result made on the post-event S1 data. Considering all this analysis, the combination of pre- & post-event S1 and pre-event S2 data is recommended both to increase the number of LULCs that can be detected and to provide a higher classification result, even if there is no post-event S2 instead of using only S1 or S2 data.

6.3. On the use of textural features and effect of topography

There are very few studies in the literature investigating the potential of GLCM texture features on flood mapping. These studies focused on the contribution of texture information to the assessment of floods in dense vegetated or forested and urban areas. For example, It is stated that GLCM features produced from COSMO-SkyMed SAR data by Dasgupta et al. [190] increased the overall accuracy of flood mapping from 93% to 95%. Similarly, Senthilnath et al. [148] stated that the accuracy assessment result with mean shift segmentation for flood mapping is quite promising compared to GLCM. Amitrano et al. [70] evaluated the S1 GLCM features and reported that the homogeneity and contrast features performed well. In addition to the success of GLCM, the common result of these studies using different data is that the GLCM features that give the best results vary according to the data and topographical characteristics. At the same time, optimizing parameters such as the window size required for calculating GLCM texture fetures is also application dependent for the same reasons.

For this reason, in this thesis, 10 GLCM features were calculated from the data that varied according to the scenarios, and the number of features was optimized by applying PCA. When we look at the outcomes and compare them to the initial findings of Tavus et al. [180], using the RF method and without considering the GLCM and PCA analysis, there is a notable improvement. Furthermore, the method suggested here shows improved classification for urban and bare land. Based on the confusion matrix generated from Stacks 4 and 5 with and without GLCM feature components given in Section 5.2.1, the 86% OA and 83% K values in Stack 4 decrease to 68% OA and 60% K values in Stack 5, respectively. As evident from both the classification results and the error matrices, the utilization of of GLCM data yields a considerably improvement in classification accuracy, effectively decreasing the confusing between FV and FL classes. In cases where GLCM is not used, over 75% of FV class pixels were misclassified as FL, whereas no such confusion between FV and other classes. To elaborate, the absence of textural features led to the labeling of flood regions as urban and vegetated areas. It is clear that the radar data exhibits a different scattering mechanism for inundated vegetation when contrasted with other classes. This finding emphasizes the difference in texture

characteristics of the flooded vegetation, specifically in contrast to the flood, water, or other cropland in the area.

The impact of GLCM feature components was assessed when the proposed method to the Ordu case area, as detailed in Section 4.2, which has distinctly different topographical characteristics. The results demonstrated a substantial improvement in overall classification accuracy (99% with GLCM and 93% without GLCM). It is apparent that flooded vegetation displays a distinct radar data scattering pattern in contrast to other classes. This finding highlights the contrast in textural characteristics of flooded vegetation when compared to floods, bodies of water, or other agricultural areas within the region. Consequently, the use of GLCM data plays an important role in significantly enhancing classification accuracy, particularly by preventing confusion between the FV and FL classes.

7. CONCLUSION AND FUTURE WORK

This chapter involves the main outcomes and the limitations as conclusions. In the second part, remaining challenges are identified and recommendations for future studies are also given.

7.1. Conclusions

Floods are the most common and costly type of natural hazard according to criteria such as frequency, distribution, area of impact, unpredictability, power, and duration. Considering the direct or indirect destructive effects on the socio-economic, environment and human life, it is of great importance to deep understand the dynamics of floods. Because the magnitude and types of damages depend on flood location, extent, and inundation level, flood mapping and monitoring are crucial for accurate impact assessment and effective disaster risk management. For this purposes, traditional methods face frequently challenges in evaluating flood dynamics because of the data limitations caused by floods nature and the rapid movement of water bodies. In this scope, remote sensing technologies and EO data collected from satellite platforms provide the necessary tools and data for the monitoring and assessment of floods. The most frequently used pairs of sensors that can serve this purpose are optical and radar sensors, the advantages and disadvantages of which are given in detail in Section 2.3.

Integration of SAR and optical data has a great potential to produce essential features such as color, brightness, texture, shape, surface roughness and smoothness, water content, etc., to detect flooding in areas with different constructions and topography. On the other hand, as technology advances and data accessibility improves, the fusion of heterogeneous information from optical and radar data is still an active research area to synthesize the advantages of both sensors in the scope of flood mapping and monitoring. Among these sensors, the most preferred ones are S1 SAR and S2 optical satellites, due to their regular global coverage and free data distribution policy.

This thesis developed a feature-level data fusion methodology for flood extent mapping using optical and radar data, in particular by using the S1 SAR and S2 satellites of ESA. The proposed method was developed in the case of the Sardoba dam flood, which flooded some regions of Uzbekistan and Kazakhstan and caused serious disasters on human lives, settlements and croplands. The event chosen here is ideal for developing a fusion method, as it is not affected by SAR distortions due to its topographical characteristic, there is no cloud problem in optical thanks to the absence of precipitation, and moreover, PlanetScope external data is available for the validation process. In addition, since the large part of the area is cropland, it also allowed detailed analysis of the flooded (or inundated) vegetation. A data-driven LULC classification approach with the RF method is presented with different auxiliary features comparatively for different Sentinel-2 and Sentinel-1 data availability scenarios. As auxiliary features, the use of GLCM features and water and vegetation indices, which were rarely analyzed until now and produced from SAR and optical data, with PCA were investigated in detail. The method and scenario type proposed here is applied to a second area, namely Ordu flood event, which has a very rough topography and is caused by precipitation, unlike the Sardoba event, and its results are analyzed.

According to the results, although single SAR intensity is the most preferred data for the detection of permanent water bodies (PW) in the literature, this class has the highest kappa value (0.90) in the scenario containing pre- & post-event S1 and pre-event S2 data in the thesis. Although the number of approaches related to flooded vegetation (FV) is more limited compared to the PW class, the change in backscatter mechanisms between multi-temporal SAR intensity stands out as the main indicator of this class. At the same time, approaches to FV determination, which are highly dependent on the characteristics both area and data used, tend to be supervised rather than automated. As a result of this thesis, it has been seen that it is not possible to determine the FV class with the supervised approaches from only S1 data, especially if there is no prior-information about the area, which is common in flood disasters. According to the classification results, it is recommended to use S1 and S2 data together for this class, which can be determined by the contribution of GLCM principle components by 60% (kappa values are 0.56 and 0.86 with and without GLCM PCs, respectively). These findings illustrate the potential of the use of S1 and S2, for FV according to only S1 or S2 together with the importance of the

proposed auxiliary features. It was not possible to determine the floods that occurred under the dense forest areas analyzed in the second study case (Ordu), since no difference could be observed between flooded and non-flooded conditions in both S1 and S2 data. On the other hand, the successful determination of the forest class in the classification results shows that the S1 and S2 sensors are insufficient in the analysis of floods occurring in forest areas in this thesis. On the other hand, according to a visual comparison of classification results, the use of GLCM PCs contributed to the successful determination of forest class and changes caused by flooding in the river basin. However, the results show that the S1 and S2 sensors together with the proposed approach are insufficient in the analysis of floods occurring in the forested areas.

Although studies investigating urban floods are rare in the literature, it is possible to say that the methods used SAR intensity together with InSAR coherence, defined as the complex correlation between the phases of the returned signals, have come to the fore in recent years. As can be seen in both study areas applied within the scope of the thesis, since flood disasters spread over large areas, there are also settlements within the impact areas. The type that is specified as urban flood in the literature could not be determined with the proposed method and the sensors used in this thesis, just like the floods that occur in forest areas. Besides InSAR coherence, polarimetric parameters, which provide insight into the backscattering mechanisms and are calculated by decomposition methods, can improve the detection of both urban and flooded pixels (in vegetated and forested areas). In addition, it is clear that the flood types mentioned so far that cannot be determined well enough because of the sensor limitations will make progress thanks to L-band missions with open data policies such as NISAR and the ROSE-L mission, which are planned to be operational in the future.

As a significant finding, the necessity of using pre-event S2 bands and features derived from them has been proven in cases where post-event S2 data cannot be used as an input for classification. While the presence of stable water in the floodplain enables the detection of flood extents a few days after the flood peak, it's important to note that in most cases, the average duration of a flood event spans approximately 2.5 to 3.5 days [185]. In the same study, it was stated that about 58% of the floods in Europe could

potentially be observed by S1, and only 28% could be observed by S2 because of cloudy conditions. This finding, produced as a result of the thesis, will undoubtedly contribute to the mapping of the 58% flood observed by S1 and more flood disasters can be analyzed by using the pre-event S2 data.

The performance of flood detection varies in regions with different characteristics such as topography and land use land cover (LULC) types. Consequently, each of these features has significant importance in the context of flood mapping. According to this, flood extent mapping based on ML classification should not be binary (flood and non-flood) and it is recommended to use related LULC classes including flooded vegetation for obtaining high accuracy. Furthermore, the suggested methodology demonstrates a high potential for accuracy and applicability across various sites under flat and hilly topographical terrain as well as different land cover conditions, making it effective for mapping floods and assessing damages.

Additionally, the optimal feature types proposed in the methodology improved in all LULC types evaluated except the permanent water class. The feature types involve textural features obtained from gray level co-occurrence matrix (GLCM) variables and spectral indices produced for vegetation and water. The major advantage of using these features is that they significantly improve flood observations, specifically, flood and flooded vegetation classes, which are critical in most studies. Finally, the proposed methodology exhibits a notable potential for accuracy and can be effectively employed in various locations to map floods and assess damages, with a particular emphasis on cropland areas. In this context, in countries such as Türkiye where precise crop pattern information is not available, it is considered that it will be beneficial for the studies conducted by some institutions (e.g. AFAD) to determine the supports to be given to agricultural land owners after the flood.

Also from another point of view, when the results are compared with Tavus et al. [180], with the RF method without GLCM and PCA analysis, it is possible to say that observe a significant improvement in the scenario, which includes all the data. The proposed method in this thesis demonstrates better performance for urban areas and bare land. In

contrast, Tavus et al. [180] achieved a 99% overall accuracy (OA) based on test data that had been split from training data. Here, OA values ranging from 68% to 86% for all five scenarios are a clear indication that external reference should be preferred for validation.

In this thesis, a series of accuracy metrics were produced, such as OA and kappa coefficient for accuracy evaluation, and PA, UA and F1-score for class-based accuracy. As discussed in the previous sections, although the OA and kappa values of the different scenarios were high, visual inspection of the classification results revealed class-based underachievement. For example, the OA and kappa values greatly overestimates the accuracy of the flooded and flooded vegetation classes (e.g. in the Stack 5 result). A similar situation applies to the bare land class in the Sardoba study area, which is much smaller than other LULC classes. However, no such limitation was encountered in the PA, UA and F1-score produced for each class. Therefore, besides PA (recall or sensitivity) and UA (precision or specificity) values, the F1-score, which provides the balance between these two values, maybe a better metric if there is a homogeneous and uneven LULC distribution in the study area. In addition, especially in studies carried out for emergency relief and damage assessment, it would be more appropriate to perform an accuracy assessment for classes such as settlements and agricultural areas.

7.2. Future Work

Based on the results of the in-depth literature search and the proposed flood mapping methodology conducted within the scope of this Ph.D. thesis, the key findings, including various challenges and potential future improvements, are listed below.

1. Primarily, it was emphasized that it is critical to evaluate the available data and various features of these data in the most appropriate way, especially for flood disaster analysis, where there are many restrictions on the use of data for various reasons. The enhancement of data availability and technologies over time is an indication that this issue will continue to exist by preserving its importance. In the near future, SAR missions such as NISAR and ROSE-L, which have improved temporal and spatial resolution, as well as wavelengths and polarizations, are

expected to be operational with open data policies. On the other hand, while the complementary use of Sentinel-1 and Sentinel-2 are sufficient to detect flooded vegetation, as previously discussed in this thesis, they are insufficient to detect floods in forest and urban areas. In addition, urban floods, many of which are caused by sudden and dense precipitation, are increasing as a result of climate change. In this context, in the study of Tavus et al. [73] an urban flood (in Ankara) was analyzed with Sentinel-1 data, and similar to the literature, it was found to be insufficient. As a result, it is clear that the new SAR missions with higher spatial and temporal resolution and longer wavelengths will allow for in-depth analysis of forest and urban floods. In addition, the improvement in temporal resolution will contribute to the increase in the number of floods that can be analyzed and to the investigation of the hydraulic processes and flood characteristics.

2. Considering the potential of the proposed method to be beneficial in determining the support to be given to cropland owners after the hazard, need to precisely determine the crop pattern. In the literature, there are pioneering studies on different crops based on SAR and optical data. If the method proposed in the thesis is developed/combined with crop pattern analysis, it is inevitable to obtain fast, up-to-date and reliable data after the disaster.
3. One of the most important challenges encountered within the scope of the thesis is the lack of validation data used for the accuracy assessment. This challenge, which is frequently mentioned in literature studies, is an important problem that should be dealt with for the analysis of flood disasters that can occur anywhere in the world and at any time. As a matter of fact, since there is no external reference data in one of the study areas (Ordu) in the thesis, it could not be analyzed quantitatively. Of course, the improvements in the number and characteristics of the new sensors mentioned in the first matter will help to solve this problem. However, considering that the reference data to be used for validation should have better characteristics than the input data used to produce the results, these improvements are likely to be insufficient. Therefore, in future studies, post-flood indicators such as soil moisture should be investigated in detail and validation strategies should be developed. On the other hand, as in many areas, future flood mapping is expected to increasingly include social media content and crowd-

sourced data alongside EO data [191-193]. However, although the reliability and quality of these data, which have just begun to be researched, remain uncertain, the potential of flood disasters should be investigated by integrating them into both analysis and validation strategies.

4. In conjunction with the growing availability of data, there have been notable developments in supervised machine learning (ML) algorithms, particularly in the deep learning (DL) methods and Convolutional Neural Networks (CNNs). In this context, many attempts using high spatial resolution data such as Planet Scope and WorldView-2 or UAVs have resulted in high accuracy [48, 194, 195]. At the same time, the existence of publicly available datasets such as Sen1Floods11 proposed by Bonafilia et al. [196] which was produced to train and test DL flood algorithms from Sentinel-1 data, supports this research. As a state-of-the-art in this context, Rambour et al. [197] introduced a dataset called SEN12-FLOOD, which features Sentinel-1 and Sentinel-2 data for flood mapping. They reported an accuracy of 75% using Sentinel-1, while the combination of Sentinel-1 and Sentinel-2 yielded an impressive OA of 90%.

While the potential of these datasets for the development of ML algorithms is undoubted, all of the datasets in question are designed for the analysis of flood and non-flood classes. In this context, Tavus et al. [198] proposed a multi-class segmentation including the flood, flooded vegetation and non-flood using Sentinel-1 SAR data and DEM as inputs. In future studies, it is planned to both expand the dataset and modify the CNN architecture to use features from S1 and S2 sensors to improve overall results. It is also considered that the inclusion of different surface models in the dataset will contribute to water depth analysis studies.

8. REFERENCES

- [1] IPCC, Global Warming of 1.5°C. An IPCC Special Report on the impacts of global warming of 1.5°C above pre-industrial levels and related global greenhouse gas emission pathways, in the context of strengthening the global response to the threat of climate change, sustainable development, and reorts to eradicate poverty. **2018.**
- [2] Jonkman, S.N. and I. Kelman, An analysis of the causes and circumstances of flood disaster deaths. *Disasters*. 29(1): p. 75-97, **2005.**
- [3] Diakakis, M., G. Deligiannakis, A. Pallikarakis, and M. Skordoulis, Factors controlling the spatial distribution of flash flooding in the complex environment of a metropolitan urban area. The case of Athens 2013 flash flood event. *International journal of disaster risk reduction*. 18: p. 171-180, **2016.**
- [4] Ologunorisa, T. and M. Abawua, Flood risk assessment: a review. *Journal of Applied Sciences and Environmental Management*. 9(1): p. 57-63, **2005.**
- [5] Psomiadis, E. Flash flood area mapping utilising Sentinel-1 radar data. in *Earth resources and environmental remote sensing/GIS applications VII*. SPIE, **2016.**
- [6] Frazier, P. and K. Page, The effect of river regulation on floodplain wetland inundation, Murrumbidgee River, Australia. *Marine and Freshwater Research*. 57(2): p. 133-141, **2006.**
- [7] Klemas, V., Remote sensing of floods and flood-prone areas: An overview. *Journal of Coastal Research*. 31(4): p. 1005-1013, **2015.**
- [8] Huang, W., et al., Automated extraction of surface water extent from Sentinel-1 data. *Remote Sensing*. 10(5): p. 797, **2018.**
- [9] Potin, P., et al. Sentinel-1 mission operations concept. in *2012 IEEE international geoscience and remote sensing symposium*. **2012.**
- [10] Drusch, M., et al., Sentinel-2: ESA's optical high-resolution mission for GMES operational services. *Remote sensing of Environment*. 120: p. 25-36, **2012.**
- [11] Konapala, G., S.V. Kumar, and S.K. Ahmad, Exploring Sentinel-1 and Sentinel-2 diversity for flood inundation mapping using deep learning. *ISPRS Journal of Photogrammetry and Remote Sensing*. 180: p. 163-173, **2021.**

- [12] Fayne, J., J. Bolten, V. Lakshmi, and A. Ahamed, Optical and physical methods for mapping flooding with satellite imagery. *Remote Sensing of Hydrological Extremes*: p. 83-103, **2017**.
- [13] Rasid, H. and M. Pramanik, Areal extent of the 1988 flood in Bangladesh: How much did the satellite imagery show? *Natural Hazards*. 8(2): p. 189-200, **1993**.
- [14] Ali, A., D.A. Quadir, and O.K. Huh, Study of river flood hydrology in Bangladesh with AVHRR data. *International Journal of Remote Sensing*. 10(12): p. 1873-1891, **1989**.
- [15] Sheng, Y., P. Gong, and Q. Xiao, Quantitative dynamic flood monitoring with NOAA AVHRR. *International Journal of Remote Sensing*. 22(9): p. 1709-1724, **2001**.
- [16] Sheng, Y., Y. Su, and Q. Xiao, Challenging the cloud-contamination problem in flood monitoring with NOAA/AVHRR imagery. *Photogrammetric Engineering and Remote Sensing*. 64(3): p. 191-198, **1998**.
- [17] Jain, S.K., A.K. Saraf, A. Goswami, and T. Ahmad, Flood inundation mapping using NOAA AVHRR data. *Water Resources Management*. 20(6): p. 949-959, **2006**.
- [18] Yan, Y.-E., et al., Detecting the spatiotemporal changes of tidal flood in the estuarine wetland by using MODIS time series data. *Journal of Hydrology*. 384(1-2): p. 156-163, **2010**.
- [19] Ordoyne, C. and M.A. Friedl, Using MODIS data to characterize seasonal inundation patterns in the Florida Everglades. *Remote Sensing of Environment*. 112(11): p. 4107-4119, **2008**.
- [20] Brakenridge, R. and E. Anderson, MODIS-based flood detection, mapping and measurement: the potential for operational hydrological applications. Kluwer Academic Publishers. p. 1-12. **2006**.
- [21] Ticehurst, C., J.P. Guerschman, and Y. Chen, The strengths and limitations in using the daily MODIS open water likelihood algorithm for identifying flood events. *Remote Sensing*. 6(12): p. 11791-11809, **2014**.
- [22] Dao, P.D. and Y.-A. Liou, Object-based flood mapping and affected rice field estimation with Landsat 8 OLI and MODIS data. *Remote Sensing*. 7(5): p. 5077-5097, **2015**.
- [23] NRT Global Flood Mapping,
<https://floodmap.modaps.eosdis.nasa.gov/index.php>, Last Access: 14 December

- [24] Notti, D., et al. Low-cost flood mapping using free satellite data from Sentinels constellation. in EGU General Assembly Conference Abstracts. **2019**.
- [25] Kittel, C.M., L. Jiang, C. Tøttrup, and P. Bauer-Gottwein, Sentinel-3 radar altimetry for river monitoring—a catchment-scale evaluation of satellite water surface elevation from Sentinel-3A and Sentinel-3B. *Hydrology and Earth System Sciences*. 25(1): p. 333-357, **2021**.
- [26] Desrochers, N.M., et al., A remote sensing view of the 2020 extreme lake-expansion flood event into the Peace–athabasca delta floodplain—implications for the future swot mission. *Remote Sensing*. 15(5): p. 1278, **2023**.
- [27] Rango, A. and V.V. Salomonson, Regional flood mapping from space. *Water Resources Research*. 10(3): p. 473-484, **1974**.
- [28] Morrison, R., M. RB, and W. PG, Monitoring Flood Inundation. **1976**
- [29] McGinnis, D. and A. Rango, Earth resources satellite systems for flood monitoring. *Geophysical Research Letters*. 2(4): p. 132-135, **1975**.
- [30] Sajjad, A., et al., Riverine flood mapping and impact assessment using remote sensing technique: a case study of Chenab flood-2014 in Multan district, Punjab, Pakistan. *Natural Hazards*: p. 1-20, **2021**.
- [31] Mishra, V.K. and T. Pant, Change Analysis of Water Area and Flood Mapping using a Novel Water Index 2020 (WI2020) for Landsat Imagery. *Geocarto International*(just-accepted): p. 1-14, **2021**.
- [32] Cavallo, C., et al., Continuous Monitoring of the Flooding Dynamics in the Albufera Wetland (Spain) by Landsat-8 and Sentinel-2 Datasets. *Remote Sensing*. 13(17): p. 3525, **2021**.
- [33] Villalon-Turrubiates, I.E. Convolutional Neural Network for Flood-Risk Assessment and Detection within a Metropolitan Area. in *2021 IEEE International Geoscience and Remote Sensing Symposium IGARSS*. 2021.
- [34] Davranche, A., G. Lefebvre, and B. Poulin, Wetland monitoring using classification trees and SPOT-5 seasonal time series. *Remote sensing of environment*. 114(3): p. 552-562, **2010**.
- [35] Rapinel, S., et al., Evaluation of Sentinel-2 time-series for mapping floodplain grassland plant communities. *Remote sensing of environment*. 223: p. 115-129, **2019**.

- [36] Goffi, A., et al., Towards an automated approach to map flooded areas from Sentinel-2 MSI data and soft integration of water spectral features. *International Journal of Applied Earth Observation and Geoinformation*. 84: p. 101951, **2020**.
- [37] Caballero, I., J. Ruiz, and G. Navarro, Sentinel-2 satellites provide near-real time evaluation of catastrophic floods in the west mediterranean. *Water*. 11(12): p. 2499, **2019**.
- [38] Atefi, M.R. and H. Miura, Detection of flash flood inundated areas using relative difference in NDVI from sentinel-2 images: a case study of the August 2020 event in Charikar, Afghanistan. *Remote Sensing*. 14(15): p. 3647, **2022**.
- [39] Shamaoma, H., N. Kerle, and D. Alkema. Extraction of flood-modelling related base-data from multi-source remote sensing imagery. in *ISPRS mid-term symposium*. **2006**.
- [40] Yang, Y., et al., Modeling of a compound flood induced by the levee breach at Qianbujing Creek, Shanghai, during Typhoon Fitow. *Natural Hazards and Earth System Sciences*. 21(11): p. 3563-3572, **2021**.
- [41] Sawaya, K.E., et al., Extending satellite remote sensing to local scales: land and water resource monitoring using high-resolution imagery. *Remote sensing of Environment*. 88(1-2): p. 144-156, **2003**.
- [42] Munawar, H.S., et al., UAVs in Disaster Management: Application of Integrated Aerial Imagery and Convolutional Neural Network for Flood Detection. *Sustainability*. 13(14): p. 7547, **2021**.
- [43] Wang, Z. and E.R. Vivoni, Mapping Flash Flood Hazards in Arid Regions Using CubeSats. *Remote Sensing*. 14(17): p. 4218, **2022**.
- [44] Santilli, G., et al., CubeSat constellations for disaster management in remote areas. *Acta Astronautica*. 145: p. 11-17, **2018**.
- [45] Iqbal, U., P. Perez, W. Li, and J. Barthelemy, How computer vision can facilitate flood management: A systematic review. *International Journal of Disaster Risk Reduction*. 53: p. 102030, **2021**.
- [46] Feng, Q., J. Liu, and J. Gong, Urban flood mapping based on unmanned aerial vehicle remote sensing and random forest classifier—A case of Yuyao, China. *Water*. 7(4): p. 1437-1455, **2015**.
- [47] Popescu, D., L. Ichim, and T. Caramihale. Flood areas detection based on UAV surveillance system. in *2015 19th International conference on system theory, control and computing (ICSTCC)*. IEEE. **2015**.

- [48] Gebrehiwot, A., et al., Deep convolutional neural network for flood extent mapping using unmanned aerial vehicles data. *Sensors*. 19(7): p. 1486, **2019**.
- [49] Karamuz, E., R.J. Romanowicz, and J. Doroszkiewicz, The use of unmanned aerial vehicles in flood hazard assessment. *Journal of Flood Risk Management*. 13(4): p. e12622, **2020**.
- [50] Iqbal, A., et al., Effectiveness of UAV-based DTM and satellite-based DEMs for local-level flood modeling in Jamuna floodplain. *Journal of Flood Risk Management*: p. e12937, **2023**.
- [51] Ward, D.P., et al., Floodplain inundation and vegetation dynamics in the Alligator Rivers region (Kakadu) of northern Australia assessed using optical and radar remote sensing. *Remote Sensing of Environment*. 147: p. 43-55, **2014**.
- [52] Schumann, G., G. Di Baldassarre, D. Alsdorf, and P.D. Bates, Near real-time flood wave approximation on large rivers from space: Application to the River Po, Italy. *Water Resources Research*. 46(5): p. n/a-n/a, **2010**.
- [53] O'Grady, D., M. Leblanc, and D. Gillieson, Use of ENVISAT ASAR Global Monitoring Mode to complement optical data in the mapping of rapid broad-scale flooding in Pakistan. *Hydrology and Earth System Sciences*. 15(11): p. 3475-3494, **2011**.
- [54] Schumann, G.J.-P. and D.K. Moller, Microwave remote sensing of flood inundation. *Physics and Chemistry of the Earth, Parts a/b/c*. 83: p. 84-95, **2015**.
- [55] Martinis, S., A. Twele, and S. Voigt, Towards operational near real-time flood detection using a split-based automatic thresholding procedure on high resolution TerraSAR-X data. *Natural Hazards and Earth System Sciences*. 9(2): p. 303-314, **2009**.
- [56] Mason, D.C., et al., Flood detection in urban areas using TerraSAR-X. *IEEE transactions on geoscience and remote sensing*. 48(2): p. 882-894, **2009**.
- [57] Matgen, P., et al., Towards an automated SAR-based flood monitoring system: Lessons learned from two case studies. *Physics and Chemistry of the Earth, Parts A/B/C*. 36(7-8): p. 241-252, **2011**.
- [58] Mason, D., et al., Automatic near real-time selection of flood water levels from high resolution Synthetic Aperture Radar images for assimilation into hydraulic models: A case study. *Remote Sensing of Environment*. 124: p. 705-716, **2012**.

- [59] Giustarini, L., et al., A change detection approach to flood mapping in urban areas using TerraSAR-X. *IEEE transactions on Geoscience and Remote Sensing*. 51(4): p. 2417-2430, **2012**.
- [60] Yu, Z., Q. An, W. Liu, and Y. Wang, Analysis and evaluation of surface water changes in the lower reaches of the Yangtze River using Sentinel-1 imagery. *Journal of Hydrology: Regional Studies*. 41: p. 101074, **2022**.
- [61] Pulvirenti, L., M. Chini, N. Pierdicca, and G. Boni, Use of SAR data for detecting floodwater in urban and agricultural areas: The role of the interferometric coherence. *IEEE Transactions on Geoscience and Remote Sensing*. 54(3): p. 1532-1544, **2015**.
- [62] Pradhan, B., M.S. Tehrany, and M.N. Jebur, A new semiautomated detection mapping of flood extent from TerraSAR-X satellite image using rule-based classification and taguchi optimization techniques. *IEEE Transactions on Geoscience and Remote Sensing*. 54(7): p. 4331-4342, **2016**.
- [63] Li, Y., et al., Urban flood mapping using SAR intensity and interferometric coherence via Bayesian network fusion. *Remote Sensing*. 11(19): p. 2231, **2019**.
- [64] Daňo, F., P. Drábik, and E. Hanuláková, Circular business models in textiles and apparel sector in Slovakia. *Central European Business Review*. 9(1): p. 1, **2020**.
- [65] Chaabani, C., et al., Flood mapping in a complex environment using bistatic TanDEM-X/TerraSAR-X InSAR coherence. *Remote sensing*. 10(12): p. 1873, **2018**.
- [66] Baghermanesh, S.S., S. Jabari, and H. McGrath, Urban Flood Detection Using TerraSAR-X and SAR Simulated Reflectivity Maps. *Remote Sensing*. 14(23): p. 6154, **2022**.
- [67] Twele, A., W. Cao, S. Plank, and S. Martinis, Sentinel-1-based flood mapping: a fully automated processing chain. *International Journal of Remote Sensing*. 37(13): p. 2990-3004, **2016**.
- [68] Martinis, S. Improving flood mapping in arid areas using Sentinel-1 time series data. in *2017 IEEE international geoscience and remote sensing symposium (IGARSS)*. IEEE . **2017**.
- [69] Martinis, S. A Sentinel-1 times series-based exclusion layer for improved flood mapping in arid areas. in *IGARSS 2018-2018 IEEE International Geoscience and Remote Sensing Symposium*. IEEE, **2018**.

- [70] Amitrano, D., et al., Unsupervised Rapid Flood Mapping Using Sentinel-1 GRD SAR Images. *IEEE Transactions on Geoscience and Remote Sensing*. 56(6): p. 3290-3299, **2018**.
- [71] Haralick, R.M., K. Shanmugam, and I.H. Dinstein, Textural features for image classification. *IEEE Transactions on systems, man, and cybernetics*(6): p. 610-621, **1973**.
- [72] Li, Y., S. Martinis, S. Plank, and R. Ludwig, An automatic change detection approach for rapid flood mapping in Sentinel-1 SAR data. *International Journal of Applied Earth Observation and Geoinformation*. 73: p. 123-135, **2018**.
- [73] Tavus, B., S. Kocaman, C. Gokceoglu, and H. Nefeslioglu, Considerations on the use of Sentinel-1 data in flood mapping in urban areas: Ankara (Turkey) 2018 floods. *The International Archives of the Photogrammetry, Remote Sensing and Spatial Information Sciences*. 42: p. 575-581, **2018**.
- [74] Hess, L.L., J.M. Melack, and D.S. Simonett, Radar detection of flooding beneath the forest canopy: a review. *International Journal of Remote Sensing*. 11(7): p. 1313-1325, **1990**.
- [75] Hess, L.L., J.M. Melack, S. Filoso, and Y. Wang, Delineation of inundated area and vegetation along the Amazon floodplain with the SIR-C synthetic aperture radar. *IEEE transactions on geoscience and remote sensing*. 33(4): p. 896-904, **1995**.
- [76] Hess, L. and J. Melack, Remote sensing of vegetation and flooding on Magela Creek Floodplain (Northern Territory, Australia) with the SIR-C synthetic aperture radar. *Hydrobiologia*. 500: p. 65-82, **2003**.
- [77] Rosenqvist, Å. and C. Birkett, Evaluation of JERS-1 SAR mosaics for hydrological applications in the Congo river basin. *International Journal of Remote Sensing*. 23(7): p. 1283-1302, **2002**.
- [78] Surampudi, S. and V. Kumar, Flood Depth Estimation in Agricultural Lands From L and C-Band Synthetic Aperture Radar Images and Digital Elevation Model. *IEEE Access*. 11: p. 3241-3256, **2023**.
- [79] Plank, S., M. Jüssi, S. Martinis, and A. Twele, Mapping of flooded vegetation by means of polarimetric Sentinel-1 and ALOS-2/PALSAR-2 imagery. *International Journal of Remote Sensing*. 38(13): p. 3831-3850, **2017**.

- [80] Ohki, M., K. Yamamoto, T. Tadono, and K. Yoshimura, Automated processing for flood area detection using ALOS-2 and hydrodynamic simulation data. *Remote Sensing*. 12(17): p. 2709, **2020**.
- [81] Kwak, Y., S.-h. Yun, and Y. Iwami. A new approach for rapid urban flood mapping using ALOS-2/PALSAR-2 in 2015 Kinu River Flood, Japan. in 2017 IEEE International Geoscience and Remote Sensing Symposium (IGARSS). IEEE, **2017**.
- [82] Gokon, H., F. Endo, and S. Koshimura, Detecting Urban Floods with Small and Large Scale Analysis of ALOS-2/PALSAR-2 Data. *Remote Sensing*. 15(2): p. 532, **2023**.
- [83] Zoka, M., E. Psomiadis, and N. Dercas. The complementary use of optical and SAR data in monitoring flood events and their effects. in *Proceedings*. 2018. MDPI.
- [84] Tong, X., et al., An approach for flood monitoring by the combined use of Landsat 8 optical imagery and COSMO-SkyMed radar imagery. *ISPRS journal of photogrammetry and remote sensing*. 136: p. 144-153, **2018**.
- [85] Martinis, S., et al., A multi-scale flood monitoring system based on fully automatic MODIS and TerraSAR-X processing chains. *Remote Sensing*. 5(11): p. 5598-5619, **2013**.
- [86] DeVries, B., et al., Rapid and robust monitoring of flood events using Sentinel-1 and Landsat data on the Google Earth Engine. *Remote Sensing of Environment*. 240: p. 111664, **2020**.
- [87] Benoudjit, A. and R. Guida, A novel fully automated mapping of the flood extent on SAR images using a supervised classifier. *Remote Sensing*. 11(7): p. 779, **2019**.
- [88] Sunar, A., N. Yagmur, and A. Dervisoglu, Flood analysis with remote sensing data—A case study: Maritsa river, Edirne. *The International Archives of the Photogrammetry, Remote Sensing and Spatial Information Sciences*. 42: p. 497-502, **2019**.
- [89] Bioresita, F., A. Puissant, A. Stumpf, and J.-P. Malet, Fusion of Sentinel-1 and Sentinel-2 image time series for permanent and temporary surface water mapping. *International Journal of Remote Sensing*: p. 1-24, **2019**.

- [90] Huang, M. and S. Jin, Rapid flood mapping and evaluation with a supervised classifier and change detection in shouguang using sentinel-1 sar and sentinel-2 optical data. *Remote Sensing*. 12(13): p. 2073, **2020**.
- [91] Manakos, I., G.A. Kordelas, and K. Marini, Fusion of Sentinel-1 data with Sentinel-2 products to overcome non-favourable atmospheric conditions for the delineation of inundation maps. *European Journal of Remote Sensing*. 53(sup2): p. 53-66, **2020**.
- [92] Slagter, B., N.-E. Tsendbazar, A. Vollrath, and J. Reiche, Mapping wetland characteristics using temporally dense Sentinel-1 and Sentinel-2 data: A case study in the St. Lucia wetlands, South Africa. *International Journal of Applied Earth Observation and Geoinformation*. 86, **2020**.
- [93] Singha, M., et al., Identifying floods and flood-affected paddy rice fields in Bangladesh based on Sentinel-1 imagery and Google Earth Engine. *ISPRS Journal of Photogrammetry and Remote Sensing*. 166: p. 278-293, **2020**.
- [94] Hakdaoui, S., et al., A collaborative change detection approach on multi-sensor spatial imagery for desert wetland monitoring after a flash flood in Southern Morocco. *Remote Sensing*. 11(9): p. 1042, **2019**.
- [95] Hakdaoui, S. and A. Emran, Extraction of water information based on SAR RADAR and Optical image processing: Case of flood disaster in Southern Morocco, in *Geospatial Technology*. Springer. p. 15-29, **2020**.
- [96] Tripathi, G., A.C. Pandey, B.R. Parida, and A. Kumar, Flood inundation mapping and impact assessment using multi-temporal optical and SAR satellite data: a case study of 2017 Flood in Darbhanga district, Bihar, India. *Water Resources Management*. 34(6): p. 1871-1892, **2020**.
- [97] Sherpa, S.F., et al., Probabilistic Mapping of August 2018 Flood of Kerala, India, Using Space-Borne Synthetic Aperture Radar. *IEEE Journal of Selected Topics in Applied Earth Observations and Remote Sensing*. 13: p. 896-913, **2020**.
- [98] Lal, P., et al., Evaluating the 2018 extreme flood hazard events in Kerala, India. *Remote Sensing Letters*. 11(5): p. 436-445, **2020**.
- [99] Bai, Y., et al., Enhancement of detecting permanent water and temporary water in flood disasters by fusing sentinel-1 and sentinel-2 imagery using deep learning algorithms: Demonstration of sen1floods11 benchmark datasets. *Remote Sensing*. 13(11): p. 2220, **2021**.

- [100] Gašparović, M. and D. Klobučar, Mapping floods in lowland forest using sentinel-1 and sentinel-2 data and an object-based approach. *Forests*. 12(5): p. 553, **2021**.
- [101] Muszynski, M., et al. Flood Event Detection from Sentinel 1 and Sentinel 2 Data: Does Land Use Matter for Performance of U-Net based Flood Segmenters? in *2022 IEEE International Conference on Big Data (Big Data)*, IEEE, **2022**.
- [102] Jenifer, A.E., A. Aparna, N. Sudha, and A. Kumar, AgriFloodNet: a dual patch CNN architecture for mapping flooded agricultural lands via bi-temporal multi-sensor images. *Geocarto International*. 37(26): p. 13618-13637, **2022**.
- [103] Pulvirenti, L., N. Pierdicca, M. Chini, and L. Guerriero, Monitoring Flood Evolution in Vegetated Areas Using COSMO-SkyMed Data: The Tuscany 2009 Case Study. *IEEE Journal of Selected Topics in Applied Earth Observations and Remote Sensing*. 6(4): p. 1807-1816, **2013**.
- [104] Polverari, F., et al. Precipitation signature on side-looking aperture radar imaging: Sensitivity analysis to surface effects at C, X and Ku band. **2014**.
- [105] Hong, S.-H. and S. Wdowinski, Double-Bounce Component in Cross-Polarimetric SAR From a New Scattering Target Decomposition. *IEEE Transactions on Geoscience and Remote Sensing*. 52(6): p. 3039-3051, **2014**.
- [106] Quesney, A., Estimation of Watershed Soil Moisture Index from ERS/SAR Data. *Remote Sensing of Environment*. 72(3): p. 290-303, **2000**.
- [107] Paloscia, S., et al., Soil moisture mapping using Sentinel-1 images: Algorithm and preliminary validation. *Remote Sensing of Environment*. 134: p. 234-248, **2013**.
- [108] Otsu, N., A Threshold Selection Method from Gray-Level Histograms. *IEEE Transactions on Systems, Man, and Cybernetics*. 9(1): p. 62-66, **1979**.
- [109] Tew, Y.L., et al., Rapid extreme tropical precipitation and flood inundation mapping framework (RETRACE): Initial Testing for the 2021–2022 Malaysia Flood. *ISPRS International Journal of Geo-Information*. 11(7): p. 378, **2022**.
- [110] Schumann, G., G. Di Baldassarre, and P.D. Bates, The Utility of Spaceborne Radar to Render Flood Inundation Maps Based on Multialgorithm Ensembles. *IEEE Transactions on Geoscience and Remote Sensing*. 47(8): p. 2801-2807, **2009**.
- [111] Pulvirenti, L., et al., Discrimination of Water Surfaces, Heavy Rainfall, and Wet Snow Using COSMO-SkyMed Observations of Severe Weather Events. *IEEE Transactions on Geoscience and Remote Sensing*. 52(2): p. 858-869, **2014**.

- [112] Chen, Z. and S. Zhao, Automatic monitoring of surface water dynamics using Sentinel-1 and Sentinel-2 data with Google Earth Engine. *International Journal of Applied Earth Observation and Geoinformation*. 113: p. 103010, **2022**.
- [113] Martinis, S., et al., Comparing four operational SAR-based water and flood detection approaches. *International Journal of Remote Sensing*. 36(13): p. 3519-3543, **2015**.
- [114] Bazi, Y., L. Bruzzone, and F. Melgani, An unsupervised approach based on the generalized Gaussian model to automatic change detection in multitemporal SAR images. *IEEE Transactions on Geoscience and Remote Sensing*. 43(4): p. 874-887, **2005**.
- [115] Chini, M., R. Hostache, L. Giustarini, and P. Matgen, A Hierarchical Split-Based Approach for Parametric Thresholding of SAR Images: Flood Inundation as a Test Case. *IEEE Transactions on Geoscience and Remote Sensing*. 55(12): p. 6975-6988, **2017**.
- [116] Schlaffer, S., P. Matgen, M. Hollaus, and W. Wagner, Flood detection from multi-temporal SAR data using harmonic analysis and change detection. *International Journal of Applied Earth Observation and Geoinformation*. 38: p. 15-24, **2015**.
- [117] Clement, M.A., C.G. Kilsby, and P. Moore, Multi-temporal synthetic aperture radar flood mapping using change detection. *Journal of Flood Risk Management*. 11(2): p. 152-168, **2018**.
- [118] Zadeh, L.A., Fuzzy sets as a basis for a theory of possibility. *Fuzzy Sets and Systems*. 100: p. 9-34, **1999**.
- [119] Pulvirenti, L., N. Pierdicca, M. Chini, and L. Guerriero, An algorithm for operational flood mapping from Synthetic Aperture Radar (SAR) data using fuzzy logic. *Natural Hazards and Earth System Sciences*. 11(2): p. 529-540, **2011**.
- [120] Dasgupta, A., et al., Towards operational SAR-based flood mapping using neuro-fuzzy texture-based approaches. *Remote sensing of Environment*. 215: p. 313-329, **2018**.
- [121] Grimaldi, S., et al., Flood mapping under vegetation using single SAR acquisitions. *Remote Sensing of Environment*. 237: p. 111582, **2020**.
- [122] Cian, F., M. Marconcini, and P. Ceccato, Normalized Difference Flood Index for rapid flood mapping: Taking advantage of EO big data. *Remote Sensing of Environment*. 209: p. 712-730, **2018**.

- [123] Hostache, R., P. Matgen, and W. Wagner, Change detection approaches for flood extent mapping: How to select the most adequate reference image from online archives? *International Journal of Applied Earth Observation and Geoinformation*. 19: p. 205-213, **2012**.
- [124] Ban, Y. and O.A. Yousif, Multitemporal Spaceborne SAR Data for Urban Change Detection in China. *IEEE Journal of Selected Topics in Applied Earth Observations and Remote Sensing*. 5(4): p. 1087-1094, **2012**.
- [125] Skakun, S., A neural network approach to flood mapping using satellite imagery. *Computing and Informatics*. 29(6): p. 1013-1024, **2010**.
- [126] Notti, D., et al., Potential and limitations of open satellite data for flood mapping. *Remote sensing*. 10(11): p. 1673, **2018**.
- [127] Tanim, T.R., et al., A comprehensive understanding of the aging effects of extreme fast charging on high Ni NMC cathode. *Advanced Energy Materials*. 12(22): p. 2103712, **2022**.
- [128] Tavus, B., S. Kocaman, and C. Gokceoglu, Flood damage assessment with Sentinel-1 and Sentinel-2 data after Sardoba dam break with GLCM features and Random Forest method. *Science of The Total Environment*. 816: p. 151585, **2021**.
- [129] Gašparović, M. and D. Dobrinić, Comparative assessment of machine learning methods for urban vegetation mapping using multitemporal sentinel-1 imagery. *Remote Sensing*. 12(12): p. 1952, **2020**.
- [130] Radhakrishnan, K., K.A. Scott, and D.A. Clausi, Sea ice concentration estimation: Using passive microwave and SAR data with a U-net and curriculum learning. *IEEE Journal of Selected Topics in Applied Earth Observations and Remote Sensing*. 14: p. 5339-5351, **2021**.
- [131] Hosseiny, H., F. Nazari, V. Smith, and C. Nataraj, A framework for modeling flood depth using a hybrid of hydraulics and machine learning. *Scientific Reports*. 10(1): p. 8222, **2020**.
- [132] Chen, Z., N. Chen, W. Du, and J. Gong, An active monitoring method for flood events. *Computers & Geosciences*. 116: p. 42-52, **2018**.
- [133] Berger, M., et al., ESA's sentinel missions in support of Earth system science. *Remote sensing of environment*. 120: p. 84-90, **2012**.
- [134] Planet application program interface: In space for life on Earth, <https://api.planet.com>,

- [135] Tavus, B., S. Kocaman, H. Nefeslioğlu, and C. Gökçeoğlu, Flood mapping using Sentinel-1 SAR data: A case study of Ordu 8 August 2018 flood. **2019**.
- [136] Breiman, L., Random forests. *Machine learning*. 45: p. 5-32, **2001**.
- [137] Long, D. and F. Ulaby, *Microwave radar and radiometric remote sensing*. 2015: Artech.
- [138] Schreier, G., A. Roth, and W. Knöpfle. ERS-1 SAR geocoding system as link between spaceborne and earth reference data. in *AIP Conference Proceedings*. 1993. American Institute of Physics.
- [139] Singh, P. and R. Shree, A new computationally improved homomorphic despeckling technique of SAR images. *International Journal of Advanced Research in Computer Science*. 8(3), **2017**.
- [140] Lee, J.-S. and E. Pottier, *Polarimetric radar imaging: from basics to applications*. 2017: CRC press.
- [141] Jaybhay, J. and R. Shastri, A study of speckle noise reduction filters. *signal & image processing: An international Journal (SIPIJ)*. 6(3): p. 71-80, **2015**.
- [142] Putri, A.F.S., W. Widyatmanti, and D.A. Umarhadi, Sentinel-1 and Sentinel-2 data fusion to distinguish building damage level of the 2018 Lombok Earthquake. *Remote Sensing Applications: Society and Environment*. 26: p. 100724, **2022**.
- [143] Khatami, R., G. Mountrakis, and S.V. Stehman, A meta-analysis of remote sensing research on supervised pixel-based land-cover image classification processes: General guidelines for practitioners and future research. *Remote sensing of environment*. 177: p. 89-100, **2016**.
- [144] Hurskainen, P., et al., Auxiliary datasets improve accuracy of object-based land use/land cover classification in heterogeneous savanna landscapes. *Remote sensing of environment*. 233: p. 111354, **2019**.
- [145] Xia, H. and Q. Rao. Flood Level Prediction on the Basis of the Artificial Neural Network. in *2009 First International Conference on Information Science and Engineering*. **2009**.
- [146] Gebremichael, E., et al., Flood hazard and risk assessment of extreme weather events using synthetic aperture radar and auxiliary data: A case study. *Remote Sensing*. 12(21): p. 3588, **2020**.
- [147] Cerbelaud, A., et al., Supervised classification methods for automatic damage detection caused by heavy rainfall using multitemporal high resolution optical

- imagery and auxiliary data. *The International Archives of the Photogrammetry, Remote Sensing and Spatial Information Sciences*. 43: p. 693-700, **2021**.
- [148] Senthilnath, J., et al., Integration of speckle de-noising and image segmentation using Synthetic Aperture Radar image for flood extent extraction. *Journal of earth system science*. 122: p. 559-572, **2013**.
- [149] Tucker, C.J., Red and photographic infrared linear combinations for monitoring vegetation. *Remote sensing of Environment*. 8(2): p. 127-150, **1979**.
- [150] McFeeters, S.K., The use of the Normalized Difference Water Index (NDWI) in the delineation of open water features. *International journal of remote sensing*. 17(7): p. 1425-1432, **1996**.
- [151] Mohammadi, A., J.F. Costelloe, and D. Ryu, Application of time series of remotely sensed normalized difference water, vegetation and moisture indices in characterizing flood dynamics of large-scale arid zone floodplains. *Remote sensing of environment*. 190: p. 70-82, **2017**.
- [152] Abdullah, A.Y.M., et al., Spatio-temporal patterns of land use/land cover change in the heterogeneous coastal region of Bangladesh between 1990 and 2017. *Remote Sensing*. 11(7): p. 790, **2019**.
- [153] Weng, Q., *An introduction to contemporary remote sensing*. **2012**: McGraw-Hill Education.
- [154] Santoro, M., et al., Strengths and weaknesses of multi-year Envisat ASAR backscatter measurements to map permanent open water bodies at global scale. *Remote Sensing of Environment*. 171: p. 185-201, **2015**.
- [155] Graosque, J.Z. and L.A. Guasselli, Principal component analysis of C-SAR images for flood mapping, Santa Fe Province, Argentina. *Territorium: Revista Internacional de Riscos*. Portugal. Vol. 27, n. 2 (2020), p. 41-48, **2020**.
- [156] Graosque, J.Z., Mapeamento das áreas de inundação utilizando imagens C-SAR e SRTM, nas províncias de Santa Fé e Entre Ríos, Argentina. **2018**.
- [157] Gómez-Palacios, D., M.A. Torres, and E. Reinoso, Flood mapping through principal component analysis of multitemporal satellite imagery considering the alteration of water spectral properties due to turbidity conditions. *Geomatics, Natural Hazards and Risk*. 8(2): p. 607-623, **2017**.
- [158] Dutsenwai, H.S., B.B. Ahmad, A. Mijinyawa, and A.I. Tanko, Fusion of SAR images for flood extent mapping in northern peninsula Malaysia. *International Journal of Advanced and Applied Sciences*. 3(12): p. 37-48, **2016**.

- [159] Xie, H., et al., Evaluation of Landsat 8 OLI imagery for unsupervised inland water extraction. *International Journal of Remote Sensing*. 37(8): p. 1826-1844, **2016**.
- [160] Liu, C., et al. Deep neural network fusion via graph matching with applications to model ensemble and federated learning. in *International Conference on Machine Learning*. **2022**.
- [161] Khan, S.N., D. Li, and M. Maimaitijiang, A Geographically Weighted Random Forest Approach to Predict Corn Yield in the US Corn Belt. *Remote Sensing*. 14(12): p. 2843, **2022**.
- [162] Li, M., et al., Monitoring Post-Flood Recovery of Croplands Using the Integrated Sentinel-1/2 Imagery in the Yangtze-Huai River Basin. *Remote Sensing*. 14(3): p. 690, **2022**.
- [163] Wieland, M. and M. Pittore, Performance evaluation of machine learning algorithms for urban pattern recognition from multi-spectral satellite images. *Remote Sensing*. 6(4): p. 2912-2939, **2014**.
- [164] Phiri, D., M. Simwanda, and V. Nyirenda, Mapping the impacts of cyclone Idai in Mozambique using Sentinel-2 and OBIA approach. *South African Geographical Journal*. 103(2): p. 237-258, **2021**.
- [165] Belgiu, M. and L. Drăguț, Random forest in remote sensing: A review of applications and future directions. *ISPRS journal of photogrammetry and remote sensing*. 114: p. 24-31, **2016**.
- [166] Ham, J., Y. Chen, M.M. Crawford, and J. Ghosh, Investigation of the random forest framework for classification of hyperspectral data. *IEEE Transactions on Geoscience and Remote Sensing*. 43(3): p. 492-501, **2005**.
- [167] Gislason, P.O., J.A. Benediktsson, and J.R. Sveinsson, Random forests for land cover classification. *Pattern recognition letters*. 27(4): p. 294-300, **2006**.
- [168] Waske, B. and S. van der Linden, Classifying multilevel imagery from SAR and optical sensors by decision fusion. *IEEE Transactions on Geoscience and Remote Sensing*. 46(5): p. 1457-1466, **2008**.
- [169] Waske, B. and M. Braun, Classifier ensembles for land cover mapping using multitemporal SAR imagery. *ISPRS journal of photogrammetry and remote sensing*. 64(5): p. 450-457, **2009**.
- [170] Rodriguez-Galiano, V., M. Sanchez-Castillo, M. Chica-Olmo, and M. Chica-Rivas, Machine learning predictive models for mineral prospectivity: An

- evaluation of neural networks, random forest, regression trees and support vector machines. *Ore Geology Reviews*. 71: p. 804-818, **2015**.
- [171] Phiri, D., J. Morgenroth, C. Xu, and T. Hermosilla, Effects of pre-processing methods on Landsat OLI-8 land cover classification using OBIA and random forests classifier. *International journal of applied earth observation and geoinformation*. 73: p. 170-178, **2018**.
- [172] Mather, P.M. and M. Koch, *Computer processing of remotely-sensed images: an introduction*. John Wiley & Sons. **2011**.
- [173] Cohen, J., A coefficient of agreement for nominal scales. *Educational and psychological measurement*. 20(1): p. 37-46, **1960**.
- [174] Bangira, T., S.M. Alfieri, M. Menenti, and A. Van Niekerk, Comparing thresholding with machine learning classifiers for mapping complex water. *Remote Sensing*. 11(11): p. 1351, **2019**.
- [175] Konstantinova, A. and E. Loupian, Analysis of the consequences of the dam failure of the Sardoba Reservoir on May 1, 2020. *Sovremennyye problemy distantsionnogo zondirovaniya Zemli iz kosmosa*. 17(3): p. 261-266, **2020**.
- [176] Simonov, E., Uzbekistan dam collapse was a disaster waiting to happen. *The Third Pole*, **2020**.
- [177] Zanaga, D., Van De Kerchove, R., De Keersmaecker, W., Souverijns, N., Brockmann, C., Quast, R., Wevers, J., Grosu, A., Paccini, A., Vergnaud, S., Cartus, O., Santoro, M., Fritz, S., Georgieva, I., Lesiv, M., Carter, S., Herold, M., Li, Linlin, Tsendbazar, N.E., Ramoino, F., Arino, O., *ESA WorldCover 10 m 2020 v100*. **2021**.
- [178] Global, U., *Arc-Second Elevation (GTOPO30)*; **1996**.
- [179] Kocaman, S., et al., Evaluation of floods and landslides triggered by a meteorological catastrophe (Ordu, Turkey, August 2018) using optical and radar data. *Geofluids*. 2020: p. 1-18, **2020**.
- [180] Tavus, B., S. Kocaman, and C. Gokceoglu, Assessment of flooded areas caused by a dam break (Sardoba dam, Uzbekistan). *The International Archives of the Photogrammetry, Remote Sensing and Spatial Information Sciences*. 43: p. 291-297, **2021**.
- [181] Kocaman, S., E. Sevgen, and C. Gokceoglu. A Photogrammetric Surface Comparison for a Dam Reservoir in a Landslide—Prone Area in Eastern Anatolia, Turkey. in *Recent Advances in Geo-Environmental Engineering, Geomechanics*

- and Geotechnics, and Geohazards: Proceedings of the 1st Springer Conference of the Arabian Journal of Geosciences (CAJG-1), Tunisia 2018: p. 453-456, **2019**.
- [182] Shen, X., et al., Inundation Extent Mapping by Synthetic Aperture Radar: A Review. *Remote Sensing*. 11(7): p. 879, **2019**.
- [183] Schlaffer, S., M. Chini, L. Giustarini, and P. Matgen, Probabilistic mapping of flood-induced backscatter changes in SAR time series. *International Journal of Applied Earth Observation and Geoinformation*. 56: p. 77-87, **2017**.
- [184] D'Addabbo, A., et al., A Bayesian network for flood detection combining SAR imagery and ancillary data. *IEEE Transactions on Geoscience and Remote Sensing*. 54(6): p. 3612-3625, **2016**.
- [185] Tarpanelli, A., A.C. Mondini, and S. Camici, Effectiveness of Sentinel-1 and Sentinel-2 for flood detection assessment in Europe. *Natural Hazards and Earth System Sciences*. 22(8): p. 2473-2489, **2022**.
- [186] Tupas, M.E., F. Roth, B. Bauer-Marschallinger, and W. Wagner, An Intercomparison of Sentinel-1 Based Change Detection Algorithms for Flood Mapping. *Remote Sensing*. 15(5): p. 1200, **2023**.
- [187] Shahabi, H., et al., Flood detection and susceptibility mapping using sentinel-1 remote sensing data and a machine learning approach: Hybrid intelligence of bagging ensemble based on k-nearest neighbor classifier. *Remote Sensing*. 12(2): p. 266, **2020**.
- [188] Dotzler, S., J. Hill, H. Buddenbaum, and J. Stoffels, The potential of EnMAP and Sentinel-2 data for detecting drought stress phenomena in deciduous forest communities. *Remote Sensing*. 7(10): p. 14227-14258, **2015**.
- [189] Kääh, A., B. Altena, and J. Mascaro, Coseismic displacements of the 14 November 2016 M w 7.8 Kaikoura, New Zealand, earthquake using the Planet optical cubesat constellation. *Natural hazards and earth system sciences*. 17(5): p. 627-639, **2017**.
- [190] Dasgupta, A., S. Grimaldi, R. Ramsankaran, and J.P. Walker, Optimized glcm-based texture features for improved SAR-based flood mapping. in 2017 IEEE International Geoscience and Remote Sensing Symposium (IGARSS). **2017**.
- [191] Scotti, V., M. Giannini, and F. Cioffi, Enhanced flood mapping using synthetic aperture radar (SAR) images, hydraulic modelling, and social media: A case study of Hurricane Harvey (Houston, TX). *Journal of Flood Risk Management*. 13(4): p. e12647, **2020**.

- [192] Doshi, D. and M. Garschagen, Assessing social contracts for urban adaptation through social listening on Twitter. *npj Urban Sustainability*. 3(1): p. 30, **2023**.
- [193] Brouwer, T., et al., Probabilistic flood extent estimates from social media flood observations. *Natural Hazards and Earth System Sciences*. 17(5): p. 735-747, **2017**.
- [194] Potnis, A.V., R.C. Shinde, S.S. Durbha, and K.R. Kurte, Multi-class segmentation of urban floods from multispectral imagery using deep learning. in *IGARSS 2019-2019 IEEE international geoscience and remote sensing symposium*. IEEE. **2019**.
- [195] Peng, B., Z. Meng, Q. Huang, and C. Wang, Patch similarity convolutional neural network for urban flood extent mapping using bi-temporal satellite multispectral imagery. *Remote Sensing*. 11(21): p. 2492, **2019**.
- [196] Bonafilia, D., B. Tellman, T. Anderson, and E. Issenberg, Sen1Floods11: A georeferenced dataset to train and test deep learning flood algorithms for sentinel-1. in *Proceedings of the IEEE/CVF Conference on Computer Vision and Pattern Recognition Workshops*. **2020**.
- [197] Rambour, C., et al., Sen12-flood: a SAR and multispectral dataset for flood detection. IEEE: Piscataway, NJ, USA, **2020**.
- [198] Tavus, B., R. Can, and S. Kocaman, A CNN-based flood mapping approach using sentinel-1 data. in *2022 24th ISPRS Congress on Imaging Today, Foreseeing Tomorrow, Commission III*. 2022. Copernicus GmbH.